Excitonic Antiferromagnetism in two-dimensional t_{2g}^4 Systems

Von der Fakultät Mathematik und Physik der Universität Stuttgart
zur Erlangung der Würde eines Doktors der Naturwissenschaften
(Dr. rer. nat.) genehmigte Abhandlung

Vorgelegt von

Teresa Feldmaier

aus Waiblingen

Hauptberichterin:	Prof. Dr. Maria Daghofer
Mitberichter:	Jun.-Prof. Dr. Stefan Kaiser

Tag der mündlichen Prüfung: 18. Dezember 2019

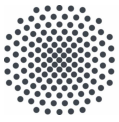

Institut für funktionelle Materie und Quantentechnologien
der Universität Stuttgart

2020

Inhaltsangabe

Stark korrelierte $4d$- und $5d$-Übergangsmetalloxide mit Spin-Bahn-Kopplung stehen im Fokus wissenschaftlicher Aufmerksamkeit, da ihre Kombination von Spin-Bahn-Kopplung und Elektronenkorrelationen interessante Phänomene, wie zum Beispiel topologisch nicht-triviale Phasen, erwarten lässt.

Da t_{2g}-Systeme mit einem Loch bereits eingehend untersucht wurden, konzentriert sich diese Arbeit auf Systeme mit zwei Löchern. Im atomaren Limes garantieren starke lokale Wechselwirkungen, dass pro Platz nur eines der drei t_{2g}-Orbitale doppelt besetzt ist, wodurch sich aus den anderen beiden, halbgefüllten Orbitalen der Bahndrehimpuls $L = 1$ und sowie der Gesamtspin $S = 1$ ergibt. Durch den Einfluss der Spin-Bahn-Kopplung koppeln L und S zu einem ionischen Grundzustand mit Gesamtdrehimpuls $J = 0$. Ein solcher Singulettzustand tritt wahrscheinlich in nichtmagnetischen Doppelperovskitiridaten auf, in welchen die Spin-Bahn-Kopplung recht stark ist. Für gemäßigte Spin-Bahn-Kopplungsstärken wird jedoch der sogenannte exzitonische Magnetismus erwartet, welcher maßgeblich vom Superaustausch getrieben wird. Dieser bezieht auch die höher liegenden magnetischen Triplettzustände $J = 1$ und die Quintettzustände $J = 2$ mit ein. Ist der Superaustausch stark genug, um mit der von der Spin-Bahn-Kopplung erzeugten Singulett-Triplett-Aufspaltung konkurrieren zu können, werden der lokalen Wellenfunktion Anteile des $J = 1$-Zustandes zum $J = 0$-Zustand beigemischt. Somit erlangt die lokale Wellenfunktion ein magnetisches Moment, welches ordnen kann. Eine mögliche Realisierung dieses Prozesses wird in Ca_2RuO_4 erwartet. Dieses t_{2g}^4-Ruthenat mit quadratischer Gitterstruktur zeigt für tiefe Temperaturen eine antiferromagnetische Ordnung, die mit einer Stauchung der RuO_6-Oktaeder einhergeht. Das resultierende tetragonale Kristallfeld senkt das xy-Orbital ab, dessen nahezu volle Besetzung in Experimenten und numerischen Berechnungen bestätigt wird. Eine Betrachtung der magnetischen Ordnung im Rahmen dieses Ansatzes führt auf einen konventionellen Spin-1-Magnetismus. Jedoch zeigen experimentelle Messungen magnetischer Anregungen Widersprüche zum Verhalten eines Heisenberg-Antiferromagneten auf, welche sich durch das exzitonische Bild erklären lassen.

Die Interaktion zweier Löcher auf einem zweidimensionalen Quadratgitter wird durch ein Dreiband-Hubbard-Modells beschrieben, welches die kinetische Energie der Elektronen, lokale Wechselwirkungen, die Spin-Bahn-Kopplung und das tetragonale Kristallfeld berücksichtigt. Durch Nutzung der variationellen Cluster-Näherung (Variational Cluster Approximation) können Wechselwirkungsphänomene und spontane Symmetriebrechung untersucht werden. Die variationellen Cluster-Näherung benötigt zunächst die Lösung des Hamilton-Operators auf einem kleinen Cluster, welche durch exakte Diagonalisie-

rung gegeben ist. Die Selbstenergie des Clusters wird dann im thermodynamischen Limes in die Einteilchen-Green-Funktion eingesetzt, um das großkanonische Potential zu erhalten. Basierend auf der Selbstenergiefunktionaltheorie kann das großkanonische Potential nun optimiert werden, indem Einteilchenparameter, zum Beispiel die kinetische Energie oder das chemische Potential, auf dem Referenzsystem variiert werden. Insbesondere lassen sich fiktive symmetriebrechende Weiss-Felder anwenden, welche nur auf den kleinen Cluster, nicht jedoch auf das ganze Gitter, wirken. Optimiert ein solches Weiss-Feld die Selbstenergie des vollsymmetrischen Hamilton-Operators, kann daraus spontane Symmetriebrechung gefolgert werden. Dieses Vorgehen zeigte sich bereits sehr erfolgreich in der Beschreibung winkelaufgelöster Photoemissionspektren in Sr_2IrO_4. In der vorliegenden Arbeit werden durch Anwendung diverser Weiss-Felder abhängig von der Stärke der Wechselwirkungen antiferromagnetische Phasen mit Spin- und Orbitalordnung sowie eine paramagnetische Phase gefunden. Um den Grundzustand des Gitters verstehen zu können, werden die Erwartungswerte der lokalen atomaren Grundzustände und der Lochdichten in den magnetischen Phasen sowie in Abwesenheit der Weiss-Felder berechnet. Zudem werden Ein-Teilchen-Spektraldichten präsentiert, welche mit winkelaufgelösten Photoemissionspektren verglichen werden können.

Zunächst wird der exzitonische Magnetismus in einem einfachen Modell simuliert, welches nur die kinetische Energie, die lokalen Elektronenwechselwirkungen, sowie die Spin-Bahn-Kopplung berücksichtigt. Für schwache Spin-Bahn-Kopplung existiert eine antiferromagnetische Phase, die durch ein Streifenmuster in Orbital und Spin gekennzeichnet ist. Gemäßigte Spin-Bahn-Kopplungsstärken führen zu einer antiferromagnetischen exzitonischen Phase mit Schachbrettmuster, wobei die Spins aus der Gitterebene heraus zeigen. Starke Spin-Bahn-Kopplung unterbindet die magnetische Ordnung und es kommt zu einer paramagnetischen Phase.

Wird das tetragonale Kristallfeld ins Modell integriert, verändern sich die magnetischen Phasen ein wenig. Das Kristallfeld bewirkt eine Umorientierung der Spins in die Gitterebene und ruft eine starke Polarisierung der Orbitale hervor. Trotzdem bleibt der exzitonische Magnetismus für gemäßigte Kristallfeldstärken erhalten und verschwindet erst für stärkere. Die Spin-Bahn-Kopplung spielt eine entscheidende Rolle, da sie weiterhin für die Ausbildung der paramagnetischen Phase verantwortlich ist.

Für die Untersuchung des Magnetismus in Ca_2RuO_4 werden mit Hilfe der Dichtefunktionaltheorie realistische Parameter hergeleitet und mit experimentellen Daten kombiniert. Es zeigt sich, dass Ca_2RuO_4 in den Bereich exzitonischen Magnetismus fällt, obwohl die Polarisierung der Orbitale sehr stark ist. Zudem erweist sich das System als recht anfällig für kleine Änderungen der Spin-Bahn-Kopplungsstärke, da nur für Stärken in der Größenordnung der kinetischen Energie der exzitonische Charakter vorliegt. Für kleinere Spin-Bahn-Kopplung ergibt sich ein reiner Spin-1-Magnetismus, während stärkere Spin-Bahn-Kopplung einen paramagnetischen Zustand bewirkt.

Abstract

Strongly correlated and spin-orbit coupled $4d^4$ and $5d^4$ transition metal oxides are a focus of strong scientific attention as this combination of spin-orbit coupling and correlations is expected to provide interesting phenomena like topologically nontrivial phases such as topological Mott insulators and spin liquids.

While the case of one hole in the t_{2g} subspace is extensively studied, we focus on systems with two holes. In the atomic limit, strong on-site interactions ensure that only one t_{2g} orbital at each site is doubly occupied. The resulting two half-filled orbitals then form an effective orbital angular momentum $L = 1$ and spin $S = 1$. Spin-orbit coupling gives an ionic ground state $J = 0$ by coupling L and S to a total angular momentum J. This singlet ground state is likely to be realized in non-magnetic double-perovskite iridates.

However, if superexchange, which involves the excited magnetic $J = 1$ and $J = 2$ states, is strong enough to compete with the singlet-triplet splitting caused by spin-orbit coupling, the on-site wave function becomes a superposition of $J = 0$ and $J = 1$ and acquires a magnetic moment that can order.

A possible candidate for this excitonic magnetism is given by the the two-dimensional square-lattice Ca_2RuO_4. Experiments revealed an antiferromagnetic insulting phase for low temperatures. Additionally, the low-temperature phase of Ca_2RuO_4 is accompanied by a rather strong tetragonal crystal field that flattens the RuO_6 octahedra. It lowers the xy-orbital and experiments as well as numerical approaches indicate its nearly full occupation, suggesting a more conventional $S = 1$ spin order. On the other hand, magnetic excitations are better explained by the excitonic picture.

We use a three-orbital Hubbard-like model on a two-dimensional square lattice containing various hoppings, on-site interaction, spin-orbit coupling and tetragonal crystal field to investigate the impact of these interactions on the emergence of magnetism. We apply the Variational Cluster Approximation to address long-range order and spontaneous symmetry breaking. It requires the solution of a small cluster system achieved by exact diagonalization. The self-energy of the cluster is then inserted into the one-particle Green's function of the thermodynamic limit to obtain the grand potential. According to self-energy functional theory, the thermodynamic grand potential can then be optimized by varying the one-particle parameters used to obtain the cluster self energy. In particular, one can add fictitious symmetry-breaking Weiss fields that act only on the reference system and are not included in the thermodynamic limit Green's functions.

If a symmetry-broken self energy optimizes the grand potential of the fully symmetric Hamiltonian, one can infer spontaneous symmetry breaking. It has been highly successful in describing angle-resolved photoemission spectroscopy for strong SOC in Sr_2IrO_4. By applying several Weiss fields, we find spin and orbital ordered magnetic regimes as well as a paramagnetic phase depending on the interplay of the interactions. Further, we calculate expectation values of the ionic on-site states and hole densities in the magnetic regimes and in the absence of Weiss fields which allows us to characterize the lattice ground state. Further, we show one-particle spectral densities that can in principle be compared to angle-resolved photoemission spectroscopy.

The excitonic magnetism is firstly studied on a simple model containing only hopping, on-site interactions and spin-orbit coupling. We find an antiferromagnetic stripy phase with spin and orbital order for weak spin-orbit coupling and an antiferromagnetic checkerboard regime with excitonic magnetism for intermediate spin-orbit coupling. Stronger spin-orbit coupling suppresses the ordering.

The interplay of spin-orbit coupling and tetragonal crystal field alters the magnetic phases a bit. The tetragonal crystal field causes a reorientation of the antiferromagnetic spin order and imposes a rather strong orbital polarization. Nevertheless, the excitonic magnetism is present for intermediate tetragonal crystal field and is only suppressed for stronger tetragonal crystal field. Even for larger tetragonal crystal field, spin-orbit coupling plays a crucial role by driving the system into the paramagnetic phase.

Using density-functional theory and projections onto Wannier states, realistic parameters for Ca_2RuO_4 are derived and combined with recent experimental data to model the magnetism in Ca_2RuO_4. We find that it falls into the excitonic regime despite its strong orbital polarization with nearly filled xy-orbital. However, the strength of spin-orbit coupling is quite delicate as the excitonic magnetism applies only when spin-orbit coupling is of the order of the hopping amplitudes. For smaller spin-orbit coupling there is spin-1 magnetism without excitonic character while larger spin-orbit coupling stabilizes a non-magnetic state.

Contents

List of abbreviations

AFM Antiferromagnetic

CPT Cluster Perturbation Theory

DFT Density Functional Theory

ED Exact Diagonalization

FO Ferro-Orbital

GKA Goodenough-Kanamori-Anderson

PM Paramagnetic

SOC Spin-Orbit Coupling

TCF Tetragonal Crystal Field

VCA Variational Cluster Approximation

1 Introduction

1.1 Motivation

An important driver for the interest in the interplay of spin-orbit coupling (SOC) and electronic correlations is the search for topologically nontrivial phases like topological Mott insulators [53] and spin liquids [8]. While the prominent $3d$ metals, e. g. iron, nickel and copper, are usually understood to have rather weak SOC, more promising candidates are found in the $5d$ and $4d$ transition metal oxides where SOC is stronger. Especially, the electronic configurations $4d^4$, $4d^5$, $5d^4$ and $5d^5$, as appear in transition metal oxides containing Ru^{4+}, Ir^{5+} and Ir^{4+}, reveal intriguing ground states and magnetic phenomena [58, 75].

The impact of SOC is particularly transparent in t_{2g}^5 systems. Here, orbital angular momentum $L = 1$ and spin momentum $S = 1/2$ are coupled by SOC to total momentum J with a doublet $J = 1/2$ and a quartet $J = 3/2$ [30]. With five t_{2g} electrons, the $J = 3/2$ levels are completely and the $J = 1/2$ level is half-filled. The interplay of on-site interactions and SOC then yields a Mott insulator where the single hole in the doublet $J = 1/2$ can order. The single-layer square-lattice compound Sr_2IrO_4 has been established as a prime example for such spin-orbit driven Mott physics [6]. The resulting effective single-band description focusing on the hole in the $J = 1/2$ states is even robust enough to survive doping, where Fermi-arcs [36] and hints of superconductivity [37] have been reported. In a honeycomb geometry, the magnetic anisotropies due to SOC are of a form similar to Kitaev's spin-liquid model [39], so that α-$RuCl_3$ and similarly structured Ir compounds are candidates for spin liquids [70, 74].

The situation is rather different regarding systems with two holes. For very strong SOC, J-J-coupling might be applicable. The $J = 1/2$ band is then doubly occupied, leading to a singlet $J = 0$. Non-magnetic double-perovskite iridates [18, 52] likely realize a singlet ground state and their SOC might be strong enough to push them into this regime of J-J-coupling [22].

For intermediate SOC, theoretical predictions [31, 47] still argue that SOC gives an ionic ground state with $J = 0$. However, the gap to a triplet of excited states is here smaller, see Chap. 2. If superexchange, which involves the $J = 1$ and $J = 2$ states, is strong enough to compete with the singlet-triplet splitting caused by SOC, the on-site wave function becomes a superposition of $J = 0$ and $J = 1$ and acquires a magnetic moment that can order [31, 47]. Such excitonic antiferromagnetism has been found in

simulations of a one-dimensional three-orbital model using density matrix renormalization group [29], as well as in infinite dimensions using dynamical mean field theory [62].

A possible candidate for excitonic antiferromagnetism is given by the the square-lattice t_{2g}^4 ruthenate Ca_2RuO_4 which is in AFM insulting phase for low temperatures [7, 41]. Experiments [28] revealed a global maximum of the spin-wave dispersion found at the center of the first Brillouin zone which is in sharp contrast to a Heisenberg antiferromagnet and has been interpreted as a signature of such excitonic magnetism in Ca_2RuO_4 [22, 67, 77].

However, an alternative picture of Ca_2RuO_4 is that of an orbitally polarized $S = 1$ system. Its low-temperature phase is characterized by a shortened c-axis [2, 17, 49, 77] and an AFM order with moments aligned parallel to the layers [7]. This tetragonal crystal field (TCF) lowers the energy of the xy-orbital. Experiments [15] as well as numerical approaches [13, 14, 21, 44] indicate its nearly full occupation. Based on *ab initio* calculations [78], that in turn agree with angle-resolved photoemission spectroscopy [69], the yz- and xz-orbitals are then both approximately half-filled and form a spin $S = 1$ that orders supporting a more conventional explanation for the magnetism. SOC is here included as a correction rather than a driver [41].

We use a three-orbital Hubbard-like model containing various hoppings, on-site interaction, SOC and TCF to treat the correlations of four electrons per site on a two-dimensional square lattice. Further, we present several atomic models describing the t_{2g}^4 ground state in different limits that help characterizing the lattice ground state. While density matrix renormalization group is suited for one dimension, dynamical-mean-field-theory calculations were not able to reach the necessary low temperature needed for antiferromagnetic (AFM) order in material specific calculations [5]. We will thus employ the Variational Cluster Approximation (VCA) [54] to address the debate between spin-1 and excitonic magnetism and to classify the role of SOC.

Since we are interested in symmetry-broken states, the VCA is a useful method as it is able to address long-range order and symmetry breaking on the lattice. It has been highly successful in describing angle-resolved photoemission spectroscopy for strong SOC in Sr_2IrO_4 [72]. VCA requires the solution of a small cluster system achieved by exact diagonalization (ED). The self-energy of the cluster is then inserted into the one-particle Green's function of the thermodynamic limit to obtain the grand potential. According to self-energy functional theory [56], the thermodynamic grand potential can then be optimized by varying the one-particle parameters (e. g. hopping, chemical potential, ...) used to obtain the cluster self-energy. In particular, one can add fictitious symmetry-breaking Weiss fields that act only on the reference system and are not included in the thermodynamic limit Green's functions. If a symmetry-broken self-energy optimizes the grand potential of the fully symmetric Hamiltonian, one can infer spontaneous symmetry breaking.

We present phase diagrams and discuss the character of the ordered regimes where spin

and orbital orders are simultaneously present. Using models in the absence of SOC and in the strong coupling regime with and without TCF, we are able to derive a SOC-TCF phase diagram. Using density functional theory (DFT) and projections onto Wannier states, realistic parameters for Ca_2RuO_4 are derived and combined with recent experimental data [22] to classify the magnetism in Ca_2RuO_4. Further, we show one-particle spectral densities that can in principle be compared to angle-resolved photoemission spectroscopy.

1.2 Outline

The thesis is organized as follows. In Chap. 2, we provide an overview of the electronic properties of $5d^4$ and $4d^4$ transition metal oxides regarding the crystal structure and the resulting model including hopping, SOC and on-site interactions. As t_{2g}^4 systems are the main focus of this thesis, we discuss the interaction of the two holes per site with five different atomic models for several limits of interaction relations. A general overview of Ca_2RuO_4 is given, which is a well-studied compound and serves as an example that we will model and to which we will compare our results. The calculations of the two-dimensional lattice models are performed using VCA. As it is especially useful for the investigation of symmetry-broken systems, we discuss its application to our model systems.

Using VCA, we investigate in Chap. 3 a simplified model where SOC and superexchange compete leading to magnetic and non-magnetic regimes with spin and orbital orderings. To characterize the lattice ground state, we calculate orbital occupations and expectation values in both regimes and find excitonic magnetism. By increasing SOC, the strongly coupled regime is investigated as likely to be realized in the non-magnetic double-perovskite iridates. Additionally, we study the impact of the hopping anisotropy, which is characteristic for t_{2g} systems, in the excitonic regime.

Chapter 4 focuses on the interplay of SOC and TCF. We present the magnetic and non-magnetic regimes emerging for different strengths of SOC and TCF and discuss the spin and orbital orders.

In Chap. 5, we present a simplified model for Ca_2RuO_4 which is extended to a more realistic one step by step to identify the crucial interactions for the emergence of magnetism. Further, we examine the role of SOC for the excitonic magnetism in Ca_2RuO_4.

In Chap. 6, we summarize our work in the form of a SOC-TCF phase diagram and give an outlook on future tasks.

2 Model and Methods

In this chapter, the basic aspects and methods underlying this thesis are presented. Section 2.1 provides an overview of the features of transition metal oxides that are relevant to our investigations. We especially focus on $5d^4$ and $4d^4$ systems in particular t_{2g}^4, and the role of SOC, hopping and multi-orbital interaction within these systems. Further, we present five atomic models to describe the complex interplay of two holes in the t_{2g} subspace for different limits. In Sec. 2.2, a general overview of Ca_2RuO_4 is given which is a well-studied compound and serves as an example which we will model and to which we will compare our results. Finally, in Sec. 2.3 the numerical approaches, namely the Cluster Perturbation Theory (CPT) and the VCA, are explained shortly. Moreover, their application to our model system with symmetry-breaking fields is discussed.

2.1 t_{2g}^4 Systems and their electronic Properties

In the atomic limit, d-orbitals have orbital momentum $l = 2$ and together with the electron spin $s = 1/2$ this leads to a tenfold degeneracy. Within the octahedral oxygen structure typical for transition metal oxides, orbital degeneracy is lifted by cubic crystal field splittings [26, 32]. The d-orbitals with large amplitude in direction of the principle axes, namely $d_{x^2-y^2}$ and d_{z^2}, form the e_g subspace, whereas d_{xy}, d_{yz} and d_{xz} build the lower lying t_{2g} subspace separated by $10Dq \approx 2 - 3\,\mathrm{eV}$. As this splitting is much larger than any other interaction, except Coulomb interaction $U \approx 2\,\mathrm{eV}$, we neglect here the e_g states. For d^4 and d^5 configurations there are four and five electrons in the t_{2g} subspace, respectively.

Depending on the geometry of the surrounding ligands there are different types of crystal field splittings for two-dimensional perovskite structures like tetragonal or orthorhombic splittings. In the low-temperature phase of Ca_2RuO_4 the oxygen octahedra are flattened along the c-axis perpendicular to the lattice plane. This TCF splitting lifts the degeneracy of the t_{2g} orbitals by lowering d_{xy} in energy. In the hole picture, TCF Δ is given by

$$H_{\mathrm{TCF}} = \Delta \sum_{i,\sigma} c^\dagger_{ixy\sigma} c_{ixy\sigma} \tag{2.1}$$

where $c^{(\dagger)}_{ixy\sigma}$ is the annihilation (creation) operator of a hole in the xy-orbital on site i with spin σ. For flattened octahedra, TCF is always positive $\Delta > 0$. Figure 2.1 shows a sketch of the level splitting introduced by cubic and tetragonal crystal field splittings.

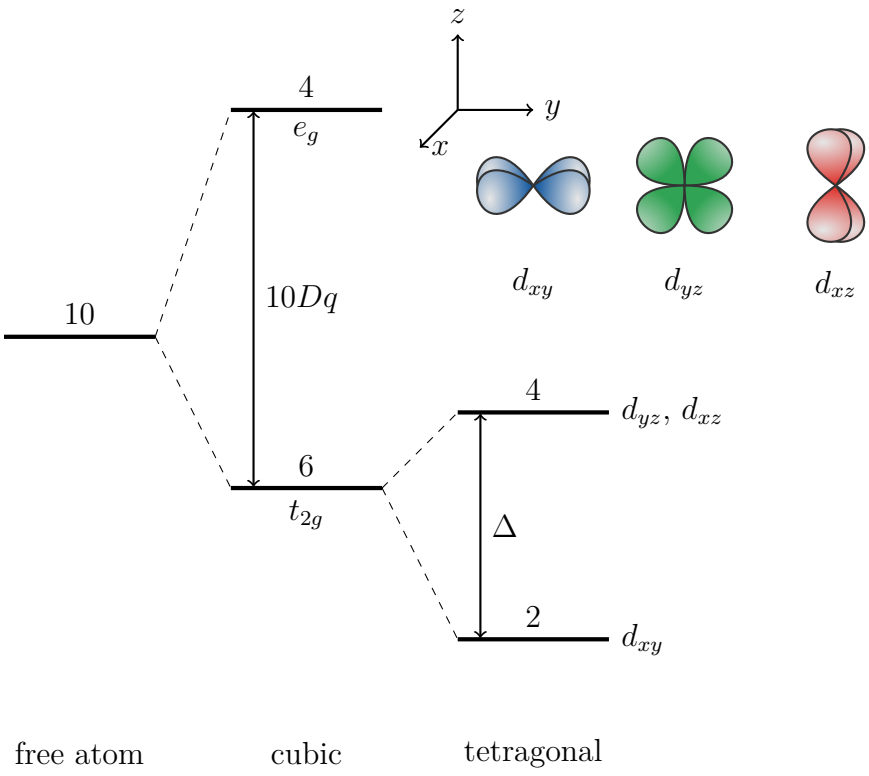

Figure 2.1: Sketch of the influence of the cubic and tetragonal crystal field on the level structure (not scaled). The d-shell of a free atom consists of ten degenerate levels. Having cubic crystal field splitting, the states are separated into lower t_{2g} and higher e_g levels by approximately $10Dq$. TCF Δ further splits the t_{2g} levels and separates d_{xy} from d_{yz} and d_{xz}. For flattened octahedra the xy-orbital is lowered in energy.

Further, the orientation of the t_{2g} orbitals d_{xy}, d_{yz} and d_{xz} within the crystal axes is shown.

To discuss electrons in narrow bands, the Hubbard model provides a very powerful and simple model [26]. As the orbitals of the lattice atoms do not overlap much, tight-binding approaches are valid. There are two processes: The hopping t_{ij} which enables the electrons to hop from site i to site j and the Coulomb repulsion U considering the on-site electronic interactions. The Hubbard Hamiltonian in second quantization is given by

$$H = \sum_{i,j,\sigma} t_{ij} c_{i\sigma}^{\dagger} c_{j\sigma} + U \sum_{i,\sigma} n_{i\sigma} n_{i\bar{\sigma}}. \tag{2.2}$$

Here, $c_{i\sigma}^{(\dagger)}$ is the annihilation (creation) operator of an electron on site i with spin σ and $n_{i\sigma} = c_{i\sigma}^{\dagger} c_{i\sigma}$ is the occupation number operator [50]. The Hubbard Hamiltonian H only includes one orbital. Multi-orbital Hubbard models contain additional interaction terms because the interaction of spins on the same site in different orbitals has to be taken into account. There, Hund's rule applies which tries to maximize spin and angular momentum on each site. The multi-orbital on-site interaction will be discussed in Sec. 2.1.3. Longer-range inter-site interactions are not included here.

2.1.1 Spin-Orbit Coupling and its Influence on t_{2g}^5 Mott Insulators

SOC is a relativistic effect that links the orbital angular momentum $\boldsymbol{l}$ and spin $\boldsymbol{s}$ of an electron. For strongly correlated $3d$ compounds, it is usually assumed to be a small perturbation. However, it grows fast with the atomic number Z and is hence crucial for $5d$ transition metal oxides like iridates [58, 75]. While several energy scales are involved, such as kinetic energy, electronic interaction and various crystal field splittings, SOC has there been identified as essential.

Without SOC, there can be pure spin interactions leading to an isotropic magnetic exchange of Heisenberg type $\boldsymbol{S}_i \boldsymbol{S}_j$ [32]. The spin space has no connection to the real space or to the real directions of the crystal. By coupling spin and orbital degrees of freedom, SOC λ creates a link between the spin orientation $\boldsymbol{s}$ and the orbital angular momentum $\boldsymbol{l}$ connected to the crystal lattice and determines a magnetic anisotropy. The effects can be described by the one-particle operator

$$H_{\mathrm{SOC}} = \lambda \boldsymbol{l} \boldsymbol{s}. \tag{2.3}$$

As the cubic crystal field splitting widely separates the e_g and t_{2g} manifolds, we restrict ourselves to the three-orbital model with the t_{2g} orbitals d_{xy}, d_{yz} and d_{xz}. The components of the angular momentum l_i $(i = x, y, z)$ projected into the t_{2g} subspace satisfy the relation $[l_\alpha, l_\beta] = -\mathrm{i}\varepsilon_{\alpha\beta\gamma} l_\gamma$. This differs from the angular momentum algebra for $l = 1$ only by a minus sign. Hence, there is a correspondence between t_{2g} and p orbitals [68] and the SOC operator Eq. (2.3) reads

$$H_{\mathrm{SOC}} = \lambda \boldsymbol{l}_{t_{2g}} \boldsymbol{s} = -\lambda \boldsymbol{l}_p \boldsymbol{s}. \tag{2.4}$$

In contrast to p-orbitals, the hierarchy of states in energy is reversed due to the minus sign, i. e. the electrons favor large total angular momentum.

Using this effective $l = 1$ scheme, the SOC Hamiltonian can be expressed in second quantization using the cubic t_{2g} basis by [11, 71]

$$\begin{aligned} H_{\mathrm{SOC}} &= \lambda \sum_{\substack{\alpha,\beta \\ \sigma,\sigma'}} \langle \alpha\sigma | \boldsymbol{l}_{t_{2g}} \boldsymbol{s} | \beta\sigma' \rangle \, c^\dagger_{\alpha\sigma} c_{\beta\sigma'} \\ &= -\lambda \sum_{\substack{\alpha,\beta \\ \sigma,\sigma'}} \langle \alpha | \boldsymbol{l}_p | \beta \rangle \, \langle \sigma | \boldsymbol{s} | \sigma' \rangle \, c^\dagger_{\alpha\sigma} c_{\beta\sigma'} \\ &= \frac{\mathrm{i}\lambda}{2} \sum_{\substack{\alpha,\beta,\gamma \\ \sigma,\sigma'}} \varepsilon_{\alpha\beta\gamma} \tau^\alpha_{\sigma\sigma'} c^\dagger_{\beta\sigma} c_{\gamma\sigma'}. \end{aligned} \tag{2.5}$$

$c^\dagger_{\beta\sigma}$ creates an electron in orbital β ($\beta = xy$, yz, xz) with spin σ ($\sigma = \uparrow, \downarrow$). The matrix elements of the spin operator $\boldsymbol{s}$ are given by $\boldsymbol{\tau}/2$ where $\boldsymbol{\tau}$ is the vector of the Pauli matrices σ_k ($k = x, y, z$). The matrix elements of the components of the orbital angular momentum operator are in case of the p-orbitals $\langle \alpha | \boldsymbol{l}^k_p | \beta \rangle = -\mathrm{i}\varepsilon_{k\alpha\beta}$ where $k, \alpha, \beta \in \{yz, xz, xy\}$ in the t_{2g}-p correspondence. In matrix notation H_{SOC} reads [73]

$$H_{\mathrm{SOC}} = \frac{\lambda}{2} \boldsymbol{c}^\dagger \begin{pmatrix} 0 & -\mathrm{i}\sigma_z & \mathrm{i}\sigma_y \\ \mathrm{i}\sigma_z & 0 & -\mathrm{i}\sigma_x \\ -\mathrm{i}\sigma_y & \mathrm{i}\sigma_x & 0 \end{pmatrix} \boldsymbol{c} \tag{2.6}$$

with

$$\boldsymbol{c} = (c_{yz\uparrow}, c_{yz\downarrow}, c_{xz\uparrow}, c_{xz\downarrow}, c_{xy\uparrow}, c_{xy\downarrow}). \tag{2.7}$$

The crucial role of SOC becomes evident for example in iridates with d^5 configuration. Materials like Sr_2IrO_4 and Ba_2IrO_4 were naively expected to be in a metallic state due to the odd number of electrons. Since the cubic crystal field splitting is large enough, the t^5_{2g} subspace is in a low-spin state with a partially filled band and thus the system would be a metal according to the band picture, see Fig. 2.2 (a).

While very strong on-site interactions might still induce an insulating gap, cf. Fig. 2.2 (b), the needed interaction strength is unrealistic. Due to their larger orbital wave function, effective on-site interactions for $5d$ orbitals are weaker than for $3d$. Moreover, Sr_2RhO_4 is indeed a normal metal [33]. However, Sr_2IrO_4 and Ba_2IrO_4 proved to be insulating with weak ferromagnetism [9].

That is the point where SOC becomes important. Pure SOC couples orbital angular momentum $l = 1$ and spin $s = 1/2$ to total momentum $j = 1/2$ and $j = 3/2$. This splits the t_{2g} orbitals into a doublet with $j = 1/2$ and quartet with $j = 3/2$ [68], see Fig. 2.2 (c). Having five electrons the $j = 3/2$ and $j = 1/2$ bands are fully and half-filled, respectively. Now, even smaller U is able to open a Mott gap, cf. Fig. 2.2 (d), driving the system into a Mott insulating state. Experimental studies [33, 34] show that the system is well described by the novel j-states.

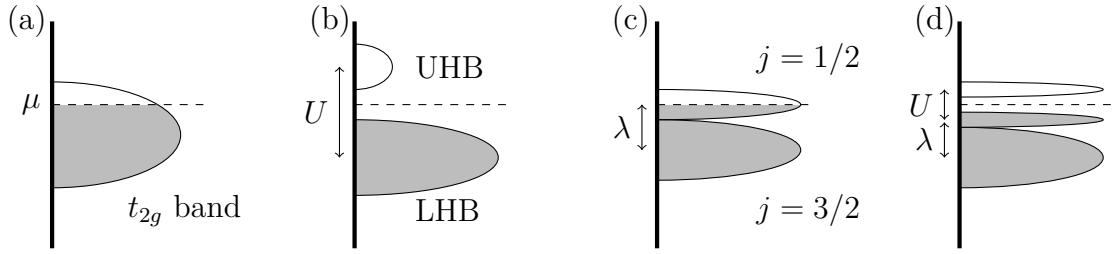

Figure 2.2: Density of states for different interaction scenarios in t_{2g}^5 systems based on an illustration in [33]. The chemical potential μ determines the band filling (gray color). The system in (a) without interaction is supposed to be a metal. Adding (b) an unrealistic large Coulomb interaction U generates a fully occupied lower Hubbard band (LHB) and an empty upper Hubbard band (UHB). For strong SOC λ (c) the band is split into a fully occupied $j = 3/2$ quartet and a half-filled $j = 1/2$ doublet. Now, even smaller U (d) opens a Mott gap and generates a Mott insulator.

2.1.2 Hopping

As previously discussed, the transition metal ions are surrounded by oxygen octahedra. In this thesis, we focus on two-dimensional square lattices where the octahedra are corner sharing ordered with 180° bonds between the transition metal ions, see Fig. 2.3. The hopping processes are mediated by the oxygen atoms but as this is only an intermediate state we neglect their presence in the following.

The strongest hopping contribution is given between two orbitals whose lobes point towards the oxygen atom. As sketched in Fig. 2.3 (a), the xz- and yz-orbital lobes point along the x- and the y-direction, respectively. This results in a strong hopping t_{xz} and t_{yz} along this bond. Due to its symmetry, the xy-orbital hops in both directions with strength t_{xy}, see Fig. 2.3 (b). In summary, regarding only the strongest hopping contributions between neighboring sites, just two orbitals are active on a given bond [27].

To observe the dispersion, we calculate the one-particle spectral density $A(\boldsymbol{k}, \omega)$ given by the CPT one-particle Green's function, which will be explained in Sec. 2.3, see Eq. (2.46). The one-particle spectral densities $A(\boldsymbol{k}, \omega)$ of the hoppings t_{xy}, t_{yz} and t_{xz} are depicted in Fig. 2.4 along the path in the Brillouin zone given in Fig. 2.5. Figure 2.4 (a) shows the averaged superposition of all three orbitals while (b)-(d) show each orbital separately. The spectra directly reflect the hopping restrictions as the d_{xy} spectrum is two-dimensional while the d_{yz} and d_{xz} spectra are only one-dimensional.

DFT calculations on Ca_2RuO_4 [63] reveal that especially for the xy-orbitals next-nearest neighbor hoppings t_{xy}^{NNN} are relevant, too. Furthermore, the DFT calculations indicate that a non-negligible hopping $t_{xy,xz}$ occurs between the xy- and the xz-orbitals

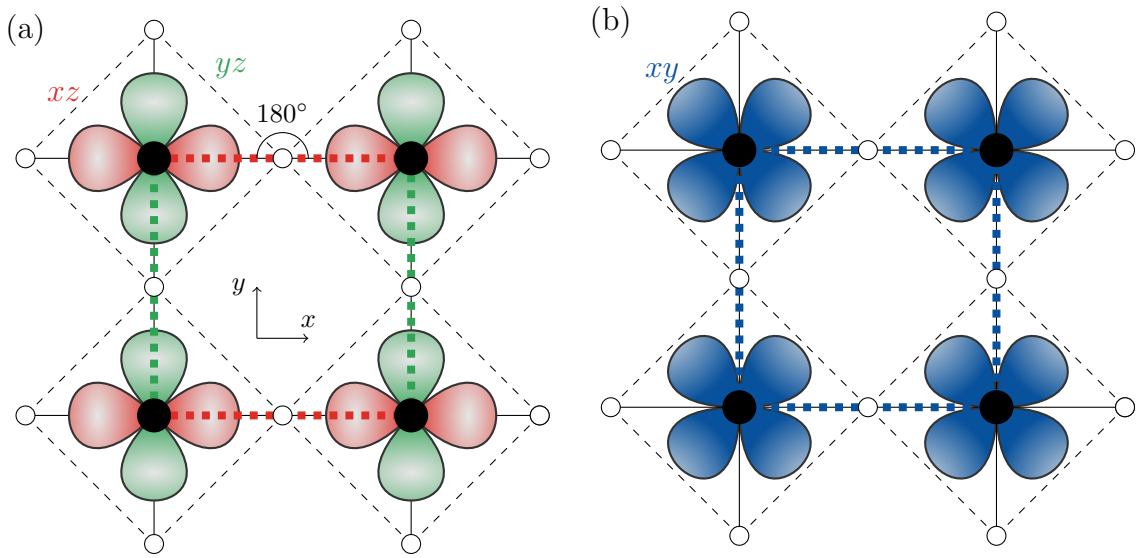

Figure 2.3: Corner-sharing octahedra of oxygen atoms (white dots) surrounding the transition metal ions (black dots) form a 180° bond. The hopping is mediated by the oxygen atoms. Regarding only the strongest hopping contributions between neighboring sites, just two orbitals are active for a given bond. (a) Hopping between xz- and yz-orbitals along a x- and y-bond marked by dashed lines in the corresponding color. The hopping in the other directions is significantly smaller. (b) Hopping between xy-orbitals along a x- and y-bond.

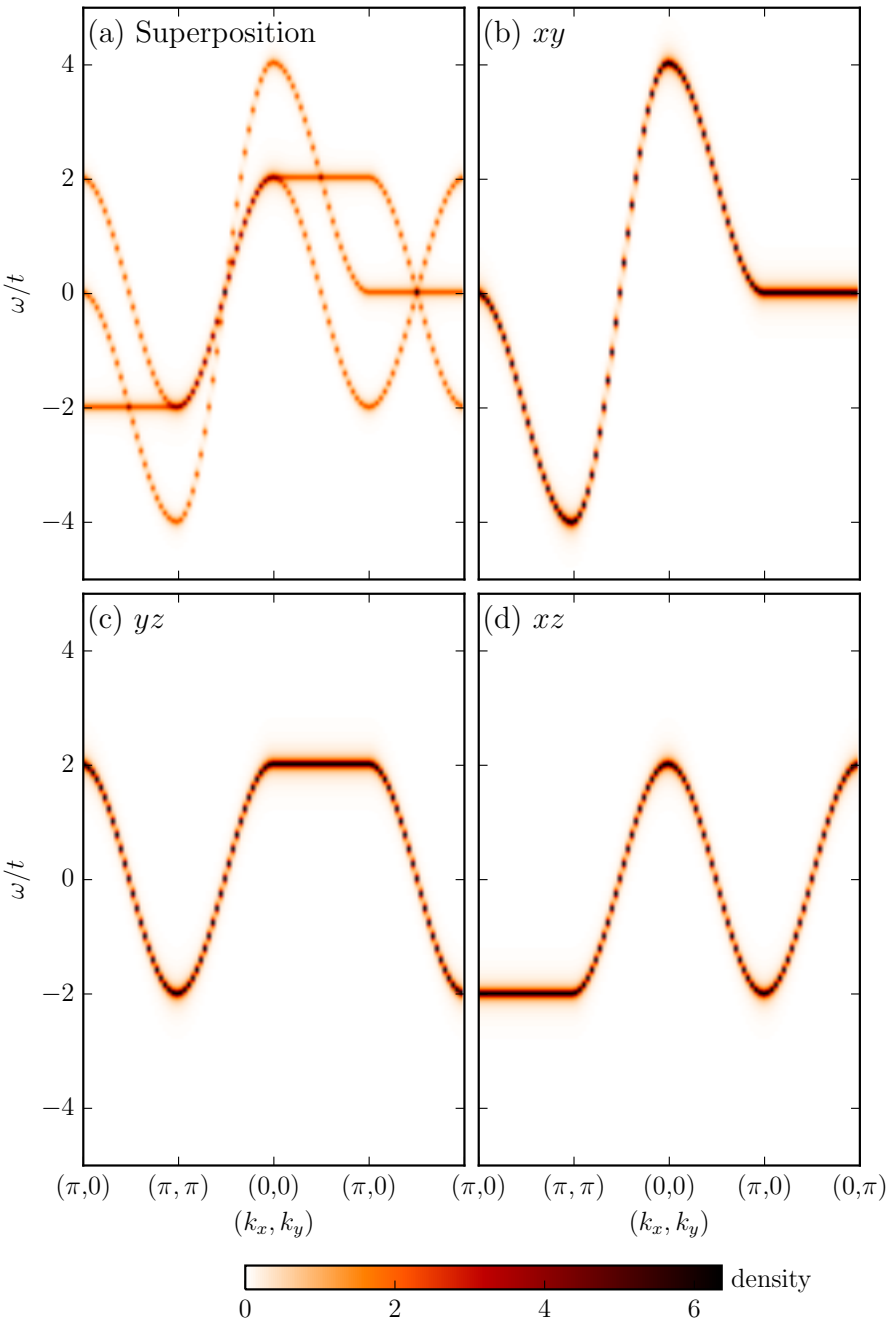

Figure 2.4: Spectral density $A(\boldsymbol{k}, \omega)$ for the hopping contributions $t_{xy} = t_{xz} = t_{yz}$ without further interactions. (a) The averaged superposition of all three orbitals and (b)-(d) each orbital individually are shown. The path in the Brillouin zone is depicted in Fig. 2.5. The xy-orbital shows a two-dimensional dispersion as the hopping is allowed in two directions. The d_{yz} and d_{xz} dispersions are only one-dimensional due to the hopping restrictions.

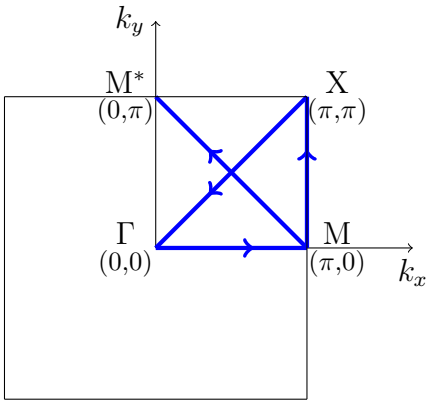

Figure 2.5: Sketch of the path through the two-dimensional Brillouin zone of a square lattice. The path starts at the M point ($k_x = \pi, k_y = 0$) moves on to X (π, π) and Γ (0,0), then back to M and ends in M* $(0, \pi)$. As the system is rotational invariant it is sufficient to focus on one quarter of the whole Brillouin zone. Along this path the spectral densities of the system are calculated.

in x-direction. It represents a small orthorhombic distortion of the lattice. The prohibited hopping of xz- or yz-orbitals in y- or x-direction is characteristic for t_{2g} orbitals. However, in real materials small hoppings occur nevertheless. We introduce an "orthogonal" hopping $t^{\perp}$, which allows the yz- and xz-orbital to hop in x- and y- direction, respectively.

In summary, the hopping consists of four processes in descending strength: The nearest neighbor hopping t_α ($\alpha = xy, yz, xz$) between the same orbitals in selected directions, the next-nearest neighbor hoppings t_{xy}^{NNN} for the xy-orbital, the hopping $t_{xy,xz}$ between the xy- and the xz-orbitals only in x-direction and finally the weak hopping $t_\alpha^{\perp}$ ($\alpha = yz, xz$) in orthogonal direction to the lobes. Further, the electron hopping is always spin preserving. Eventually, the kinetic Hamiltonian written in energy space

$$H_{\text{kin}} = \sum_{\boldsymbol{k},\alpha,\beta,\sigma} \varepsilon_{\boldsymbol{k}}^{\alpha\beta} c_{\boldsymbol{k}\alpha\sigma}^{\dagger} c_{\boldsymbol{k}\beta\sigma} \tag{2.8}$$

contains all hoppings within the dispersion relation $\varepsilon_{\boldsymbol{k}}^{\alpha\beta}$. Here, $c_{\boldsymbol{k}\alpha\sigma}^{(\dagger)}$ is the annihilation (creation) operator of an electron with spin σ ($\sigma = \uparrow, \downarrow$) and orbital α ($\alpha = xy$, yz, xz) with momentum $\boldsymbol{k}$. $c_{\boldsymbol{k}\alpha\sigma}$ is the Fourier transform of $c_{i\alpha\sigma}$ where i denotes the site index on the two-dimensional lattice. For the hoppings listed above, the non-zero dispersion relation parts are

$$\begin{aligned}
\varepsilon_{\boldsymbol{k}}^{xy} &= -2t_{xy}(\cos k_x + \cos k_y) - 4t_{xy}^{NNN} \cos k_x \cos k_y, \\
\varepsilon_{\boldsymbol{k}}^{yz} &= -2t_{yz} \cos k_y - 2t_{yz}^{\perp} \cos k_x, \\
\varepsilon_{\boldsymbol{k}}^{xz} &= -2t_{xz} \cos k_x - 2t_{xz}^{\perp} \cos k_y.
\end{aligned} \tag{2.9}$$

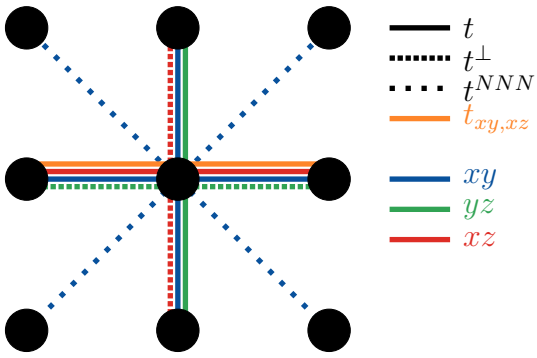

Figure 2.6: Sketch of the hoppings between transition metal oxides (black dots) given by the dispersion relation $\varepsilon_{\boldsymbol{k}}^{\alpha\beta}$ in Eq. (2.9) and Eq. (2.10). The hoppings t, $t^{\perp}$ and t^{NNN} are depicted by solid and dotted lines, respectively, while the line colors denote the involved orbitals. The hopping $t_{xy,xz}$ which includes xy- and xz-orbitals is painted in orange.

for the same two orbitals orbitals $\alpha = \beta$ and

$$\varepsilon_{\boldsymbol{k}}^{xy,xz} = \varepsilon_{\boldsymbol{k}}^{xz,xy} = -2t_{xy,xz}\cos k_x. \tag{2.10}$$

for the hopping between the xy- and the xz-orbitals. An overview of the hopping geometry is sketched in Fig. 2.6.

2.1.3 Multi-Orbital Interaction

The Hubbard Hamiltonian introduced in Eq. (2.2) is suitable for one-band systems and contains hopping between neighboring sites and the Coulomb interaction within one orbital. Multi-orbital systems are far more complex than one-band systems as there is an additional degree of freedom and thus the interaction of the electrons between two orbitals of the same site has to be considered. First, there is the Coulomb interaction U which depends on the orbital occupation on the given site. It defines the largest interaction energy scale and describes the interaction of two electrons with opposite spin occupying the same orbital. When the two electrons are on different orbitals their wave functions overlap less and therefore they interact with weaker strength denoted by U'. Second, Hund's coupling J_{H} is sensible to the spin direction of the electrons favoring a maximal total spin. Therefore, spins are forced to point in the same direction. Its origin is again the Coulomb repulsion which is reduced if the spins are parallel and avoid each other. Third, Hund's rule maximizes the total angular momentum which results in a maximally antisymmetric wave function supporting the maximal spin.

In the symmetric Kanamori form, the on-site Coulomb interactions [19, 51, 68] are

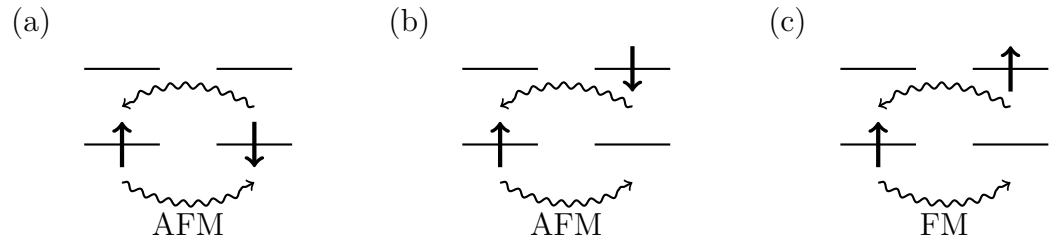

Figure 2.7: Cartoon picture of the superexchange processes and the GKA rules. (a) For superexchange between half-filled orbitals only AFM exchange is possible. The ferromagnetic exchange is forbidden by the Pauli principle. For superexchange between an occupied and an empty orbital, there can be (b) an AFM exchange as well as a (c) ferromagnetic exchange. The superexchange is mediated by an oxygen orbital which is neglected in this cartoon picture.

given by

$$\begin{aligned} H_{\text{int}} = U \sum_{i,\alpha} n_{i\alpha\uparrow} n_{i\alpha\downarrow} + \frac{U'}{2} \sum_{i,\sigma} \sum_{\alpha \neq \beta} n_{i\alpha\sigma} n_{i\beta\bar{\sigma}} \\ + \frac{1}{2}(U' - J_{\text{H}}) \sum_{i,\sigma} \sum_{\alpha \neq \beta} n_{i\alpha\sigma} n_{i\beta\sigma} \\ - J_{\text{H}} \sum_{i,\alpha \neq \beta} (c^{\dagger}_{i\alpha\uparrow} c_{i\alpha\downarrow} c^{\dagger}_{i\beta\downarrow} c_{i\beta\uparrow} - c^{\dagger}_{i\alpha\uparrow} c^{\dagger}_{i\alpha\downarrow} c_{i\beta\downarrow} c_{i\beta\uparrow}) \end{aligned} \tag{2.11}$$

with Coulomb interaction U, U' and Hund's coupling J_{H} connected via $U' = U - 2J_{\text{H}}$.

In (Mott) insulators, charge fluctuations are suppressed. Hopping is, however, still important as can be seen by considering it in second-order perturbation theory. This gives superexchange where one electron hops to the neighboring site and back. As the hopping is mediated by oxygen the superexchange process is actually a multi-step process [32]. For simplicity, we neglect the oxygens in the following and focus only on the transition metal ions.

In magnetic systems with non-negligible Hund's coupling the spins on neighboring sites are either ferromagnetically or antiferromagnetically aligned. Goodenough, Kanamori and Anderson (GKA) [32] showed that there are two principle rules concerning the superexchange processes.

The first rule concerns the hopping between two neighboring sites from a half-filled orbital to another half-filled one as for example given in Fig. 2.7 (a) for two orbitals. If the neighboring spins are ferromagnetically aligned, the superexchange is forbidden by the Pauli principle. In the AFM case, there is a rather strong AFM exchange with energy gain

$$\Delta E_{\uparrow\downarrow} = -\frac{t^2}{U}. \tag{2.12}$$

Second, we consider the hopping from an occupied orbital to an empty one. Now, there are two possible processes. If the neighboring spins are antiferromagnetically aligned, see Fig. 2.7 (b), the energy $\Delta E_{\uparrow\downarrow}$ is the same as before in Eq. (2.12). However, in the ferromagnetic case, Fig. 2.7 (c), Hund's coupling has to be taken into account and leads to the exchange energy

$$\Delta E_{\uparrow\uparrow} = -\frac{t^2}{U - J_{\mathrm{H}}}. \tag{2.13}$$

Since $J_{\mathrm{H}}/U < 1$ and therefore $\Delta E_{\uparrow\uparrow} < \Delta E_{\uparrow\downarrow}$, the ferromagnetic exchange is dominant.

Concerning d^4 systems with two holes per site, the superexchange processes are more complicated. In this case, second-order perturbation theory leads to some more energy corrections which regard also the interaction of the three spins on one site during the superexchange [16]. Further, there are orbital preserving and orbital non-preserving processes due to the pair production term in the Hund's coupling Eq. (2.11).

2.1.4 Characteristics of t_{2g}^4 Systems

The interaction of four electrons in the t_{2g} subspace leads to qualitatively quite different scenarios than the d^5 case. In contrast to the d^5 doublets $j = 1/2$ of Sec. 2.1.1, the d^4 ionic ground state is a non-magnetic singlet. Due to the interplay of Hund's coupling and SOC the orbital momenta and spins form a total angular momentum J with the singlet ground state $J = 0$ in the atomic limit. Therefore, iridate and ruthenate oxides with d^4 configuration were supposed to be non-magnetic. However, superexchange has been argued to mix in $J = 1$ states and thus allow magnetism [31, 47].

To gain a better understanding of the origin of such magnetism, we present the atomic level structure for five different limits. First, the interaction of small SOC λ and Hund's coupling J_{H} is considered. Within this so called LS-regime, J_{H}/λ is large. Here, the spins and orbital angular momenta of each particle couple to total S and L which results in a spin $S = 1$ and orbital $L = 1$ ground state. Further, the SOC forces a coupling to the total momentum $\boldsymbol{J_{LS}} = \boldsymbol{L} + \boldsymbol{S}$ that splits the ground state into a singlet, a triplet and a quintet with splittings proportional to λ. Second, if SOC gets stronger than Hund's coupling $\lambda \gg J_{\mathrm{H}}$, the distance between singlet and triplet enlarges. Within this so called jj-regime, the particles form total momenta j_i out of their l_i and s_i which are then combined to $\boldsymbol{J_{jj}}$. Third and fourth, the TCF Δ, Eq. (2.1), has to be taken into account in the LS- and the jj-regime. In the latter, we neglect Hund's coupling for simplicity. Finally, we use a Hamiltonian containing all parameters J_{H}, U, λ and Δ whose eigenstates and eigenenergies are calculated by ED on one site.

Interplay of Hund's coupling and SOC in the LS-Limit

As Hund's coupling and Coulomb interaction are in general the most dominant forces within Mott insulators, we first focus on the regime with $J_{\mathrm{H}} \gg \lambda$. To start with, no TCF is taken into account.

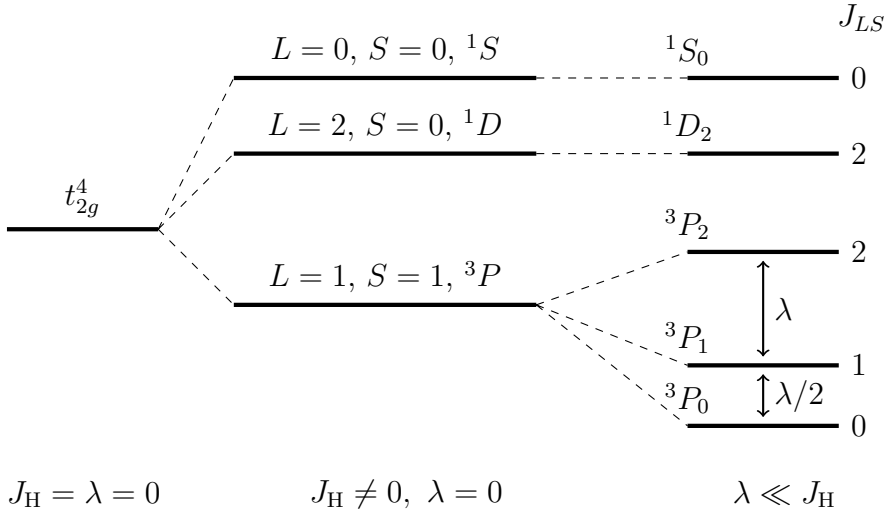

Figure 2.8: Unscaled sketch of the level splitting of the t_{2g}^4 subspace in the presence of Hund's coupling J_{H} and SOC λ in the atomic limit. On the left side, all 15 states are degenerate. Adding J_{H} the orbital and spin momenta form total L and S and the levels split into three. When SOC is taken into account, $\lambda \ll J_{\mathrm{H}}$, the orbital and spin momenta couple to total J_{LS} and the lowest level is further split into three states. The ground state $J_{LS} = 0$ is given by a non-magnetic singlet which is separated by $\lambda/2$ to a higher lying triplet $J_{LS} = 1$. The quintet $J_{LS} = 2$ is separated by λ. Note that this sketch is in the hole picture.

Figure 2.8 shows the atomic level structure of the t_{2g}^4 subspace for the hole picture. In the absence of interactions, except the cubic crystal field splitting, all 15 states of the t_{2g}^4 subspace are degenerate. Taking Hund's coupling into account, the orbital momenta $l_i = 1$ and the spin momenta $s_i = 1/2$ ($i = 1, 2$) of each of the two holes couple to total orbital momentum $L = 0, 1, 2$ and spin momentum $S = 0, 1$ with magnetic quantum numbers M_L and M_S. This basis transformation is mediated by the Clebsch-Gordan coefficients CG. For the spins and angular momenta it yields the states

$$\begin{aligned} |L, M_L\rangle &= |l_1 = 1, l_2 = 1, L, M_L\rangle \\ &= \sum_{m_{l_1}, m_{l_2}} CG(m_{l_1}, m_{l_2}, M_L)\, |l_1 = 1, m_{l_1}, l_2 = 1, m_{l_2}\rangle\,, \end{aligned} \tag{2.14}$$

$$\begin{aligned} |S, M_S\rangle &= |s_1 = 1/2, s_2 = 1/2, S, M_S\rangle \\ &= \sum_{m_{s_1}, m_{s_2}} CG(m_{s_1}, m_{s_2}, M_S)\, |s_1 = 1/2, m_{s_1}, s_2 = 1/2, m_{s_2}\rangle\,. \end{aligned} \tag{2.15}$$

The full state $|L, M_L, S, M_S\rangle$ is given by the tensor product

$$|L, M_L, S, M_S\rangle = |l_1 = 1, l_2 = 1, L, M_L\rangle \otimes |s_1 = 1/2, s_2 = 1/2, S, M_S\rangle\,. \tag{2.16}$$

As $|L, M_L, S, M_S\rangle$ must be antisymmetric, it is only possible to get $|L = 1, M_L, S = 1, M_S\rangle$, $|L = 2, M_L, S = 0, M_S\rangle$ and $|L = 0, M_L, S = 0, M_S\rangle$. The formerly degenerate states now split due to Hund's coupling into three energy levels where ${}^3P$ with $L = 1, S = 1$ is the ground state, see Fig. 2.8 in the middle. It is still ninefold degenerate.

Adding a small SOC $\lambda \ll J_{\mathrm{H}}$ the orbital and spin momentum are coupled to total angular momentum $\boldsymbol{J_{LS}} = \boldsymbol{L} + \boldsymbol{S}$ with $J_{LS} = 0, 1, 2$ again given by the Clebsch-Gordan transformation

$$|J_{LS}, M_J\rangle \equiv |L, S, J_{LS}, M_J\rangle = \sum_{M_L, M_S} CG(M_L, M_S, M_J)\, |L, M_L, S, M_S\rangle\,. \tag{2.17}$$

Note that Eq. (2.3) changes to $H_{\mathrm{SOC}} = \lambda/2\boldsymbol{LS}$ for the interaction of two particles. This results in a level splitting of the former ground state ${}^3P$ into three sublevels, see Fig. 2.8 on the right side. The ground state is now given by the singlet ${}^3P_0$ with $J_{LS} = 0$. It is separated by $\lambda/2$ to the higher lying triplet $|J_{LS} = 1\rangle$ and by $3/2\lambda$ to the quintet $|J_{LS} = 2\rangle$. In the following, we focus on the low-energy subspace ${}^3P$ as the contribution of higher levels can be neglected. As there is no splitting in terms of the magnetic quantum numbers M_J, we use

$$\begin{aligned} |J_{LS} = 0\rangle &\equiv |J_{LS} = 0, M_J = 0\rangle\,, \\ |J_{LS} = 1\rangle &\equiv \sum_{M_J=-1}^{1} |J_{LS} = 1, M_J\rangle\,, \\ |J_{LS} = 2\rangle &\equiv \sum_{M_J=-2}^{2} |J_{LS} = 2, M_J\rangle\,. \end{aligned} \tag{2.18}$$

to describe the J_{LS} states.

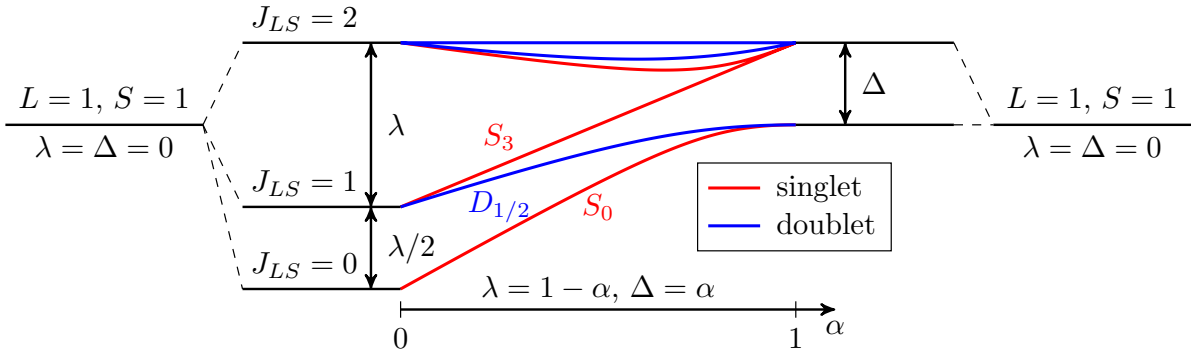

Figure 2.9: In the LS-coupling limit, the interplay of SOC λ and TCF Δ significantly influences the level structure. On the left side, the level structure for $\Delta = 0$ is the same as in Fig. 2.8. As the tuning parameter α increases, the level structure changes completely by building only singlets (red color) and doublets (blue color). On the right side, the scenario for $\lambda = 0$ results in a threefold degenerate ground state and a sixfold excited state separated by Δ.

Interplay of SOC and TCF in the LS-Limit

Adding the TCF to the LS-coupling limit reveals an interesting competition between TCF Δ and SOC λ. Figure 2.9 on the left side shows the situation discussed before with $\Delta = 0$. The states can be identified by the J_{LS} quantum number. On the right side, where $\lambda = 0$, the levels form a threefold degenerate ground state and a sixfold degenerate excited state separated by Δ. The parameter α is introduced to provide a smooth transition between those two limits by setting $\lambda = 1 - \alpha$ and $\Delta = \alpha$.

Starting on the left side, small Δ immediately starts to split the triplet and quintet into sublevels. The triplet becomes a lower doublet $D_{1/2}$ and a higher singlet S_3 for octahedra shortened along the c-axis. The former converges towards the ground state singlet S_0 while the latter joins the former quintet to form a sextet for increasing Δ. For intermediate α the structure consists only of doublets and singlets. However, the low-energy situation is given by the non-magnetic singlet S_0 and the magnetic doublet $D_{1/2}$. For increasing TCF, the splitting between those states is significantly reduced.

Interplay of SOC and Hund's coupling in the jj-Limit

In the limit of strong SOC, coupling to total momentum j dominates over the formation of total spins or total orbital angular momenta. Therefore, each particle's spin $s_i = 1/2$ and orbital momentum $l_i = 1$ ($i = 1, 2$) couple to $\boldsymbol{j}_i = \boldsymbol{l}_i + \boldsymbol{s}_i$. The quantum number j_i

can have the values $j_i = 1/2,\, 3/2$ and the corresponding states are given by

$$|l_i, s_i, j_i, m_{j_i}\rangle = \sum_{m_{l_i}, m_{s_i}} CG(m_{l_i}, m_{s_i}, m_{j_i})\, |l_i, m_{l_i}, s_i, m_{s_i}\rangle \tag{2.19}$$

using m_{j_i} as magnetic quantum number and the Clebsch-Gordan coefficients CG for the transformation between the two bases.

The two one-particle states are coupled to a single two-particle state by applying the tensor product. For the lowest state $(j_1 = 1/2, j_2 = 1/2)$ this is given by

$$\begin{aligned} |j_1 = 1/2, m_{j_1} = \pm 1/2, j_2 = 1/2, m_{j_2} = \mp 1/2\rangle \\ = |j_1 = 1/2, m_{j_1} = \pm 1/2\rangle \otimes |j_2 = 1/2, m_{j_2} = \mp 1/2\rangle\,. \end{aligned} \tag{2.20}$$

Note that the particles are not allowed to coincide in all quantum numbers. Therefore, the $\pm$ and $\mp$ signs are used in Eq. (2.20). In a similar way the states for $(j_1 = 3/2, j_2 = 1/2)$ and $(j_1 = 3/2, j_2 = 3/2)$ are built.

There is a nice pictorial way to understand why the ground state is given by $(j_1 = 1/2, j_2 = 1/2)$. Assuming that Hund's coupling is very small the two particles do not interact with each other. Remembering Sec. 2.1, there is a ground state doublet $j = 1/2$ and an excited quadruplet $j = 3/2$ for a d^5 system. As we now have two particles, we can put them both in the ground state doublet $j = 1/2$ which is then doubly and hence fully occupied. This scenario is depicted in Fig. 2.10 (a) on the left side. The excited state is given on the right side where one particle is in the $j = 3/2$ state. Transforming this into the two-particle basis, one gets the ground state $(j_1 = 1/2, j_2 = 1/2)$, see Fig. 2.10 (b). It is separated by $3\lambda/2$ from the excited $(j_1 = 3/2, j_2 = 1/2)$ state. The $(j_1 = 3/2, j_2 = 3/2)$ lies even higher and is not shown in Fig. 2.10.

In the presence of small Hund's coupling J_H, the particles start to interact and the two momenta $\boldsymbol{j_1}$ and $\boldsymbol{j_2}$ couple to a total momentum $\boldsymbol{J_{jj}}$. The new state is once more given by the Clebsch-Gordan transformation

$$|j_1, j_2, J_{jj}, M_J\rangle = \sum_{m_{j_1}, m_{j_2}} CG(m_{j_1}, m_{j_2}, M_J)\, |j_1, m_{j_1}, j_2, m_{j_2}\rangle\,. \tag{2.21}$$

and the magnetic quantum number M_J. For the ground state $(j_1 = 1/2, j_2 = 1/2)$ this results only in a renaming to $|J_{jj} = 0, M_J = 0\rangle$, see Fig. 2.10 (b) on the right side. However, the $(j_1 = 3/2, j_2 = 1/2)$ state splits into a triplet $|J_{jj} = 1\rangle$ and a quintet $|J_{jj} = 2\rangle$ separated by J_H approximately. For brevity, we only show how the triplet is constructed

$$\begin{aligned} |J_{jj} = 1, M_J\rangle = \frac{1}{\sqrt{2}}\Big(\sum_{m_{j_1}, m_{j_2}} CG(m_{j_1}, m_{j_2}, M_J)\, |j_1 = 1/2, m_{j_1}, j_2 = 3/2, m_{j_2}\rangle \\ + \sum_{m_{j_1}, m_{j_2}} CG(m_{j_1}, m_{j_2}, M_J)\, |j_1 = 3/2, m_{j_1}, j_2 = 1/2, m_{j_2}\rangle \Big) \end{aligned} \tag{2.22}$$

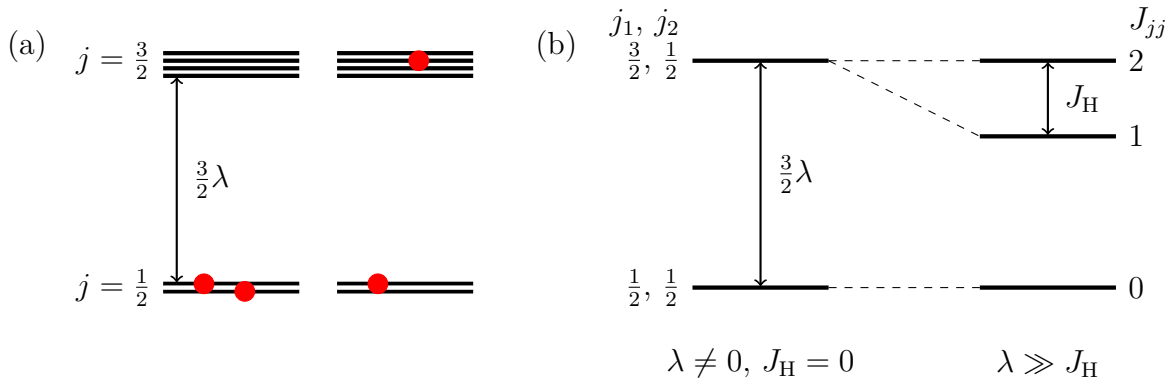

Figure 2.10: (a) In the strong SOC regime two holes are put into the d^5 ground state $j = 1/2$ on the left side. The excited state is given when one of the particles is in the $j = 3/2$ state, see right side. (b) In the two-particle scheme this leads to a singlet ground state ($j_1 = 1/2, j_2 = 1/2$) separated by $3\lambda/2$ to the excited state which is eightfold degenerate. The even higher ($j_1 = 3/2, j_2 = 3/2$) state is not shown. In the presence of small Hund's coupling, the excited states split into a quintet $J_{jj} = 2$ and a triplet $J_{jj} = 1$ which are still far above the ground state $J_{jj} = 0$ (not scaled).

Again, the magnetic quantum number M_J is irrelevant giving

$$\begin{aligned} |J_{jj} = 0\rangle &\equiv |J_{jj} = 0, M_J = 0\rangle\,, \\ |J_{jj} = 1\rangle &\equiv \sum_{M_J=-1}^{1} |J_{jj} = 1, M_J\rangle\,, \\ |J_{jj} = 2\rangle &\equiv \sum_{M_J=-2}^{2} |J_{jj} = 2, M_J\rangle\,. \end{aligned} \tag{2.23}$$

Interplay of SOC and TCF in the jj-Limit

If Hund's coupling is so small that we can neglect its influence, the interplay of TCF and SOC can be described within a one-particle scheme as the particles do not interact. In the atomic limit, the eigenstates of a Hamiltonian consisting only of SOC, Eq. (2.6), and TCF, Eq. (2.1), are given by the Kramers doublets [27, 35]. In terms of the cubic

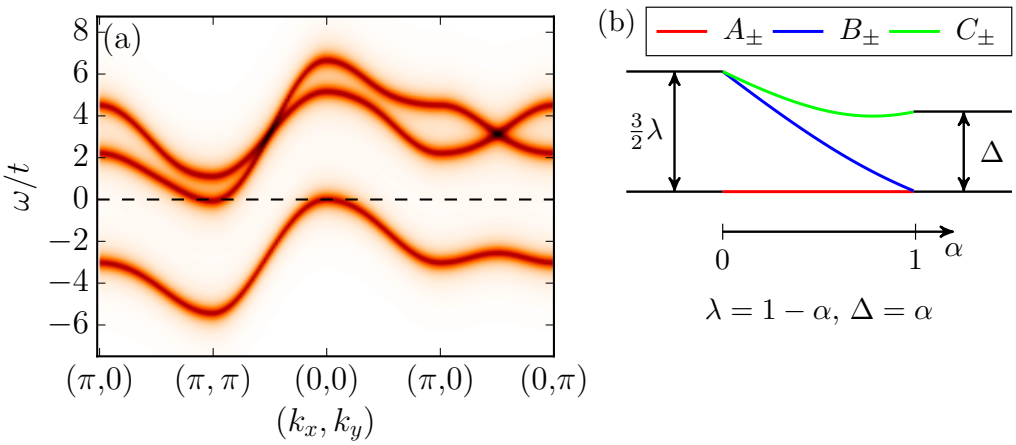

Figure 2.11: (a) CPT one-particle spectral density for SOC with hopping in the absence of further interactions along a path through the Brillouin zone. The intensity of color gives the density. (b) Level structure of the Kramers states for varying parameter $\alpha(\lambda, \Delta)$. For $\Delta = 0$, the upper doublets are degenerate which reverses for increasing Δ. In the other limit $\lambda = 0$, the ground state is fourfold degenerate.

harmonic orbitals xy, yz and xz, the Kramers doublets $A_\pm$, $B_\pm$ and $C_\pm$ are given by

$$\begin{aligned} A_\pm^\dagger &= \sin\theta c_{xy\sigma}^\dagger + \frac{\cos\theta}{\sqrt{2}}\left(\pm c_{yz\bar{\sigma}}^\dagger + \mathrm{i}c_{xz\bar{\sigma}}^\dagger\right) \\ B_\pm^\dagger &= -\sqrt{\frac{1}{2}}\left(\pm c_{yz\sigma}^\dagger + \mathrm{i}c_{xz\sigma}^\dagger\right) \\ C_\pm^\dagger &= \cos\theta c_{xy\sigma}^\dagger - \frac{\sin\theta}{\sqrt{2}}\left(\pm c_{yz\bar{\sigma}}^\dagger + \mathrm{i}c_{xz\bar{\sigma}}^\dagger\right) \end{aligned} \tag{2.24}$$

with $\pm$ denoting the pseudo spin of the Kramers doublets. The angle θ is determined by SOC λ and TCF Δ with

$$\begin{aligned} \cos\theta = \frac{1}{\sqrt{2}}\sqrt{1+\frac{\lambda/2+\Delta}{R}}, \quad \sin\theta = \frac{1}{\sqrt{2}}\sqrt{1-\frac{\lambda/2+\Delta}{R}}, \\ \text{and} \quad R = \sqrt{\frac{9\lambda^2}{4}+\Delta^2+\lambda\Delta}. \end{aligned} \tag{2.25}$$

Note that $\Delta > 0$ for flattened octahedra. The energy differences between the doublets is

$$E_{AB} = -\frac{\Delta}{2} + \frac{3\lambda}{4} + \frac{1}{2}R, \quad E_{AC} = R \tag{2.26}$$

as depicted in Fig. 2.11 (b) for a continuous transition between the two limits $\lambda = 0$ and $\Delta = 0$. In the limit of vanishing Δ the upper Kramers doublets become degenerate and

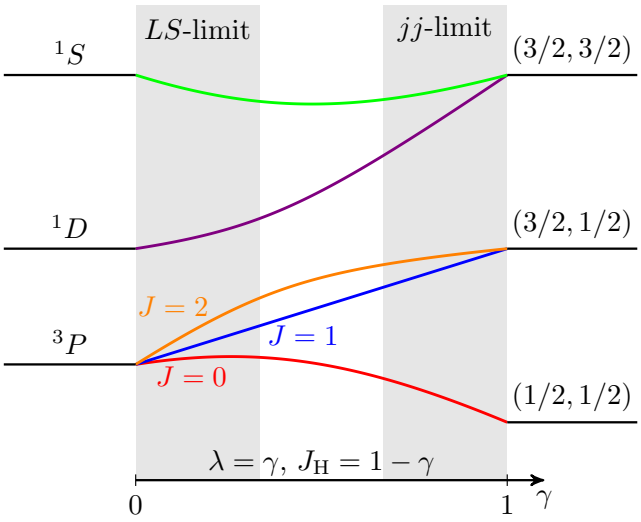

Figure 2.12: Eigenvalues of the one-site Hamiltonian consisting of SOC λ, Eq. (2.3), and Hund's coupling J_H, Eq. (2.11), calculated by ED within the limits of SOC $\lambda = 0$ and Hund's coupling $J_\mathrm{H} = 0$. There is a smooth transition between both cases. The two important regions, namely the LS- and the jj-limit, are approximately indicated by the shaded background. For the region in between, neither LS- nor jj-description fit.

the splitting is $3/2\lambda$. Figure 2.11 (a) shows the CPT one-particle spectral density for this case along a path through the Brillouin zone. The Kramers $B_\pm$ starts to split from the $C_\pm$ doublet and converges towards the ground state $A_\pm$. It results in a reversed degeneracy with energy difference Δ for $\lambda = 0$.

Full atomic Model

Any of the models so far considered all three parameters J_H, λ and Δ on equal energy scales. However, using ED on a single site, we calculate the eigenstates and eigenenergies of the atomic Hamiltonian including Hund's coupling J_H and Coulomb interaction U, Eq. (2.11), SOC λ, Eq. (2.3), and TCF Δ, Eq. (2.1). The eigenstates $|v_i\rangle$ and -energies of this 15×15-matrix are calculated using python.linalg and can be given in terms of the basis states $|b_j\rangle$

$$|v_i(J_\mathrm{H}, U, \lambda, \Delta)\rangle = \sum_j a_{ij} |b_j\rangle \tag{2.27}$$

where $|b_j\rangle = c^\dagger_{\alpha\sigma} c^\dagger_{\beta\gamma} |0\rangle$ is any state which is part of the t_{2g}^4 space. α and β are the orbitals xy, yz and xz and σ, γ denote the spins. To derive the expectation value $\langle v_i \rangle$,

explained in detail in Eq. (2.48), of an eigenstate we use the the projection

$$\begin{aligned} |v_i\rangle\langle v_i| &= \Big(\sum_k a_{ik}|b_k\rangle\Big)\Big(\sum_l a_{il}^*\langle b_l|\Big) \\ &= \sum_k a_{ik}a_{ik}^*|b_k\rangle\langle b_k| + \sum_{k,l\neq k} a_{ik}a_{il}^*|b_k\rangle\langle b_l| \\ &= \sum_k a_{ik}a_{ik}^* n_{\alpha\sigma}n_{\beta\gamma} + \sum_{k,l\neq k} a_{ik}a_{il}^* c_{\alpha\sigma}^\dagger c_{\beta\gamma}^\dagger c_{\beta'\gamma'}c_{\alpha'\sigma'} \end{aligned} \tag{2.28}$$

with n as the number operator.

The full atomic model is able to provide the connections between LS-limit, jj-limit and Kramers states. Eigenenergies for the special case of $\Delta = 0$ are shown in Fig. 2.12 interpolating between the limits of SOC $\lambda = 0$ and Hund's coupling $J_\mathrm{H} = 0$. The two regions discussed previously, namely the LS- and the jj-limit, are approximately indicated by the shaded background. For the region in between, neither LS- nor jj-description fit. The overlap between the two extreme ground states is substantial with $\langle J_{LS} = 0|J_{jj} = 0\rangle \approx 0.816$.

To investigate the influence of the TCF, the overlap of the Kramers ground state $|A_+A_-\rangle$ with the $|J_{jj} = 0\rangle$ state and the $|J_{LS} = 0\rangle$ state is calculated in Fig. 2.13. For $\Delta = 0$, the ground state description in terms of Kramers states and J_{jj} states is exactly the same as $\langle J_{jj} = 0|A_+A_-(\alpha = 0)\rangle = 1$. Therefore, $\langle J_{LS} = 0|A_+A_-(\alpha = 0)\rangle \approx 0.816$. For increasing Δ/λ the overlap stays nearly constant for $\alpha \leq 0.4$ but then drops significantly. Even $\langle J_{jj} = 0|A_+A_-\rangle$ is finally below 0.7 showing that the J_{jj} states are not able to capture the influence of TCF as already seen in Fig. 2.11 (b).

2.2 Magnetism and Features of Ca_2RuO_4 as a potential excitonic Antiferromagnet

Theoretical predictions [31, 47] for t_{2g}^4 systems argue that SOC imposes a non-magnetic ground state $J = 0$ in the atomic limit due to the coupling of spin $S = 1$ and orbital $L = 1$. This singlet ground state is likely to be realized in non-magnetic double-perovskite iridates [18, 52] which might be close to the jj-regime with doubly occupied $J = 1/2$ band [22]. Materials with more moderate SOC, however, have been argued to show excitonic magnetism [1, 31]. If superexchange, which involves the magnetic triplet $J = 1$ and quintet $J = 2$, is strong enough to compete with the singlet-triplet splitting caused by SOC, the on-site wave function becomes a superposition of $J = 0$ and $J = 1$ and acquires a magnetic moment. Square lattice Ca_2RuO_4 provides a possible realization for the emergence of such magnetism [22, 67, 77].

We briefly summarize the most important experimental observations and numerical approaches regarding Ca_2RuO_4 to derive a quantitative model for our investigations.

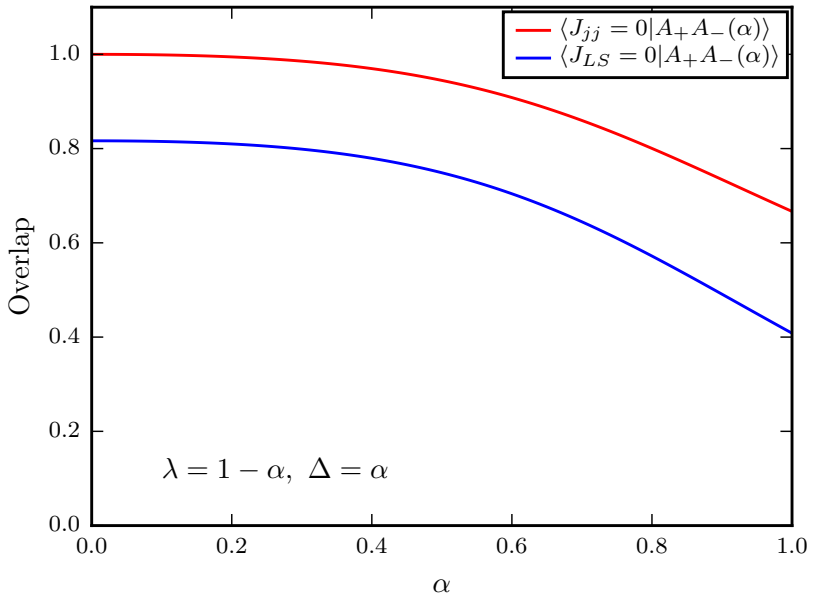

Figure 2.13: Overlap of the doubly filled Kramers ground state $|A_+A_-(\alpha)\rangle$ with the ground states $|J_{jj}=0\rangle$ and $|J_{LS}=0\rangle$ over the tuning parameter α with $\lambda = 1-\alpha$ and $\Delta = \alpha$. In the absence of TCF, $\alpha = 0$, $|J_{jj}=0\rangle$ and $|A_+A_-\rangle$ coincide while $\langle J_{LS}=0|A_+A_-(\alpha=0)\rangle \approx 0.816$. For increasing TCF, the overlap is strongly reduced and even $\langle J_{jj}=0|A_+A_-\rangle$ drops below 0.7.

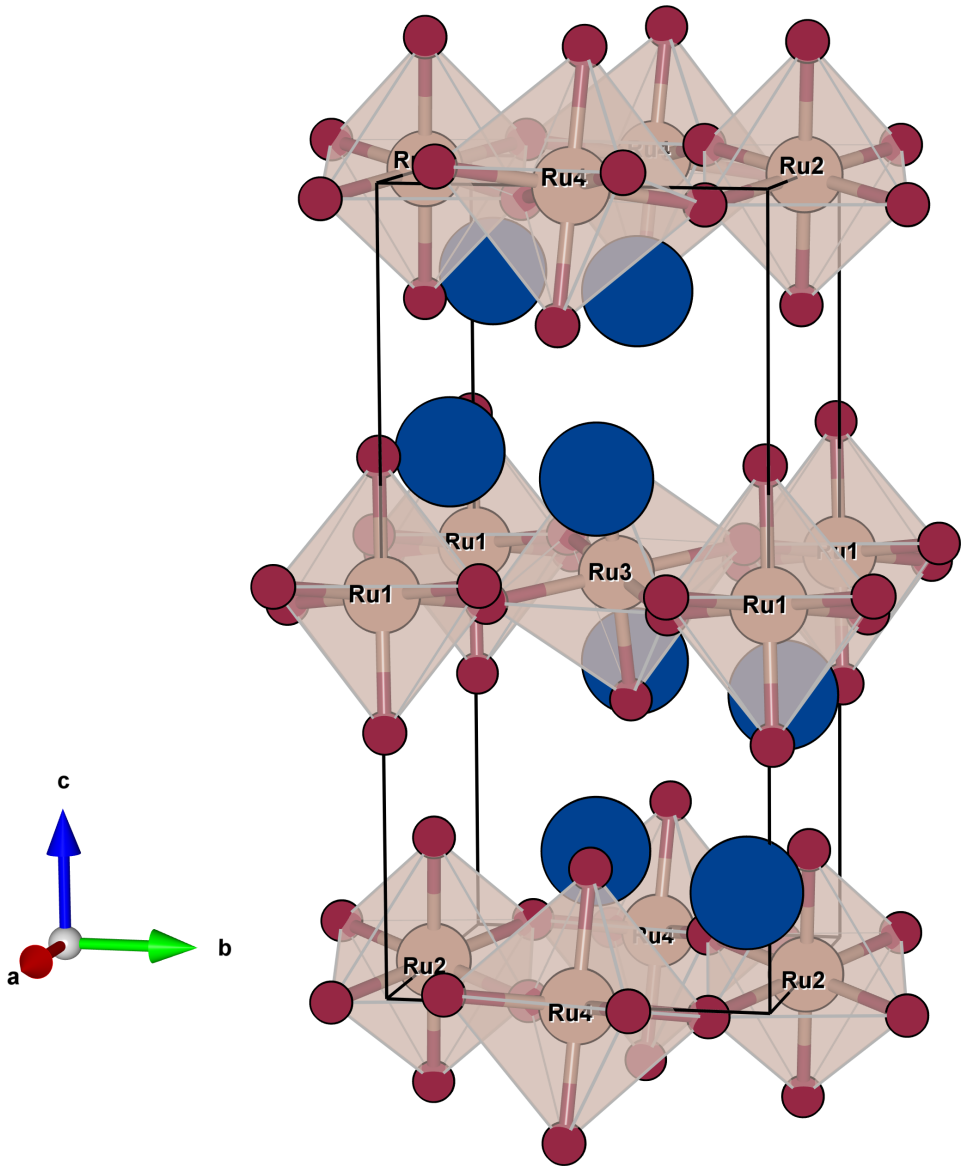

Figure 2.14: Sketch of three layers of square-lattice Ca_2RuO_4 at temperature $T = 130\,\mathrm{K}$ in the equilibrium S-phase [5, 63]. Each Ru-atom (brown ball) is surrounded by six oxygen atoms (small red balls). The RuO_6 octahedra are a bit canted towards each other. The unit cell consists of four Ru-atoms (Ru1 to Ru4) and is periodically repeated. The Ca-atoms are given as blue balls.

Ca_2RuO_4 is a quasi two-dimensional material with Ru^{4+} ions surrounded by oxygens in an octahedral configuration, see Fig. 2.14. Within each layer, the Ru-atoms build a square lattice and the RuO_6 octahedra are slightly canted towards each other at low temperatures. For high temperatures, Ca_2RuO_4 is metallic. The metal-to-insulator transition takes place at $T_{\mathrm{MI}} = 357\,\mathrm{K}$ and is accompanied by a flattening of the RuO_6 octahedra [2, 7, 17] along the c-axis. This flattening continues upon further cooling until it saturates near the onset of magnetic order at the Neel temperature $T_{\mathrm{N}} \approx 110\,\mathrm{K}$. The magnetic structure in the low-temperature phase is AFM with moments aligned parallel to the layer [7] and canted by about 6° against the b-axis [41].

The structural phase transition leads to a rather strong TCF which lowers the energy of the xy-orbital. Experiments [15] as well as numerical approaches [13, 14, 21, 44, 78] confirm its nearly full occupation. Based on these observations, some state that a more conventional spin $S = 1$ order resulting from the two half-filled xz- and yz-orbitals is responsible for the magnetism. In this approach, SOC would then be only a correction and not a main driver of the magnetism [41]. This explanation is supported by *ab initio* calculations [78] that in turn agree with angle-resolved photoemission spectroscopy [69]. ED calculations [10] showed that even in the absence of SOC the compressive octahedra distortions stabilize an AFM state with C- or G-type structure and different orbital configurations, depending on the degree of flattening.

Experiments in the insulating state revealed a global maximum of the spin-wave dispersion found at the center of the first Brillouin zone which is in sharp contrast to a Heisenberg antiferromagnet [28]. It is still unclear, how the excitonic magnetism and the spin-1 magnetism are compatible and if *ab initio* calculations are able to reproduce the excitonic magnetism.

2.3 The Variational Cluster Approximation

The CPT [23, 64] and its extension, the VCA [12, 54], are two methods to solve problems of many-body lattice systems. Both methods require the solution of a small cluster system which can be achieved by ED based on the Lanczos method [43]. Within VCA, all one-particle parameters applied to the reference cluster system can in principle be used for a variational approach. VCA has been highly successful in describing angle-resolved photoemission spectroscopy for strong SOC Sr_2IrO_4 [72].

Other numerical approaches like density matrix renormalization group studies on three-orbital Hubbard models [29] and dynamical mean field theory calculations [5] were not able to gather the two-dimensional system for zero temperature. In the first case, only one-dimensional systems are addressed while in the second, the system was studied for higher temperature. In [62], a simplified Hamiltonian was used to mitigate the sign problem. Using VCA, it is possible to investigate two-dimensional lattices and examine the system for zero temperature and arbitrary hopping parameters. VCA gives exact results on the small cluster and allows us to study symmetry-breaking fields on the lat-

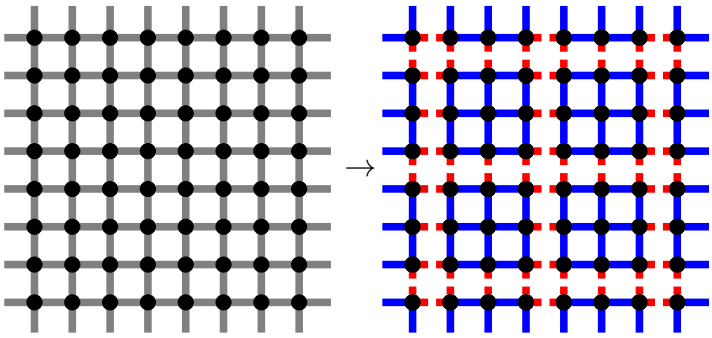

Figure 2.15: Tiling a square lattice (left site) into finite clusters e. g. of size nine. The interactions on the cluster $\boldsymbol{\tau}'$ are illustrated by blue bonds while the interactions between the clusters $\boldsymbol{V}$ are shown in red.

tice including long-range magnetic order. Further, we are able to switch the magnetic effects on and off by adding or removing the fictitious fields.

In Sec. 2.3.1, the relevant features of CPT and VCA are presented. The application of VCA to our model system and the variational principle regarding the symmetry-breaking fields and the chemical potential is given in Sec. 2.3.2.

2.3.1 General Introduction

As VCA is an extension to CPT, we provide a short summary of their conception and main ideas. A more detailed introduction to quantum cluster methods is given in [65].

Cluster Perturbation Theory

The basic idea of CPT is composed out of three steps [64]: First, the infinite lattice is divided into small identical clusters, see Fig. 2.15. Second, the one-particle Green's function within the cluster system is calculated with ED. Third, strong-coupling perturbation theory for the intersite interaction yields a connection between the cluster and the lattice system to reach the thermodynamic limit.

When tiling the lattice, the Hamiltonian H has to be separated into interactions on the cluster $\boldsymbol{\tau}'$ and between the clusters $\boldsymbol{V}$, see Fig. 2.15. The strong-coupling perturbation theory [66] then connects the Green's function of the lattice $\boldsymbol{G}$ and of the cluster $\boldsymbol{G}'$ in lowest order by

$$\boldsymbol{G}^{-1}(\omega) = \boldsymbol{G}'^{-1}(\omega) - \boldsymbol{V} \tag{2.29}$$

where ω is the energy. In the following, all parameters of the cluster are marked with a prime. The form and the function of the $\boldsymbol{V}$-matrix can be motivated using the Dyson equation. The latter results from diagrammatic perturbation theory [50] and expresses

the Green's function $\boldsymbol{G}$ in terms of its non-interacting part $\boldsymbol{G}_0$ and its self-energy $\boldsymbol{\Sigma}$ by

$$\boldsymbol{G}^{-1} = \boldsymbol{G}_0^{-1} - \boldsymbol{\Sigma}, \tag{2.30}$$
$$\boldsymbol{G}'^{-1} = \boldsymbol{G}_0'^{-1} - \boldsymbol{\Sigma}'. \tag{2.31}$$

for each system, respectively. As the self-energy, opposed to the Green's functions, is a much more local object and becomes purely local in the limit of lattices with infinite spatial dimensions, one can use the so-called Hubbard-I approximation $\boldsymbol{\Sigma} \approx \boldsymbol{\Sigma}'$ [25]. Then, Eq. (2.30) and Eq. (2.31) allow to express the Green's function $\boldsymbol{G}$ of the lattice in terms of

$$\boldsymbol{G}^{-1}(\omega) = \boldsymbol{G}'^{-1} - (\boldsymbol{G}_0'^{-1} - \boldsymbol{G}_0^{-1}) \equiv \boldsymbol{G}'^{-1}(\omega) - \boldsymbol{V}. \tag{2.32}$$

Like this, $\boldsymbol{V}$ is composed out of the non-interacting Green's functions. Furthermore, the interaction on the cluster $\boldsymbol{\tau}'$ is limited to one-particle operators only as they are incorporated in $\boldsymbol{G}_0'$.

As the tiling of the lattice into clusters gives a periodic structure, the periodization of the Green's function to the full lattice is possible. Further, it must be noted that CPT is exact in the strong coupling limit $t/U \to 0$ and for $U \to 0$ as the self-energy vanishes. However, CPT cannot be used for symmetry-broken states as it is still based on finite systems.

Variational Cluster Approximation

The VCA is based on CPT and extends the latter by including self-energy functional theory [55–57]. The general idea of VCA is to treat the cluster system as a reference system for a variational approach since the cluster system and the lattice system are allowed to differ by one-particle parameters $\boldsymbol{\tau}'$.

Luttinger and Ward [45] showed that the grand potential Ω can be written as a functional of the Green's function

$$\Omega[\boldsymbol{G}] = \Phi_{\mathrm{LW}}[\boldsymbol{G}] - \mathrm{Tr}\ln(-\boldsymbol{G}_0^{-1} + \boldsymbol{\Sigma}) - \mathrm{Tr}(\boldsymbol{\Sigma}\boldsymbol{G}) \tag{2.33}$$

where Φ_{LW} is the Luttinger-Ward functional and Tr denotes the trace. Using the properties of Φ_{LW} it can be shown that it is stationary if the Green's function fulfills the Dyson equation

$$\boldsymbol{G}^{-1} = \boldsymbol{G}_0^{-1} - \boldsymbol{\Sigma} \iff \frac{\delta\Omega[\boldsymbol{G}]}{\delta\boldsymbol{G}} = 0. \tag{2.34}$$

As Φ_{LW} is not known, a Legendre transformation of Eq. (2.33) yields it in terms of the self-energy $\boldsymbol{\Sigma}$ to

$$\Omega[\boldsymbol{\Sigma}] = F[\boldsymbol{\Sigma}] - \mathrm{Tr}\ln(-\boldsymbol{G}_0^{-1} + \boldsymbol{\Sigma}) \tag{2.35}$$

leading to the new stationary condition

$$\boldsymbol{G}^{-1} = \boldsymbol{G}_0^{-1} - \boldsymbol{\Sigma} \iff \frac{\delta\Omega[\boldsymbol{\Sigma}]}{\delta\boldsymbol{\Sigma}} = 0. \tag{2.36}$$

Still, the Legendre transformed Luttinger-Ward functional $F[\boldsymbol{\Sigma}]$ is unknown. However, F is the same for every system with the same interaction part which applies to the cluster and the lattice system. By replacing F, Eq. (2.35) and its counterpart for the cluster system can therefore be combined to

$$\Omega[\boldsymbol{\Sigma}'] = \Omega' - \operatorname{Tr}\ln(-\boldsymbol{G}_0^{-1} + \boldsymbol{\Sigma}') + \operatorname{Tr}\ln(-\boldsymbol{G}_0'^{-1} + \boldsymbol{\Sigma}'). \tag{2.37}$$

To guess the self-energy $\boldsymbol{\Sigma}'$, any one-particle operator can be added to the cluster system. A stationary point in the grand potential Ω tells us if the choice could represent the physical system. Introducing the one-particle operators $\boldsymbol{\tau}'$ on the cluster as variational parameters, the stationary condition Eq. (2.36) turns into

$$\left.\frac{\partial\Omega[\boldsymbol{\Sigma}'_{\boldsymbol{\tau}'}]}{\partial\boldsymbol{\tau}'}\right|_{\boldsymbol{\tau}'=\boldsymbol{\tau}'_{\mathrm{opt}}} = 0, \tag{2.38}$$

where the optimal self-energy $\boldsymbol{\Sigma}'_{\boldsymbol{\tau}'_{\mathrm{opt}}}$ is given by the solution $\boldsymbol{\tau}'_{\mathrm{opt}}$.

2.3.2 Application of VCA to symmetry-broken Systems

Since the ground state of a finite cluster cannot spontaneously break a symmetry of the Hamiltonian, it is not possible to investigate symmetry-broken systems within CPT. However, in the VCA the freedom of adding one-particle parameters to the reference cluster combined with the stationary condition allows us to study symmetry-breaking fields such as AFM orderings. These so called Weiss fields are no physical fields but fictitious ones that only exist on the reference cluster.

Weiss Fields

The most general form of such a Weiss field is given by

$$H_{\mathrm{W}} = h' \sum_i \Lambda_i \mathrm{e}^{\mathrm{i}\boldsymbol{Q}\boldsymbol{R}_i} \tag{2.39}$$

where Λ_i can be any one-particle operator on site i with site vector $\boldsymbol{R}_i$ and vector $\boldsymbol{Q}$ which fixes the ordering pattern. The choice of Λ_i determines the manifold $\boldsymbol{\Sigma}_{h'}$ and the strength of the field h' takes the role of $\boldsymbol{\tau}'$ in Eq. (2.38) which directly leads to the optimal field strength h'_{opt}.

For example, the magnetic Weiss field which applies AFM ordering with spins pointing in z-direction is given by

$$H = h' \sum_{i,\alpha} (n_{i\alpha\uparrow} - n_{i\alpha\downarrow}) \mathrm{e}^{\mathrm{i}(\pi,\pi)^{\mathrm{T}}\boldsymbol{R}_i}, \tag{2.40}$$

where the sum goes over all orbitals $\alpha = xy, yz, xz$ and sites i. The AFM ordering of the spins in z-direction is forced by the number operators $n_{i\alpha\sigma=\uparrow,\downarrow}$ as $n_{i\alpha\uparrow} - n_{i\alpha\downarrow} \propto S_z$ and

the staggering $e^{i(\pi,\pi)^T \boldsymbol{R}_i}$ which reverses the sign giving a checkerboard pattern. Stripy patterns can be achieved by setting $\boldsymbol{Q} = (\pi, 0)^T$ or $\boldsymbol{Q} = (0, \pi)^T$.

Furthermore, Weiss fields with several independent one-particle operators are useful to describe more complex orderings. For example, one could think of a stripy spin order and a thereto orthogonal stripy orbital order each having a different field strength h'_k. For such a Weiss field

$$H_W = \sum_k \left(h'_k \sum_i \Lambda_{ik} e^{i\boldsymbol{Q}_k \boldsymbol{R}_i} \right) \tag{2.41}$$

with k variational parameters, all strengths h'_k have to be optimized by Eq. (2.38) which results in a multi-dimensional optimization problem.

The main drawback of VCA lies in the guessing of the self-energy and the small cluster. The stationary condition only tells us that we found a possible solution of the infinite lattice system's Dyson equation. Therefore, any Weiss field that could yield a reasonable physical field must be applied to the system and the results have to be compared to each other. As the variational principle Eq. (2.38) is a global request, the Weiss field with the lowest value of $\Omega(h'_{\text{opt}})$ wins given that $\Omega(h')$ shows a minimum.

Optimization of the chemical Potential

For the investigation of d^4 systems, the particle number per site has to be fixed to four throughout the calculations. As we operate in the hole picture, the particle number per site is $N = 2$. This is done by retaining a stable and constant chemical potential μ expressed by

$$H_\mu = -\mu \sum_{i,\alpha,\sigma} n_{i\alpha\sigma} \tag{2.42}$$

with $n_{i\alpha\sigma}$ being the number operator for a hole located at site i in the orbital α with spin σ. Since the band structure is influenced by SOC and on-site interactions, we adjust the chemical potential by means of VCA. Using a Legendre transformation [4], the stationary condition Eq. (2.38) for fixed particle number turns into

$$\frac{\partial F}{\partial \boldsymbol{\tau}'} = 0 \iff \frac{\partial \Omega}{\partial \boldsymbol{\tau}'} = 0 \tag{2.43}$$

with the free energy F given by $F = \Omega + \mu N$. At the same time, this gives the additional condition

$$\frac{\partial F}{\partial \mu} = 0 \iff \left\langle \sum_{i,\alpha,\sigma} n_{i\alpha\sigma} \right\rangle = N. \tag{2.44}$$

Figure 2.16 shows an example for this optimization. The hole density of the lattice in Fig. 2.16 (a) and the hole density of the cluster in Fig. 2.16 (b) both show a plateau close to the intended density of $N = 2$ indicating that the magnitude of μ is correctly chosen. The optimal value of $\mu = 8.05t$ in terms of Eq. (2.44) is given by the minimum in the

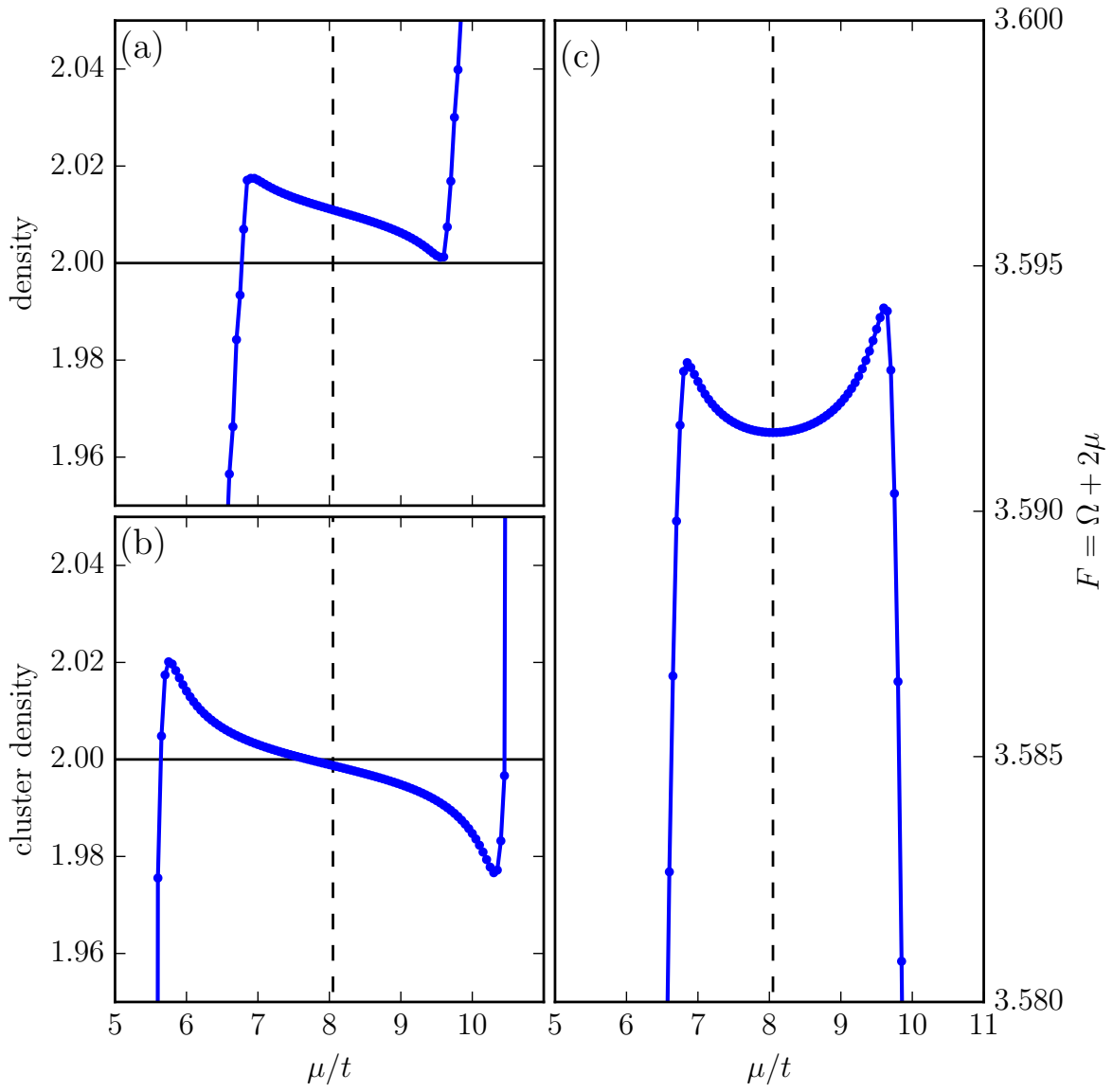

Figure 2.16: Optimization of the chemical potential μ according to Eq. (2.44). (a) The hole density of the lattice shows a plateau close to the intended density per site $N = 2$. (b) The cluster hole density per site also varies around $N = 2$. (c) The free energy $F = \Omega + 2\mu$ is extremal for $\mu = 8.05t$ marked by the dashed line. The parameter t defines the energy scale.

free energy F, see Fig. 2.16 (c). However, the hole density $N \approx 2.011$ at $\mu = 8.05t$ is not close enough to the intended density of $N = 2$.

Therefore, taking advantage of the variational principle, we allow the chemical potential on the reference system to slightly deviate by μ' taking into account deviations potentially arising from the approximate nature of the approach. It is optimized using Eq. (2.38)

$$\frac{\partial \Omega}{\partial \mu'} = 0. \tag{2.45}$$

It guarantees a better hole density both for the lattice and the cluster as shown in Fig. 2.17. Even if the density of the lattice shows a steep increase for increasing μ', see Fig. 2.17 (a), the optimal value of $\mu' = -0.08t$ given by the maximum in Ω in Fig. 2.17 (c) fixes the density to $N \approx 2$. The cluster density in Fig. 2.17 (b) stays nearly constant around $N = 2$ for all values of μ'.

The optimization of μ and μ' adds two additional variational parameters to the set of $\boldsymbol{\tau}' = \{h'_k, \mu, \mu'\}$ turning the optimization problem into a multi-dimensional one. Fortunately, throughout our investigations we find that the chemical potentials μ and μ' are not very susceptible to the investigated strength h'_k. For this reason, the optimization can be decomposed into three steps. First, we adjust the chemical potential μ by Eq. (2.44) for $h'_k = 0$ and $\mu' = 0$. Second, the cluster chemical potential is optimized by Eq. (2.45) for fixed μ and $h'_k = 0$. Third, the chemical potentials are kept fixed for a optimization regarding h'_k.

Although there is no restriction given by VCA concerning the type of extremum, we found that in almost all optimizations the optimal μ is given by a minimum and μ' by a maximum. Regarding the Weiss fields h'_k, the optimization in terms of minima is predominant.

Observables

Several observables are accessible using CPT and VCA. Regarding the CPT one-particle Green's function, it allows us to calculate the spectral density $A(\boldsymbol{k}, \omega)$ by

$$A(\boldsymbol{k}, \omega) = -2 \lim_{\eta \to \infty} \mathrm{Im}\{\boldsymbol{G}(\boldsymbol{k}, \omega + \mathrm{i}\eta)\}. \tag{2.46}$$

It gives the probability distribution for the energy ω of an electron of wave vector $\boldsymbol{k}$ that is added to or removed from the system. The electron-removal part of the spectral density can be measured by angle-resolved photoemission spectroscopy.

Further, the density of states yields

$$N(\omega) = \frac{1}{N_{\boldsymbol{k}}} \sum_{\boldsymbol{k}} A(\boldsymbol{k}, \omega) \tag{2.47}$$

with $N_{\boldsymbol{k}}$ being the number of $\boldsymbol{k}$-points.

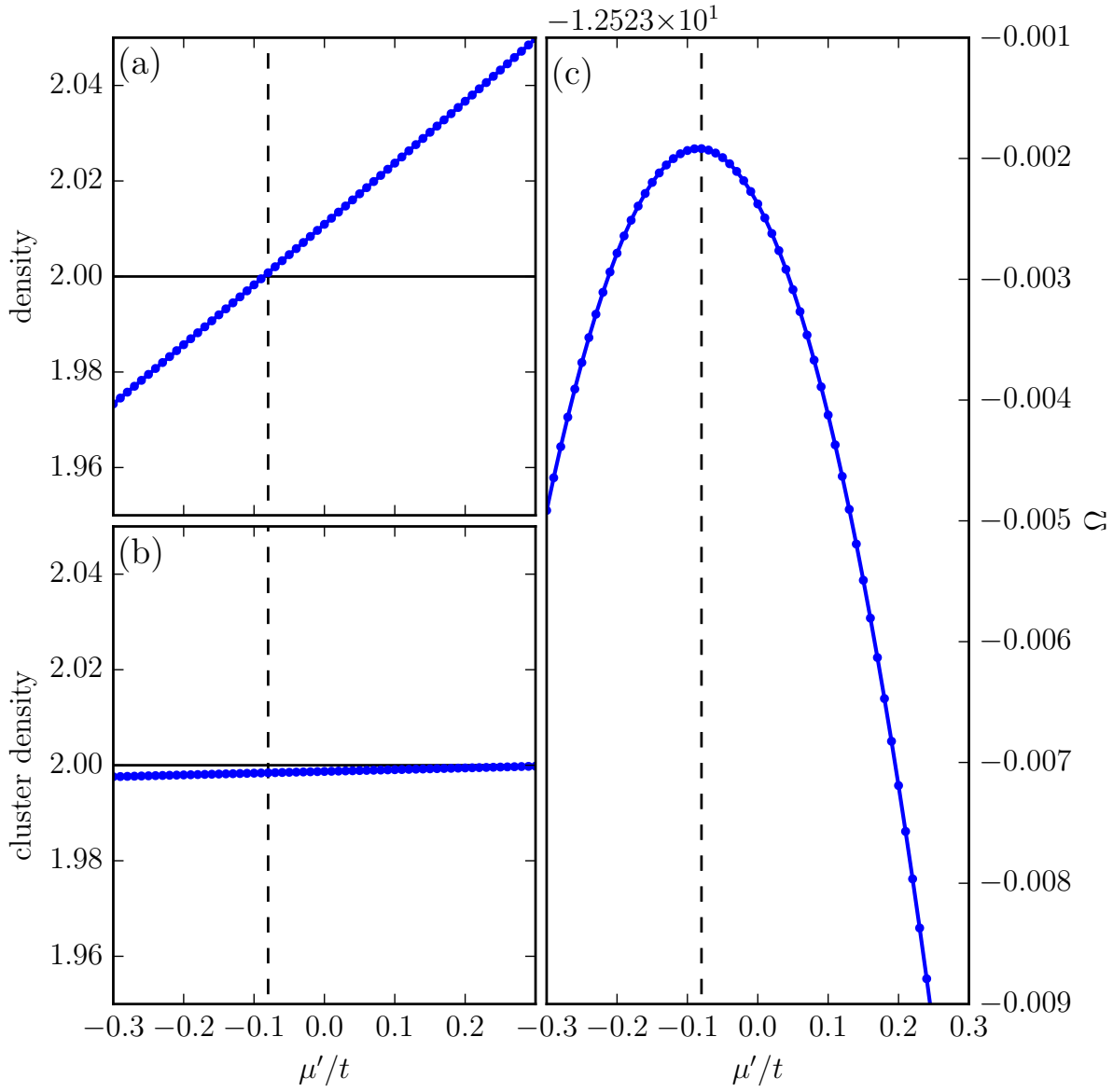

Figure 2.17: Optimization of the cluster chemical potential μ' for fixed $\mu = 8.05t$ which was found in Fig. 2.16. (a) The density of the lattice shows no plateau as before but a steep increase for increasing μ'. (b) Nevertheless, the cluster density stays nearly constant. (c) The optimal value of μ' is given by Eq. (2.45) which is a maximum in Ω at $\mu' = -0.08t$. For this value (marked by the dashed line), both densities are close to $N = 2$.

The expectation value of an one-particle operator O at temperature $T = 0$ is calculated by the contour

$$\langle O \rangle = \frac{1}{2\pi \mathrm{i}} \int_C \mathrm{d}(\mathrm{i}\omega) \mathrm{Tr}(O\boldsymbol{G}(\mathrm{i}\omega)) \tag{2.48}$$

over the path C where $\boldsymbol{G}$ is the VCA Green's function. This is used for the calculation of the occupation numbers of the orbitals, the Kramers states, Eq. (2.25), and the full atomic model, Eq. (2.28).

For a two-particle operator or its corresponding ground state $|\psi\rangle$, the expectation value is given by the ED Lanczos ground state $|\phi\rangle$ of the cluster

$$\langle \psi \rangle = |\langle \phi | \psi \rangle|^2 = \langle \phi | \psi \rangle \langle \psi | \phi \rangle . \tag{2.49}$$

This is done for the expectation values of the J_{LS} states, Eq. (2.17), and the J_{jj} states, Eq. (2.24).

3 Excitonic Magnetism

Strongly correlated electron systems offer a huge range of quantum phenomena including some that were already known for completely different states of matter. One of it is the Bose-Einstein condensate that was originally observed in cold bosonic gases. However, magnetic insulators like $TlCuCl_3$ were found to yield Bose-Einstein condensation of triplet magnon excitations [20, 40, 46, 59, 61] separating a dimer-based quantum disordered phase from a phase of long-ranged magnetic order.

Recently, Khaliullin [31] proposed a similar excitonic magnetism in multi-orbital magnetic insulators with d^4 configuration. In the atomic limit, strong Coulomb interaction and Hund's coupling ensure that exactly one orbital per site is doubly occupied. The resulting two half-filled orbitals then form an effective angular momentum $L = 1$ and spin $S = 1$. SOC couples L and S to a non-magnetic ionic ground state $J_{LS} = 0$ and a magnetic triplet state $J_{LS} = 1$ that are separated by SOC, see Sec. 2.1.4. However, as superexchange is on a comparable energy scale, excitonic magnetism can emerge when the on-site wave function becomes a superposition of the singlet $J_{LS} = 0$ and the triplet $J_{LS} = 1$. It thus acquires a magnetic moment that can order. Experiments on the candidate compound Ca_2RuO_4 [22, 67, 77] revealed a global maximum of the spin-wave dispersion found at the center of the first Brillouin zone which is in sharp contrast to a Heisenberg antiferromagnet [28] indicating the realization of such excitonic magnetism.

Apart from density matrix renormalization group studies on one-dimensional three-orbital Hubbard models [29] and dynamical mean field theory calculations for higher temperatures [5] and for a simplified model [62] there are no further numerical approaches regarding this excitonic magnetism. Using VCA, cf. Sec. 2.3, we are not only able to investigate the emergence of such magnetism but also observe how large the admixture of the magnetic triplet to the non-magnetic singlet is. Further, we have access to the type of the spin and orbital orderings that occur in the magnetic phase.

To observe this mechanism, we start with a simple model containing only nearest neighbor hopping, Hund's coupling and Coulomb interaction as well as SOC on a two-dimensional four-site cluster in Sec. 3.1.1. Crystal field splittings apart from the cubic symmetry are not taken into account. On the one hand, this model serves to understand the mechanism of excitonic AFM symmetry-breaking within VCA and the observables derived from it such as the expectation values, cf. Eq. (2.49) and Eq. (2.48), the grand potential Ω and the one-particle spectral densities. On the other hand, we investigate the impact of SOC by tuning it from rather small $\lambda \approx 0.1t$ to larger $\lambda \approx 1.6t$ while the other parameters stay fixed. It shows that SOC suppresses orbital order and drives the formation of an AFM regime for intermediate strength. Finally, there is a critical λ

above which the AFM order disappears and the system becomes non-magnetic.

In Sec. 3.1.2, we use the gathered information for a detailed parameter study on the hopping amplitude, the on-site interactions and SOC separately to derive a λ-(U, J_H) phase diagram.

Although the non-magnetic regime already appears in the LS-regime, we tune λ even stronger and show the transition to the jj-limit with $\lambda > J_\mathrm{H}$ in Sec. 3.2. This scenario is likely to be realized in non-magnetic double-perovskite iridates [18, 52].

As discussed in Sec. 2.1.2 the orbitals xy, xz and yz do not participate equally in the nearest neighbor hopping process. We investigate the impact of the hopping anisotropy on the excitonic regime by reducing it towards a more isotropic model in Sec. 3.3.

3.1 Magnetism and Trends in the LS-Regime

Before gathering all peculiarities of a real physical system, we first focus on a model with easier hopping structure. We restrict ourselves to a simple hopping that includes only the strongest nearest neighbor hopping part t_{xy}, t_{yz}, t_{xz}, see Eq. (2.9). Further, we fix the hopping between all orbitals to the same value $t = t_{xy} = t_{yz} = t_{xz}$. The interaction is given by the Kanamori parameters, Eq. (2.11), and SOC, Eq. (2.6), is taken into account. We neglect any further hoppings or crystal field contributions.

3.1.1 A simple Model

As already discussed in Sec. 2.3, the optimal magnetic field strength h' of a Weiss field applied to the reference system can be found by evaluating Eq. (2.38) meaning there exists an extremum in the grand potential $\Omega(h')$. We start with a model having $U = 12.5t$, $J_\mathrm{H} = 2.5t$ and $0.25t \lesssim \lambda \lesssim 1.25t$ with $t = t_{xy} = t_{yz} = t_{xz}$ on a two-dimensional four-site cluster. In this limit, the SOC is small enough to guarantee the LS-coupling scheme. Within our investigations several magnetic and orbital regimes are found. Before deeply examining them we first give an example for the mechanism of VCA and the applied Weiss fields.

We investigate three ordering patterns for four different values of SOC λ. As explained in Sec. 2.3, the chemical potentials μ and μ' are optimized in the absence of Weiss fields and are kept fixed for further optimizations regarding the Weiss fields. Figure 3.1 presents the grand potential Ω in dependence on the Weiss field strength. As some fields combine magnetic and orbital orderings, we need two different variational parameters h' and o', see Eq. (2.41). The corresponding operators Λ and vectors $\boldsymbol{Q}$ used in Eq. (2.41) can be found in Tab. 3.1. For simplicity, we refer to the stripy and checkerboard (G-type) antiferromagnetically ordered regimes as stripy and AFM regimes, respectively. In Fig. 3.1 each value of λ is coded by a color and the patterns can be distinguished by symbol. Arrows denote global minima for each value of λ. We first focus on the red curves which represent the smallest value of $\lambda = 0.25t$, where we show Ω for stripy S_x

	Λ_1	$\boldsymbol{Q}_1$	Λ_2	$\boldsymbol{Q}_2$	Λ_3	$\boldsymbol{Q}_3$
stripy S_z	S_z	$(\pi, 0)$				
stripy S_z, stripy orb	S_z	$(\pi, 0)$	$n_{xy} - n_{xz}$	$(0, \pi)$	$-n_{yz}$	$(0, 0)$
stripy S_x	S_x	$(\pi, 0)$				
stripy S_x, stripy orb	S_x	$(\pi, 0)$	$n_{xy} - n_{xz}$	$(0, \pi)$	$-n_{yz}$	$(0, 0)$
AFM S_z	S_z	(π, π)				
AFM S_z, FO xy	S_z	(π, π)	n_{xy}	$(0, 0)$		
AFM S_z, TO	S_z	(π, π)	TO [24]	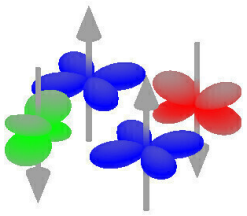		
AFM $2S_z + L_z$	$2S_z + L_z$	(π, π)				
AFM M_z	$M_z = 2S_z - L_z$	(π, π)				
AFM J_z	J_z	(π, π)				
AFM S_x	S_x	(π, π)				
AFM J_x	J_x	(π, π)				

Table 3.1: Overview of the Weiss field patterns and their composition out of orbital and magnetic components. The Weiss field Hamiltonian is given by Eq. (2.41) with the operators Λ_k and vectors $\boldsymbol{Q}_k$. The cartoon picture shows the orbital ordering TO suggested in [24]. For simplicity, we refer to the stripy and checkerboard (G-type) antiferromagnetically ordered regimes as stripy and AFM regimes, respectively.

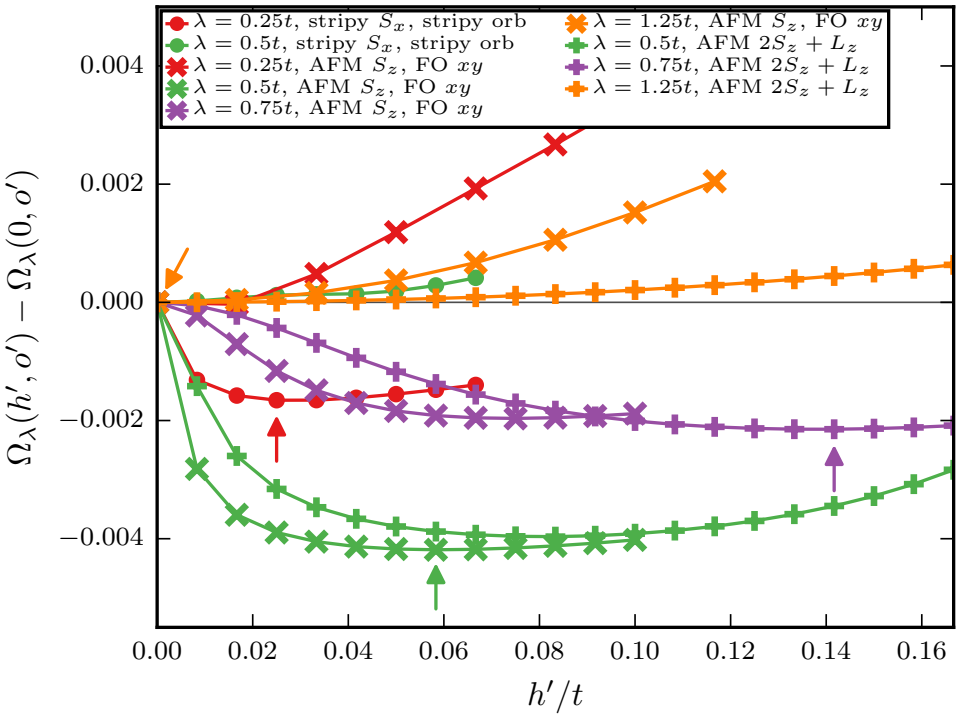

Figure 3.1: Comparison of three ordering pattern's grand potential $\Omega(h', o')$ over the magnetic Weiss field strength h'. As it is a two-dimensional variational space we project Ω on the Ω-h' plane for several values of SOC λ with fixed $U = 12.5t$, $J_\mathrm{H} = 2.5t$, $t = t_{xy} = t_{yz} = t_{xz} = 0.12\,\mathrm{eV}$ on a two-dimensional four-site cluster. The operators and vectors of the Weiss fields are given in Tab. 3.1. The small arrows denote the global minima for each value of λ.

with stripy orbital order and AFM S_z with ferro-orbital (FO) xy order. The latter shows a minimum at $h' = 0$, so its Weiss field is not favorable. However, the stripy S_x order has $h'_{\text{opt}} \neq 0$ indicating that this order is favored by the system.

Moving on to $\lambda = 0.5t$, data for three orderings are shown of which two have a non-zero h'_{opt}. The previously favored stripy regime is no longer a favored order. Now, the AFM S_z and the AFM $2S_z + L_z$ order compete. Since $\Omega(h')$ of AFM S_z is lower than $\Omega(h')$ of AFM $2S_z + L_z$, the AFM S_z order wins. Increasing λ even further to $0.75t$ the situation changes and AFM $2S_z + L_z$ wins. Finally, for $\lambda = 1.25t$ all minima with $h' \neq 0$ are gone and the system favors none of the suggested orderings. In this case, we speak of a non-magnetic or paramagnetic (PM) regime.

While $J_{\text{H}} > \lambda$ suggests that LS-coupling should be appropriate, we can test this assumption by calculating the overlap $\langle J_{LS} \rangle$, see Eq. (2.49). Figure 3.2 (a) presents several expectation values in the evolution of an AFM $2S_z + L_z$ Weiss field with strength h'. We fix $U = 12.5t$, $J_{\text{H}} = 2.5t$, $\lambda = t$ and $t = t_{xy} = t_{yz} = t_{xz} = 0.12\,\text{eV}$. The vertical line indicates the optimal value of $h'_{\text{opt}} = 0.1167t$ found by VCA as the minimum of $\Omega(h')$ in Fig. 3.2 (b). By tuning the Weiss field from the unordered state $h' = 0$ to the ordered state with optimal value h'_{opt}, we are able to observe a smooth and continuous evolution of the state population. There is no magnetic ordering for $h' = 0$ due to the small cluster size which allows us to compare the unordered state to the magnetically ordered state with h'_{opt}. The development of the expectation values is even accessible for $h' > h'_{\text{opt}}$.

Starting with $h' = 0$, the LS-picture is a good description as the $|J_{LS} = 0\rangle$ state is nearly fully occupied and $\langle J_{LS} = 1, 2\rangle \approx 0$. Regarding the ground state of the jj-limit, $|J_{jj} = 0\rangle$, it is not as useful as $|J_{LS} = 0\rangle$ because $\langle J_{jj}\rangle < 0.8$. Note that the overlap of the two states $\langle J_{LS} = 0 | J_{jj} = 0\rangle \approx 0.816$ explaining the value. However, the higher J_{jj} states $|J_{jj} = 1, 2\rangle$ behave like the $|J_{LS} = 1, 2\rangle$ states. Due to the cubic crystal symmetry, the cubic harmonic orbitals should be equally populated for $h' = 0$. However, the anisotropic hopping slightly lifts this degeneracy. The xy-orbital is allowed to hop in x- and y-direction whereas yz and xz are bound to one direction, cf. Sec. 2.1.2.

Starting to apply an AFM $2S_z + L_z$ Weiss field partly affects the populations. First, it further splits the orbitals in favor of the xy-orbital. $\langle J_{LS} = 0\rangle$ gets already reduced for small h' but is still a good description for the ground state. The way the $|J_{LS} = 0\rangle$ state and the $|J_{jj} = 0\rangle$ state loose population, the $|J_{LS} = 1\rangle$ state and the $|J_{jj} = 1\rangle$ state gain it showing that the magnetism is enabled by triplet admixture to the non-magnetic singlet. The $|J_{LS} = 2\rangle$ state and the $|J_{jj} = 2\rangle$ state remain unpopulated and do not contribute to the magnetism. Since always $\langle J_{jj} = 0\rangle < 0.8$ the J_{jj} states are not a suitable description for this range of λ / J_{H}.

As already mentioned, several orderings compete with each other and can be compared by their Ω-values. Figure 3.3 shows the value of the grand potential $\Omega_{\text{opt}} = \Omega(h'_{\text{opt}}, o'_{\text{opt}})$ with non-zero h'_{opt} for all tested orderings. Ω_{opt} is given relative to $\Omega_{\text{PM}} = \Omega(0)$. The operators and vectors of each order are given in Tab. 3.1. The colored background denotes the order that is favored by the system meaning that it has the lowest value

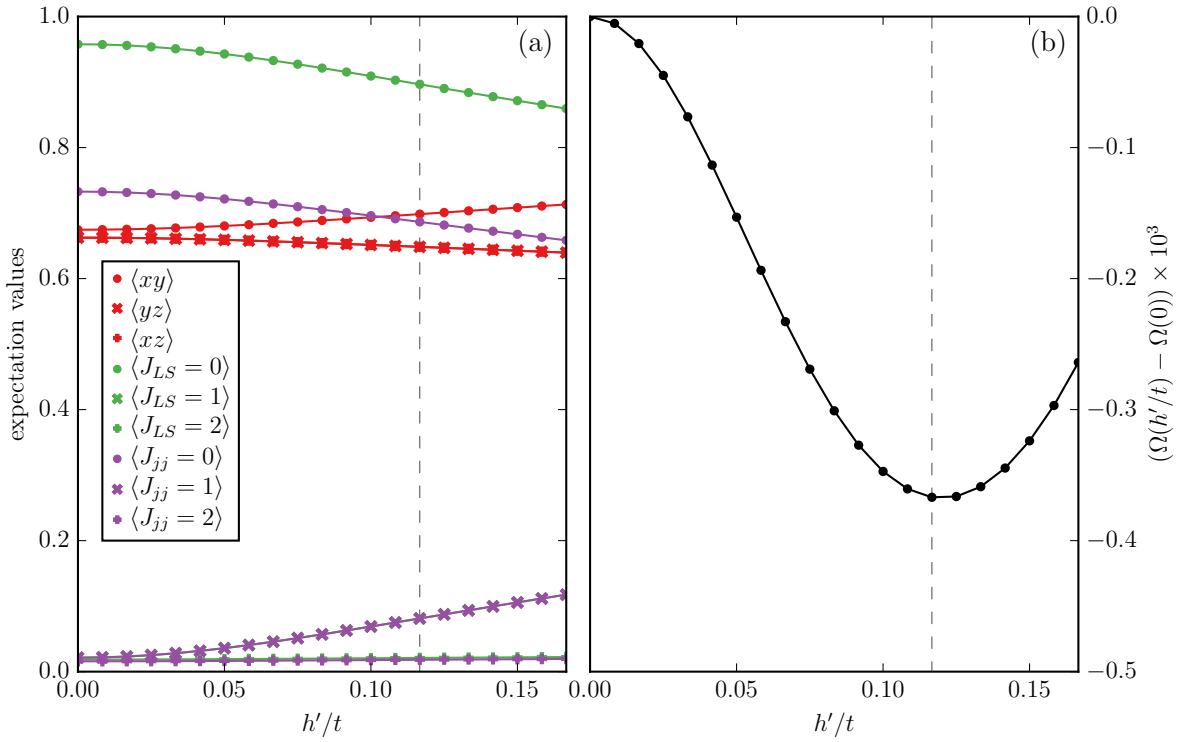

Figure 3.2: (a) Evolution of the expectation values of different states under the increasing impact of an AFM $2S_z+L_z$ Weiss field strength h'. The vertical line indicates the optimal value of $h' = 0.1167t$ given in (b) by the minimum of $\Omega(h'/t)$. We fix $U = 12.5t$, $J_{\mathrm{H}} = 2.5t$, $t = t_{xy} = t_{yz} = t_{xz} = 0.12\,\mathrm{eV}$, $\lambda = t$. Regarding the population of the t_{2g} orbitals, increasing h' splits the orbitals in favor of the xy-orbital. The system is clearly in the LS-regime as $\langle J_{LS} = 0 \rangle \approx 1$ for $h' = 0$ whereas the jj-limit ground state $\langle J_{jj} = 0 \rangle < 0.8$. The triplets $|J_{LS}, J_{jj} = 1\rangle$ and quintets $|J_{LS}, J_{jj} = 2\rangle$ are nearly zero for $h' = 0$. Turning the Weiss field on, the population of the $|J_{LS}, J_{jj} = 1\rangle$ states increases in the way the population of the $|J_{LS}, J_{jj} = 0\rangle$ states diminishes. This shows that the magnetism arises due to triplet admixture to the non-magnetic singlet.

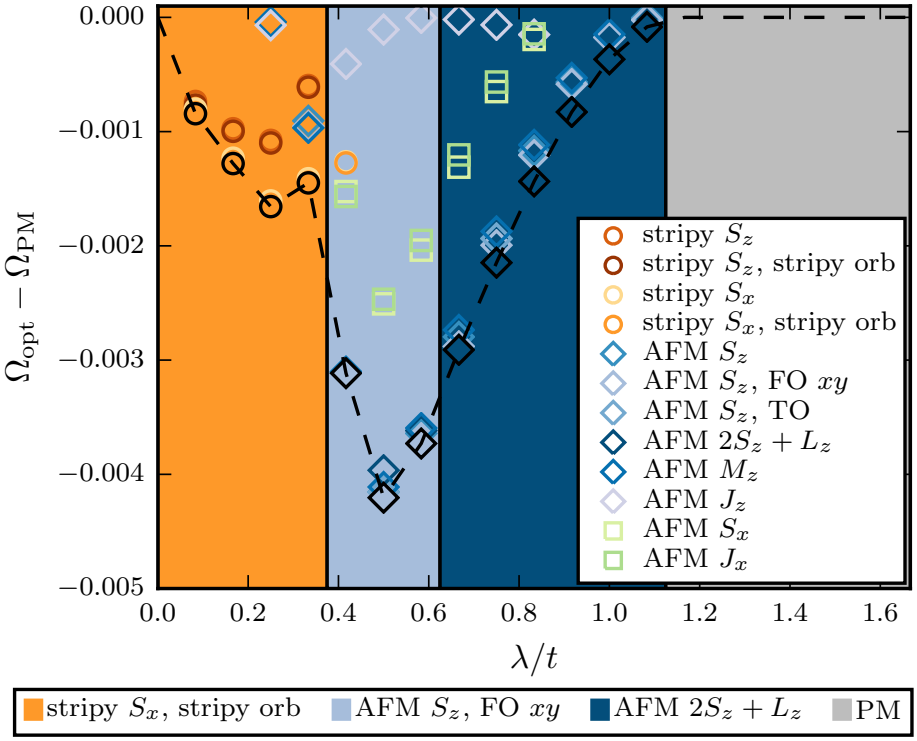

Figure 3.3: Comparison of several ordering pattern's grand potential $\Omega_{\mathrm{opt}}(h'_{\mathrm{opt}}, o'_{\mathrm{opt}})$ relative to $\Omega_{\mathrm{PM}} = \Omega(0)$ obtained without symmetry breaking for several values of SOC λ with fixed $U = 12.5t$, $J_{\mathrm{H}} = 2.5t$, $t = t_{xy} = t_{yz} = t_{xz} = 0.12\,\mathrm{eV}$. Background colors refer to the optimal orderings given by the lowest value of Ω_{opt}. By comparing the ordering patterns general trends for ordering vectors and orbital influence can be found. Discussion see text.

of Ω.

Before heading into a detailed description, we present in Fig. 3.4 the expectation values, which provide an useful insight in the orbital structure and allow a physical interpretation of the regimes. In Fig. 3.4 (a), the expectation values of the J_{LS} states are shown while Fig. 3.4 (b) focuses on the hole densities. The background colors are chosen as in Fig. 3.3. The gray colored symbols show the expectation values in the absence of any Weiss field, whereas the black symbols denote the populations in the optimal order. We examine the regimes step by step starting with very small $\lambda < 0.4t$.

In the limit of strong Coulomb repulsion U and Hund's coupling J_{H} exactly one orbital per site is doubly occupied (electron picture) or empty (hole picture). This leads to a total $L = 1$ and $S = 1$ which result in a ninefold degeneracy, cf. Sec. 2.1.4. In the absence of crystal field splittings or SOC as well as for really small SOC $\lambda < 0.4t$ this degeneracy is not resolved. Due to superexchange and the GKA rules, cf. Sec. 2.1.3,

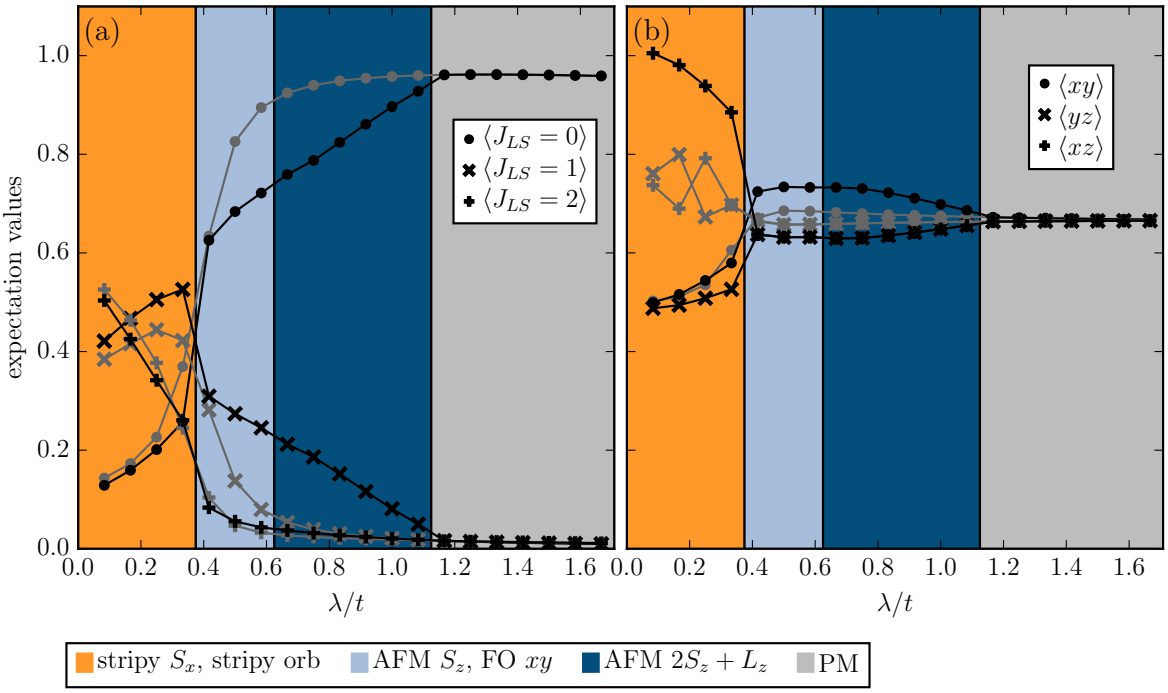

Figure 3.4: Expectation values for (a) the J_{LS} states and (b) the cubic harmonic orbitals in the non-magnetic case (gray symbols) and in the ordered regime (black symbols). The background colors give the order depending on SOC λ with fixed $U = 12.5t$, $J_\mathrm{H} = 2.5t$ and $t = t_{xy} = t_{yz} = t_{xz} = 0.12\,\mathrm{eV}$.

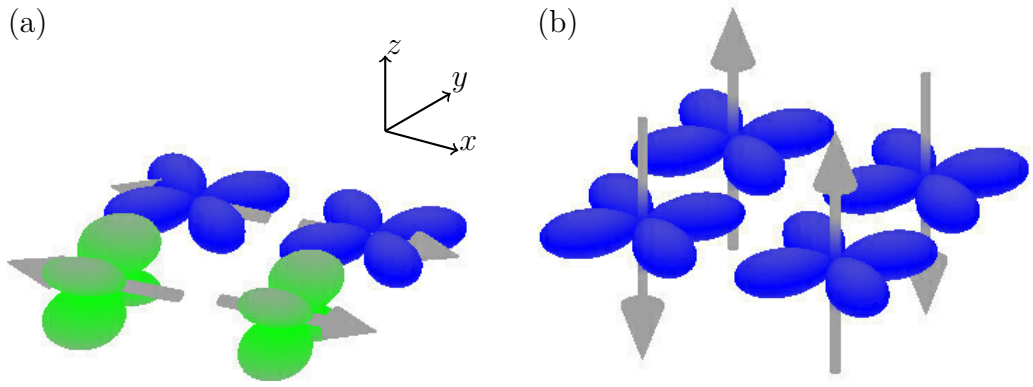

Figure 3.5: (a) In the absence of crystal field splittings and small SOC, $\lambda < 0.4t$, the ninefold degeneracy of the states is resolved by superexchange and the order follows the GKA rules. It results in a complex spin and orbital pattern having orthogonal ordering vectors $(0, \pi)$ and $(\pi, 0)$. The orbital drawn is the doubly occupied one (electron picture) or empty one (hole picture). The cartoon spins point in x-direction. (b) G-AF(1) type (= AFM S_z, FO xy) ordering for $0.4t \lesssim \lambda \lesssim 0.6t$. The spins point in z-direction in a checkerboard pattern. The xy-orbital is empty on every site (doubly filled for electrons).

the spins and orbitals form a complex stripy pattern, see Fig. 3.5 (a), which was also found by ED calculations [10]. The drawn orbital is the empty one (hole picture), the drawn spin represents the direction of the total $S = 1$ formed by the two other, half-filled orbitals. AFM coupling in x-direction is due to the half-filled xz-orbital hopping, which hops along the x-direction, and enhanced by the xy-orbital in the front row. In y-direction there are four channels of ferromagnetic superexchange given by an empty and a half-filled orbital, respectively. Here, the yz- and the xy-orbital participate in the superexchange.

This stripy spin and orbital pattern is indicated in our results by the orange background for $\lambda < 0.4t$. In Fig. 3.3, the stripy order in z- and x-direction has lower Ω than any other AFM order, if they are present at all. Small SOC has an influence on the orientation of the stripy order and makes S_x slightly preferable to S_z, more so for increasing SOC. Due to rotational in-plane symmetry, S_y should yield the same results as S_x. As SOC is too small to resolve the degeneracy of the nine states a description in the LS-scheme is not possible. This is supported by the expectation values $\langle J_{LS} = 0, 1, 2 \rangle$ which show a strangely mixed behavior, see Fig. 3.4 (a). In Fig. 3.4 (b) we gain insight into the orbital hole densities. The xz-orbital always contains a hole, i.e. is half-filled or $\langle xz \rangle = 1$, and the yz- and xy-orbitals each contain a hole on every second site, giving $\langle yz \rangle = \langle xy \rangle = 0.5$, cf. Fig. 3.5 (a). However, the orbital occupation number is not in accordance with the order we enforced on the lattice by VCA, see Tab. 3.1. Although the Weiss field suggests alternating xy- and xz-orbitals, the system chooses to order with

alternating yz and xy. We also applied the orbital pattern of Fig. 3.5 (a), but $\Omega(h')$ then only has a minimum at $h' = 0$.

We suggest that the stripy spin order is the most important aspect of the symmetry breaking. This is supported by the fact, that the orbital order has only a minor effect on Ω_{opt}, see Fig. 3.3. Additionally, calculations with a purely stripy S_x Weiss field show that the orbital occupation numbers already match the GKA rules. Therefore, the stripy spin order directly imposes an orbital order following the GKA rules on the cluster, which is actually slightly too large compared with the thermodynamic limit.

Increasing λ yields a regime that differs in two aspects: First, the stripy order vanishes and AFM ordering appears. Second, z-orientated ordering gets more favorable than x-orientated. The AFM regime is stabilized for $0.4t \lesssim \lambda \lesssim 1.1t$ and consists of two regimes: AFM S_z with FO xy order and AFM $2S_z + L_z$.

The AFM regime starts with S_z order strongly dominating over S_x order, see Fig. 3.3. Orbital ordering has only a slight impact as Ω_{opt} of AFM S_z and AFM S_z with FO xy nearly coincide. The stabilized regime is of AFM S_z type with the xy-orbital lifted on every site like sketched in Fig. 3.5 (b). Such a state has been found by [10] and is there denoted as G-AF(1) type. The hole densities in Fig. 3.4 (b) differ with $\langle xy\rangle > \langle yz\rangle \approx \langle xz\rangle$ once more contradicting the applied Weiss field. This is again due to the two-dimensional four-site cluster overestimating the orbital symmetry breaking because of the layered geometry.

In general, one should note that the favored Weiss field is not always in accordance with the physics of the system. It is essential to calculate the expectation values to get correct insights into the orbital occupations and orbital orderings. Regarding the spin, which is the dominant order parameter, the Weiss field gives reliable response. However, for small corrections given by the orbital order, the Weiss field may be misleading and must be checked by occupation-number calculations.

As discussed above, the J_{LS} states do not give a good description for small SOC $\lambda < 0.4t$. In the AFM regime, however, the $|J_{LS} = 0\rangle$ state almost entirely describes the unordered state for $\lambda \approx 0.6t$. The magnetic ordering increases weight in the $|J_{LS} = 1\rangle$ state as expected for excitonic magnetism [31], see the discussion of Fig. 3.2. The $|J_{LS} = 2\rangle$ state does not participate in the magnetic order and fast becomes irrelevant.

Other orbital orderings were suggested by e.g. [24]. We tried this AFM S_z order where three orbitals are involved in a complex ordering pattern, see the cartoon in Tab. 3.1. We found a non-vanishing Weiss field strength for this ordering but it is a bit less favorable than the AFM S_z with FO xy order.

The second part of the AFM regime is in $2S_z + L_z$ order which includes the orbitals in terms of the orbital momentum L_z. It is a bit similar to AFM S_z with FO xy order as it makes the xy-orbital different from the other two. Nevertheless, it is only slightly better than AFM S_z showing that the spin part is far more important for the symmetry breaking. Ordering in-plane direction is present but has significantly higher Ω_{opt}. Regarding the orbitals in Fig. 3.4 (b), the hole densities $\langle xy\rangle > \langle yz\rangle \approx \langle xz\rangle$ for $0.6t < \lambda < 1.1t$ but the occupations converge towards degeneracy in the PM regime.

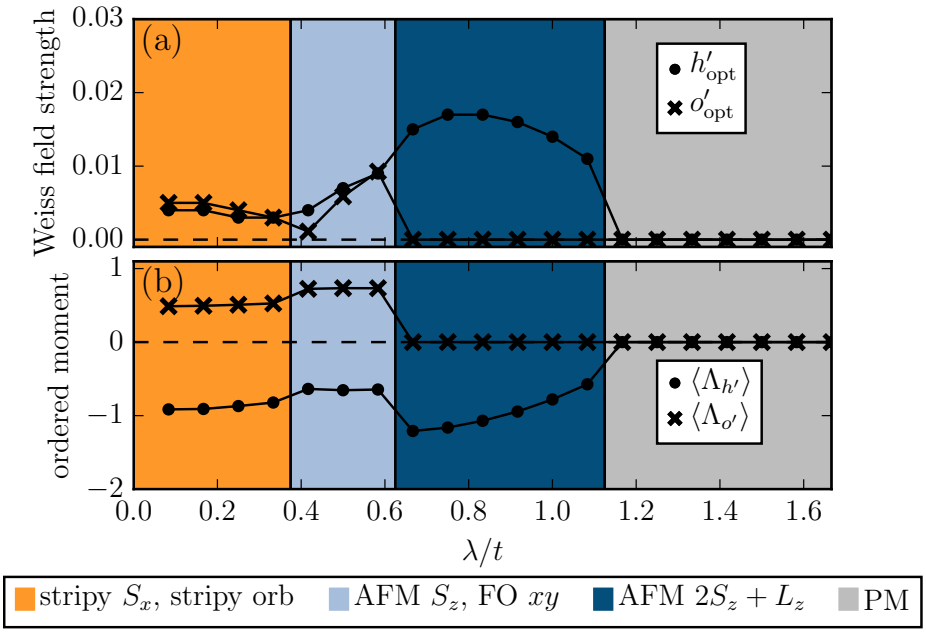

Figure 3.6: (a) Optimal Weiss field strengths h'_{opt} and o'_{opt} and (b) the ordered moments $\langle\Lambda_{h'}\rangle$ and $\langle\Lambda_{o'}\rangle$ for the spin and orbital part, respectively, over SOC λ. The background colors are chosen as in Fig. 3.3 with fixed $U = 12.5t$, $J_{\mathrm{H}} = 2.5t$ and $t = t_{xy} = t_{yz} = t_{xz} = 0.12\,\mathrm{eV}$. Discussion see text.

Still, the participation of the $|J_{LS} = 1\rangle$ state enables the magnetization but reduces for increasing λ until it converges to zero in the PM regime.

Finally, for $\lambda > 1.1t$ the splitting of the singlet and triplet caused by SOC inhibits any magnetic order and the model is PM. It is almost entirely described by the on-site singlet $|J_{LS} = 0\rangle$ and fully degenerate orbitals. Since λ is in the PM regime strong enough to suppress superexchange any impact of the layered geometry is likewise suppressed.

Figure 3.6 presents the optimal Weiss field strengths h'_{opt} and o'_{opt} as well as the ordered moments $\langle\Lambda_{h'}\rangle$ and $\langle\Lambda_{o'}\rangle$ for the regimes in Fig. 3.3. The orbital ordered moment is only present in the regimes with orbital order contribution. In the PM regime $\lambda > 1.1t$, $h' = o' = 0$ and the ordered moments vanish. Note that the Weiss field strength is no physical observable. However, Fig. 3.6 (a) shows that already small field strengths result in an ordered state.

In the stripy regime $\lambda < 0.4t$, the ordered moment of the spin $\langle\Lambda_{h'}\rangle \approx -1$ indicating an almost perfect alignment of the spins in x-direction, see Fig. 3.6 (b). The orbital ordered moment $\langle\Lambda_{o'}\rangle$ is rather constant and directly connected to the hole densities given in Fig. 3.4 (b). For $0.4t \lesssim \lambda \lesssim 0.6t$, the spin ordered moment is only $\langle\Lambda_{h'}\rangle \approx -0.65$ showing that the alignment of the spins in z-direction is less pronounced. The orbital ordered moment $\langle\Lambda_{o'}\rangle \approx 0.7 \approx \langle xy\rangle$ like in Fig. 3.4 (b). In the AFM $2S_z + L_z$ ordered regime,

$\langle \Lambda_{h'} \rangle$ is still quite large but tends to zero for increasing λ.

Figure 3.7 shows the one-particle spectral densities for selected λ-values over the path in the Brillouin zone given in Fig. 2.5. Each row has the same value of SOC while the columns show the spectra for the averaged superposition and resolved for each orbital separately. In total, there are four bands of which one is below the Fermi energy giving rise to a Mott insulator. Focusing on the superposition firstly, it is remarkable that SOC increases the band gap as expected in the LS-limit. Secondly, the bands loose their blurred features and become more defined and dispersive. For $\lambda = 0.25t$, the stripy S_x order with ordering vector $(\pi, 0)$ is directly visible in the spectra as $(0, \pi)$ and (π, π) as well as $(0, 0)$ and $(\pi, 0)$ coincide. In the AFM regimes, which start for $\lambda \gtrsim 0.4t$, the arc around the Γ-point (0,0) is doubled around the (π,π) point. This is because of the doubling of the unit cell that is present in AFM order. Within the orbitals a weight shift according to the hole densities in Fig. 3.4 (b) takes place. For $\lambda = 0.25t$ in Fig. 3.7 (a) the weight of the xz-orbital in the lowest band dominates. It is reduced in the AFM regime where all orbitals are equally occupied. As the xy-orbital is a bit more populated, its weight in the lowest band is slightly increased.

In conclusion, we found a complex stripy spin and orbital pattern for small $\lambda < 0.4t$ consistent with the GKA rules where finite $\lambda > 0$ prefers the spin to lie along x- rather than z-direction. Stronger SOC $0.4t \lesssim \lambda \lesssim 1.1t$ suppresses the orbital order so that an excitonic AFM regime arises. The symmetry breaking of the spins is the crucial step since the grand potentials of these possible AFM orders are nearly identical. The magnetism is driven only by admixture of the magnetic triplet $|J_{LS} = 1\rangle$ to the non-magnetic singlet $|J_{LS} = 0\rangle$ as proposed for excitonic magnetism. Finally, the excitonic magnetism is inhibited by too strong SOC $\lambda > 1.1t$ leading to a PM regime.

3.1.2 Parameter Study on a two-site Cluster

In the previous subsection, we investigated the influence of SOC on the ordering pattern. Now, we focus on each of the interaction parameters and their influence on the system separately, namely the hopping t, the on-site interactions Hund's coupling J_{H} and Coulomb interaction U as well as SOC λ again.

The following results are generated by VCA on a two-site cluster. This has the advantage of quite short calculation times (only several minutes compared to several hours for four-site clusters) and nevertheless provides us with general trends. However, the two-site cluster is not able to represent stripy ordering due to its limited geometry. We focus on the excitonic AFM regime and restrict to $\lambda \geq 0.25t$. As our results in the previous subsection indicate, the impact of orbital ordering is here negligibly small. The system is mainly ordered by the spins pointing out-of plane in AFM pattern (AFM S_z) and we only use this type of ordering here.

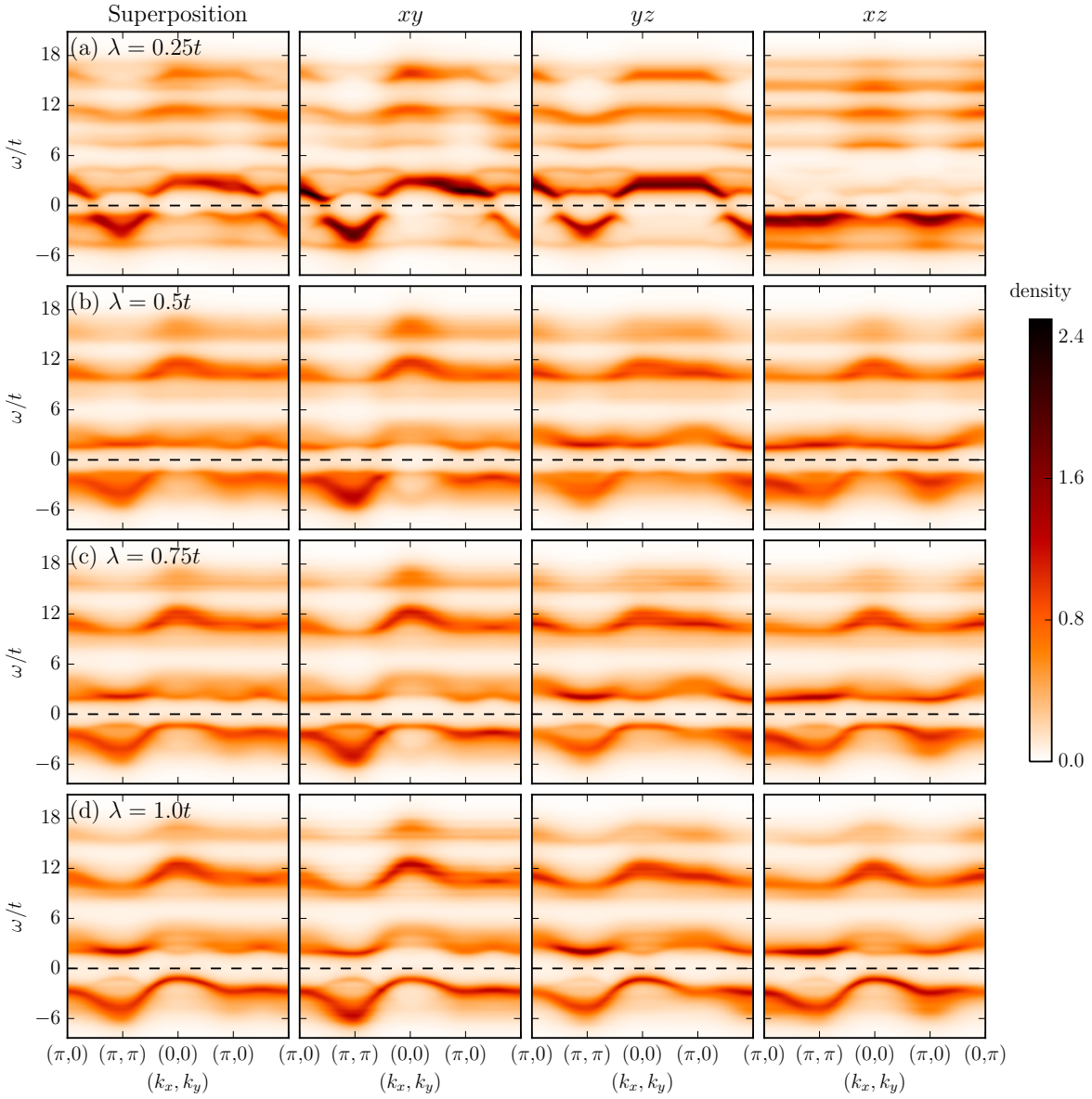

Figure 3.7: Spectral densities $A(\boldsymbol{k}, \omega)$ for fixed $U = 12.5t$, $J_{\mathrm{H}} = 2.5t$ and $t = t_{xy} = t_{yz} = t_{xz} = 0.12\,\mathrm{eV}$ for four values of SOC (a) $\lambda = 0.25t$, (b) $\lambda = 0.5t$, (c) $\lambda = 0.75t$ and (d) $\lambda = t$. Each row has the same value of SOC while the columns show the spectra for the averaged superposition and resolved for each orbital separately. The path in the Brillouin zone is sketched in Fig. 2.5. Discussion see text.

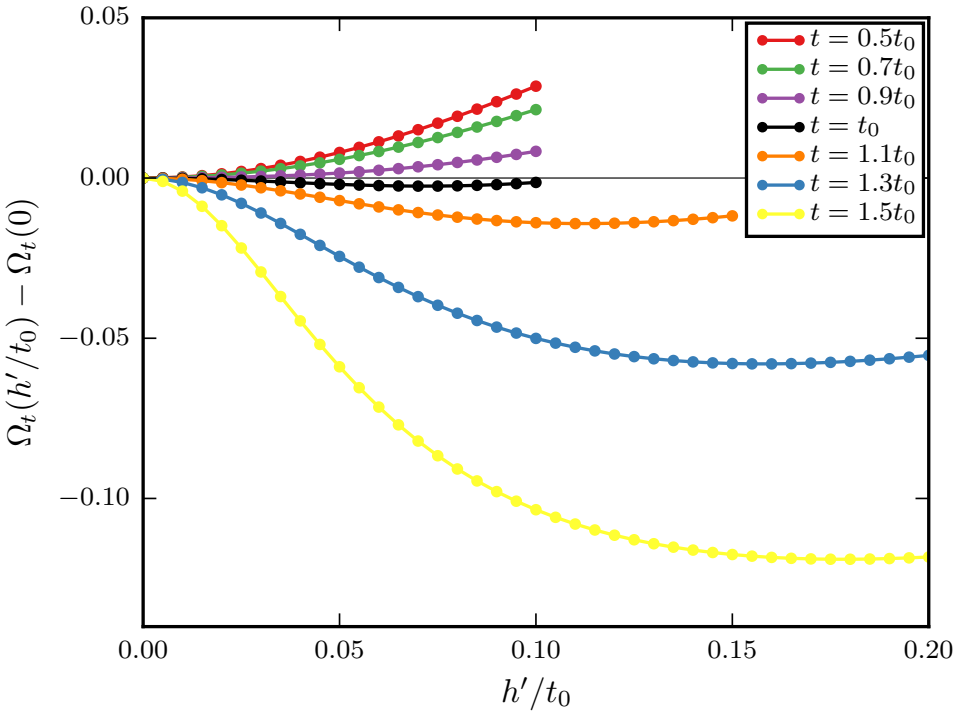

Figure 3.8: Grand potential $\Omega_t(h'/t_0)$ for different hopping values t over the Weiss field strength h' in AFM S_z order. We fix SOC $\lambda = t_0$, $U = 12.5t_0$ and $J_\mathrm{H} = 0.2U = 2.5t_0$ with the temporary energy scale $t_0 = 0.12\,\mathrm{eV}$. The hopping t stands for the main hopping terms $t = t_{xy} = t_{yz} = t_{xz}$. The optimal value of the magnetic field strength h'_opt is given by the minimum of each curve. The first three parameters have $h'_\mathrm{opt} = 0$ while the others have non-vanishing magnetic strengths. Therefore, increasing t drives the system into magnetism.

Impact of the Hopping Amplitude

To investigate the impact of the hopping amplitude t on the emergence of magnetism, we set a temporary energy scale $t_0 = 0.12\,\mathrm{eV}$ to vary t from $0.5t_0$ to $1.5t_0$. This alters the hopping strength in comparison to the other parameters λ, U and J_H but leaves their relation untouched. Again, only the main hoppings $t = t_{xy} = t_{yz} = t_{xz}$ are used. Further, we fix $\lambda = t_0$, $U = 12.5t_0$ and $J_\mathrm{H} = 0.2U = 2.5t_0$. Figure 3.8 shows the grand potential $\Omega_t(h'/t_0)$ relative to $\Omega_t(0)$ in dependence on the magnetic field strength h' of AFM S_z order for several hoppings t. Every curve shows a minimum. The first three curves have a minimum for $h'_\mathrm{opt} = 0$, the others for $h'_\mathrm{opt} \neq 0$. In the first case, $h'_\mathrm{opt} = 0$, the absence of the magnetic field is favorable. The system is non-magnetic. In the second case, the model prefers the suggested magnetic ordering.

For increasing t, the system undergoes a transition from non-magnetic to magnetic.

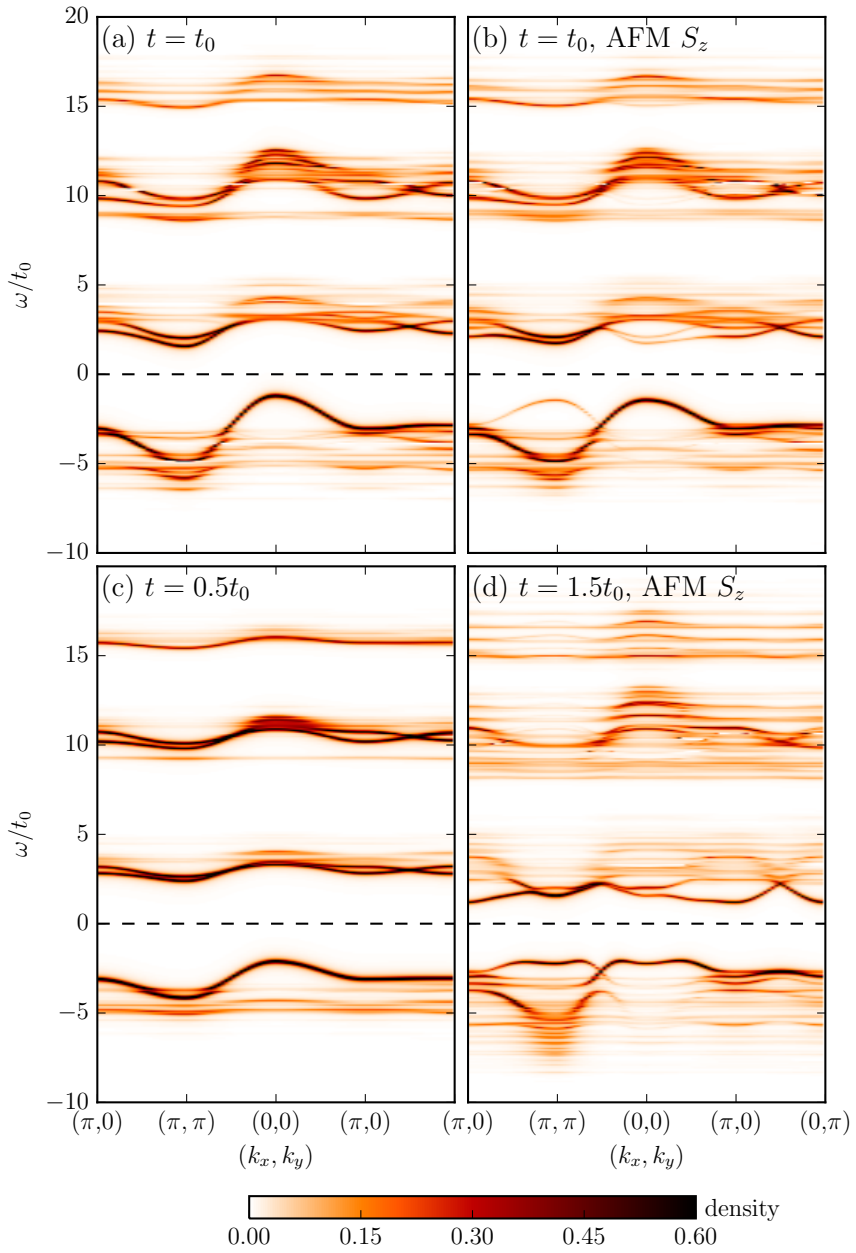

Figure 3.9: Spectral density $A(\boldsymbol{k}, \omega)$ for three values of hopping t over the path in the Brillouin zone given in Fig. 2.5. We fix SOC $\lambda = t_0$, $U = 12.5t_0$ and $J_\mathrm{H} = 0.2U = 2.5t_0$ with the temporary energy scale $t_0 = 0.12\,\mathrm{eV}$. The hopping $t = t_{xy} = t_{yz} = t_{xz}$ is (a) and (b) $t = t_0$, (c) $t = 0.5t_0$ and (d) $t = 1.5t_0$. The hopping increases the dispersion of the bands and reduces the band width. In every case except (a) where $h' = 0$, the spectral density is given for h'_opt. In the magnetic regime, (b) and (d), the characteristic doubling of the unit cell at (π, π) and $(0, 0)$ is present.

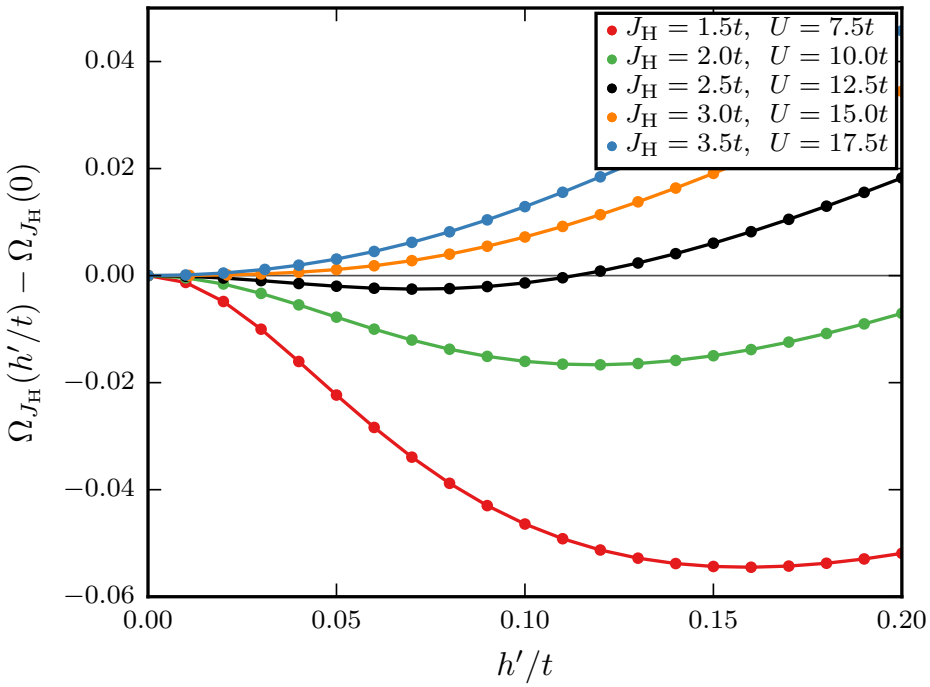

Figure 3.10: Grand potential $\Omega_{J_H}(h'/t)$ for different values of the on-site interaction (U, J_H) over the Weiss field strength h' in AFM S_z order with $t = t_{xy} = t_{yz} = t_{xz} = 0.12\,\text{eV}$, $\lambda = t$. By increasing the on-site interaction the system changes from a magnetic to a non-magnetic state due to the reduced superexchange $\propto 1/U$.

This shows that the hopping amplitude t is essential for magnetism. In other words this means that too strong SOC, Coulomb repulsion and Hund's coupling suppress magnetic structures. Increasing t increases the dispersion of the bands and therefore decreases the band gap, see Fig. 3.9 for the one-particle spectral densities. For every value of t shown in Fig. 3.9 the spectrum is calculated at $h' = h'_{\text{opt}}$, except in (a) where $h' = 0$. For $t = 0.5t_0$, Fig. 3.9 (c), there are four bands separated by large gaps. The dispersion is rather small. Increasing $t = t_0$, Fig. 3.9 (a), the band gaps narrow due to a stronger dispersion. For the same value $t = t_0$ but with the optimal Weiss field strength $h' = h'_{\text{opt}}$, the bands in Fig. 3.9 (b) look rather similar except there is a new arc in the lower band at (π, π) and at (0,0) in the upper band. This is a feature generated by the doubling of the unit cell when changing from a non-magnetic system with one atom per unit cell to a AFM system with two atoms per unit cell. This doubling can also be seen in Fig. 3.9 (d). Here, the bands are much broader and the band width is further reduced.

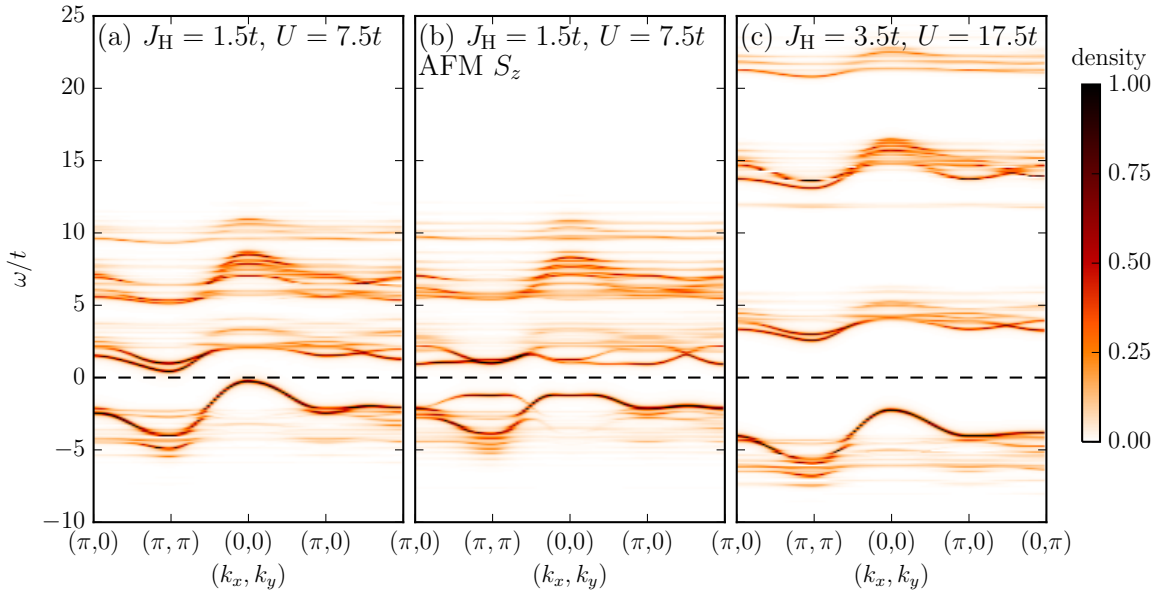

Figure 3.11: Spectral density $A(\boldsymbol{k}, \omega)$ for different values of the on-site interaction (U, J_H) over the path in the Brillouin zone given in Fig. 2.5. We fix $t = t_{xy} = t_{yz} = t_{xz} = 0.12\,\text{eV}$, $\lambda = t$. The on-site interaction is (a) $(U, J_H) = (7.5t, 1.5t)$ with $h' = 0$ and (b) $(U, J_H) = (7.5t, 1.5t)$ with $h' = h'_{\text{opt}}$ (AFM S_z regime). For (c) $(U, J_H) = (17.5t, 3.5t)$ there is no magnetic ordering as the band gap is too large.

Impact of on-site Interactions

Next, we probe the impact of Coulomb repulsion U and Hund's coupling J_H. Throughout this thesis, U and J_H are generally connected by $U = 5J_H$ if not indicated differently. Figure 3.10 shows the grand potential $\Omega_{J_H}(h'/t)$ for different values of the on-site interaction versus the AFM S_z order strength h'. Starting in the clearly AFM S_z ordered regime for small on-site interaction strength, the increase of J_H and U reduces the magnetic order strength and finally leads to a non-magnetic state for $(U, J_H) > (12.5t, 2.5t)$. Similar to the previously studied case regarding the hopping amplitude, too strong on-site interactions suppress magnetic order by reducing the superexchange $\propto 1/U$.

This is also visible in the spectral densities. Figure 3.11 (a) and (b) show the spectral densities for quite small $(U, J_H) = (7.5t, 1.5t)$ for $h' = 0$ and $h' = h'_{\text{opt}}$ which is then in the AFM S_z regime. The band gaps are quite small and in (b) it shows once more the doubling of the unit cell due to the AFM order. In Fig. 3.11 (c) the on-site interaction is increased to yield the non-magnetic regime. The band gaps are extremely large and it is obvious that superexchange is not able to compete against the splitting.

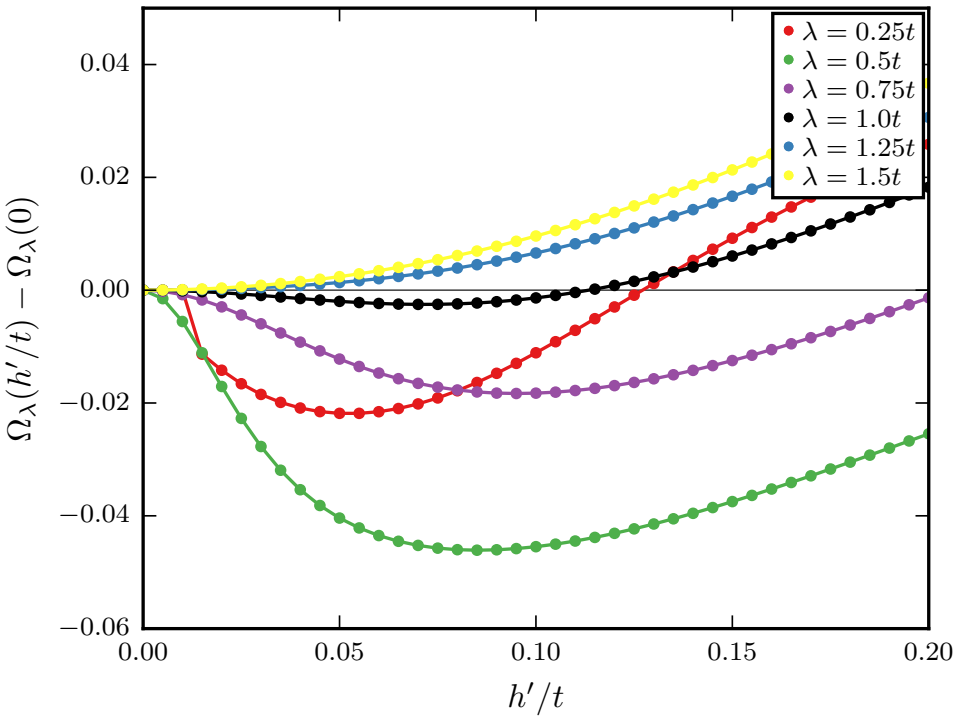

Figure 3.12: Grand potential $\Omega_\lambda(h'/t)$ for different values of SOC λ over the Weiss field strength h' in AFM S_z order with $t = t_{xy} = t_{yz} = t_{xz} = 0.12\,\text{eV}$, $U = 12.5t$ and $J_\text{H} = 2.5t$. Increasing SOC enlarges the distance between the non-magnetic singlet $|J_{LS} = 0\rangle$ and the magnetic triplet $|J_{LS} = 1\rangle$ and inhibits excitonic magnetism.

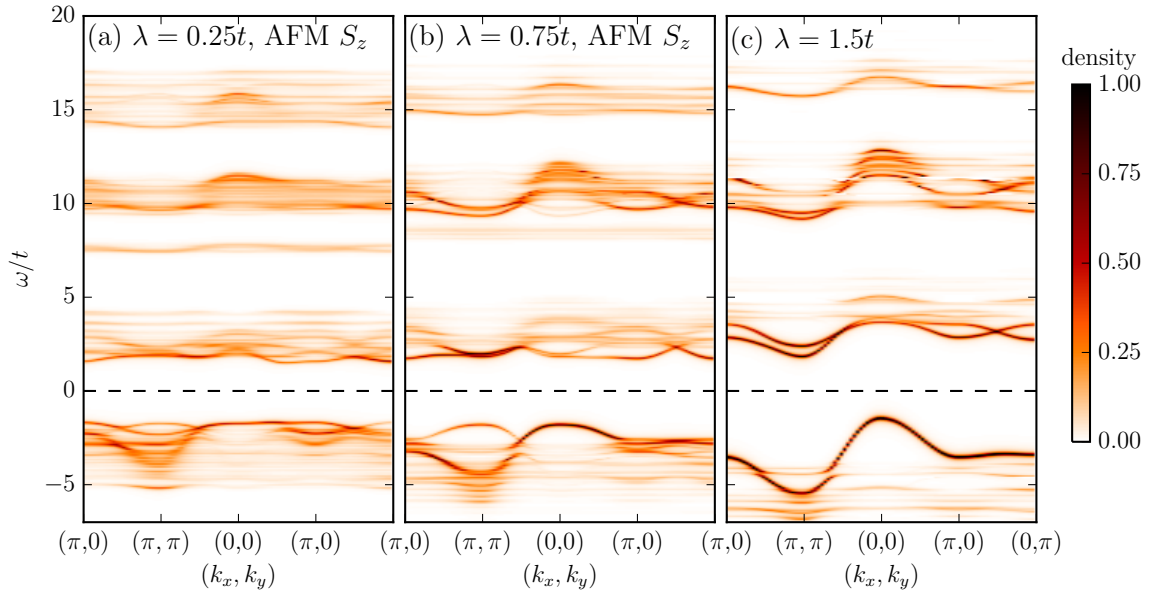

Figure 3.13: Spectral density $A(\boldsymbol{k}, \omega)$ for different values of SOC λ over the path of the Brillouin zone given in Fig. 2.5 with $t = t_{xy} = t_{yz} = t_{xz} = 0.12\,\text{eV}$, $U = 12.5t$, $J_\text{H} = 2.5t$ and (a) $\lambda = 0.25t$, (b) $\lambda = 0.75t$ and (c) $\lambda = 1.5t$. The first two spectra are in the magnetic regime, the last one is the non-magnetic regime as SOC increases the band gap and inhibits excitonic magnetism.

Impact of SOC

As the system is in the LS-regime, $\lambda < J_\text{H}$, SOC is directly involved in the splitting of the non-magnetic singlet $|J_{LS} = 0\rangle$ and the magnetic triplet $|J_{LS} = 1\rangle$, cf. Fig. 2.8. Hence, SOC is significant for the magnetism because the admixture of the magnetic triplet to the singlet is essential for the emergence of magnetism. Figure 3.12 shows the grand potential $\Omega_\lambda(h'/t)$ for different values of SOC λ in dependence on the AFM S_z order strength h'. Here, $U = 12.5t$ and $J_\text{H} = 0.2U = 2.5t$ are fixed with $t = t_{xy} = t_{yz} = t_{xz} = 0.12\,\text{eV}$. For small SOC, the model shows AFM S_z order. For $\lambda \geq 1.25t$ the magnetic order is no longer present as the singlet-triplet splitting is too large.

This can also be seen in Fig. 3.13 where the spectral densities for different λ-values are plotted. From (a) to (c) SOC is increased. In the first two cases, magnetic order is present as λ is small enough and the spectra are given in the magnetic regime visible by the arc at the (π, π) point. For increasing λ the magnetism is inhibited and the arc vanishes as shown in Fig. 3.13 (c) for $\lambda = 1.5t$.

Phase Diagram

To combine all trends found in the previous investigations a phase diagram of the two-site cluster is shown in Fig. 3.14 with $U = 5J_\text{H}$ and $t = t_{xy} = t_{yz} = t_{xz}$. The probed

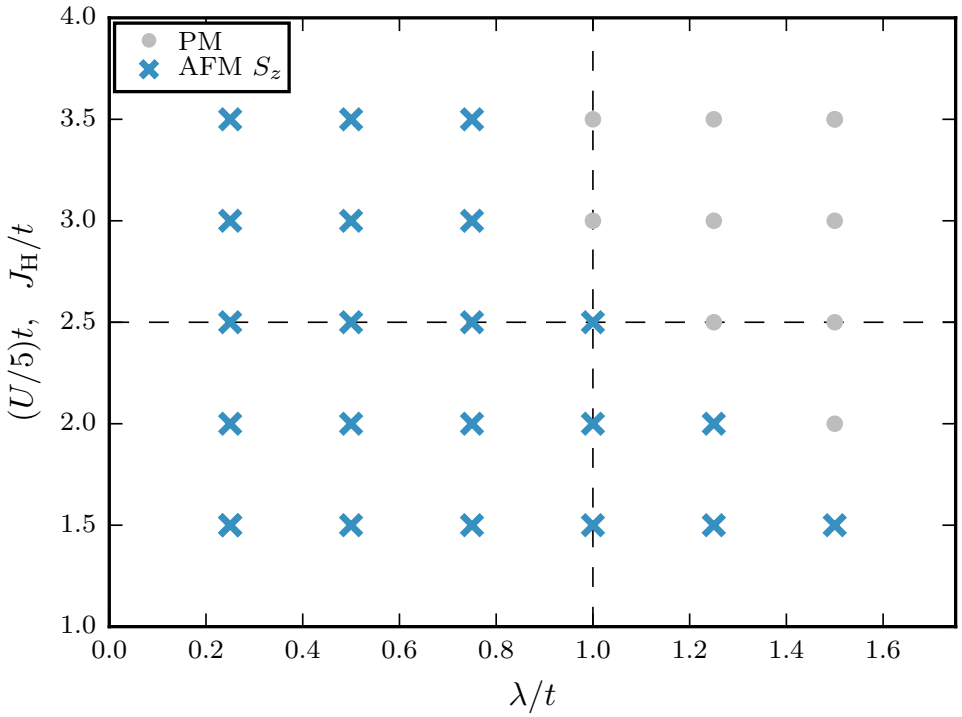

Figure 3.14: Phase diagram of a two-site cluster with hopping $t = t_{xy} = t_{yz} = t_{xz}$ and $U = 5J_\mathrm{H}$. The magnetic AFM S_z order is present for not too large on-site interaction (U, J_H) and SOC λ. Otherwise, the system is PM. The horizontal and vertical lines indicate the parameter sweeps of Fig. 3.10 and Fig. 3.12.

Weiss field is always AFM S_z as we detected this order as the dominating one. We are not interested in $\lambda < 0.25t$ as there is a stripy regime which can not be captured by a two-site cluster.

The phase diagram shows a large AFM region and a PM region which starts for large on-site interaction and SOC. The smaller the on-site interaction the longer stays the magnetic regime for increasing SOC. Strong on-site interaction pushes the bands apart which is supported by SOC. As long as the on-site interaction is small and the bands are closer together, superexchange is able to compete with the singlet-triplet splitting caused by SOC and magnetic order is possible. However, even for small on-site interaction there should be a non-magnetic regime for large SOC. In Fig. 3.14 SOC is too small to reach this non-magnetic regime.

3.2 Strong Spin-Orbit Coupling: The jj-Limit

In contrast to the previous sections where Hund's coupling was seen as the dominant force, this section focuses briefly on the transition to the other limit where $\lambda \gg J_{\mathrm{H}}$. There are some double-perovskite iridates such as Sr_2MIrO_6 (M=Y, Gd) which are likely to fulfill this criterium [18, 52, 76]. This is not the main focus of this thesis but it provides a deeper understanding of the interplay of SOC and the on-site interactions in general.

In Sec. 3.1.1, it showed that there is a critical SOC above which the magnetism is inhibited. With $\lambda \gg J_{\mathrm{H}}$, the system is always in this non-magnetic regime. Therefore, we investigate our model without any Weiss fields but nevertheless use VCA or CPT to determine the chemical potentials, the expectation values and the one-particle spectral densities. In addition to the expectation values of the J_{LS} states the investigation is now extended to the J_{jj} states, Eq. (2.24), and the Kramers doublets, Eq. (2.25), as they provide a useful description of the atomic level structure, cf. Sec. 2.1.4.

Figure 3.15 (a)-(d) shows the expectation values for the J_{LS} and the J_{jj} states, as well as the cubic harmonic orbitals and the Kramers doublets for SOC $0 < \lambda \lesssim 10t$. Hund's coupling J_{H} and Coulomb interaction U are fixed to $J_{\mathrm{H}} = 2.5t$ and $U = 12.5t$ with $t = t_{xy} = t_{yz} = t_{xz} = 0.12\,\mathrm{eV}$. The gray symbols give the values in the absence of magnetic Weiss fields, the black symbols give it in the optimal orders denoted by the background color. Figure 3.15 is an extension to Fig. 3.4 where SOC was restricted to $\lambda \leq 1.6t$. The white and red symbols are the special cases of $J_{\mathrm{H}} = 0$ and $J_{\mathrm{H}} = U/3 \approx 4.167t$ (both have fixed $U = 12.5t$). The first case drives the system immediately into the jj-limit while the second pushes it closer to the LS-regime.

Recalling the results of Fig. 3.4 the LS-regime is present for $\lambda \lesssim 1.6t$. Still in this regime the PM regime evolves since SOC splits the singlet and the triplet too far apart. This splitting even increases for increasing SOC, cf. Fig. 2.12. That is the reason why there is no magnetic order throughout the jj-regime.

Looking at Fig. 3.15 (a), it is easy to decide how far the LS-limit reaches. After the stripy regime where SOC is too small to resolve the degeneracy of the singlet and the triplet, the non-magnetic expectation value $\langle J_{LS} = 0\rangle$ is close to 1. The reduction in the magnetic regime is present because of the triplet admixture. In the non-magnetic regime $\langle J_{LS} = 0\rangle$ is still close to 1 up to $\lambda \approx 2t$. The excited states $|J_{LS} = 1, 2\rangle$ are nearly empty due to the large splitting. For higher λ, the population $\langle J_{LS} = 0\rangle$ decreases significantly while $\langle J_{LS} = 1, 2\rangle \approx 0$. The coupling to total $\boldsymbol{L}$ and $\boldsymbol{S}$ breaks down for $\lambda > 2t$ as SOC forces spin and angular momentum of each particle to couple separately.

Up to now, the J_{jj} states were useless as the population $\langle J_{jj} = 0\rangle < 0.8$, cf. Fig. 3.1 (a). Here, the J_{jj} states improve for increasing λ, see Fig. 3.15 (b). Although the excited states $|J_{jj} = 1, 2\rangle$ stay mostly empty, the population of the singlet $|J_{jj} = 0\rangle$ rises up to 1 and supersedes $\langle J_{LS} = 0\rangle$ for $\lambda \gtrsim 5t$. In between the two regimes $2t \lesssim \lambda \lesssim 5t$, none of the two descriptions are useful as $\lambda \approx J_{\mathrm{H}}$.

The Kramers states are the eigenstates of SOC neglecting Hund's coupling or Coulomb

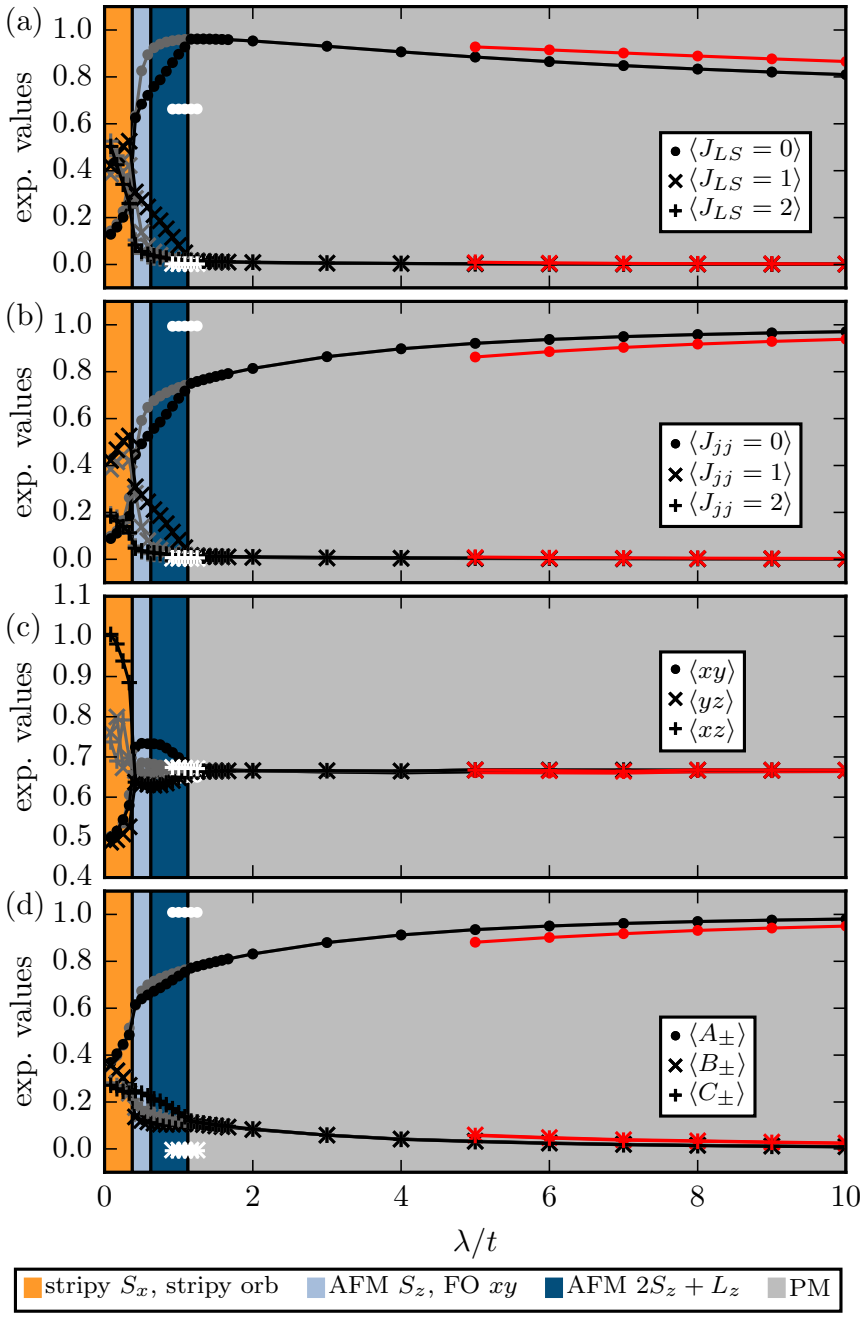

Figure 3.15: Expectation values for the (a) J_{LS} states, (b) J_{jj} states, (c) cubic harmonic orbitals and (d) Kramers states over SOC λ for fixed $U = 12.5t$, $J_{\mathrm{H}} = 0.2U = 2.5t$ and $t = t_{xy} = t_{yz} = t_{xz} = 0.12\,\mathrm{eV}$. The results of Fig. 3.4 for $\lambda < 1.6t$ are combined with those for strong SOC. The gray symbols give the values in the absence of magnetic Weiss fields, the black symbols give it in the optimal orders denoted by the background color. The white and red symbols are the special cases of $J_{\mathrm{H}} = 0$ and $J_{\mathrm{H}} = U/3 \approx 4.167t$ (both have fixed $U = 12.5t$). Discussion see text.

interaction, cf. Sec. 2.1.4. In the absence of TCF Δ, there is only a doublet ground state and a fourfold degenerate upper state. The ground state in the two-particle Kramers picture is given by $|A_+A_-\rangle$ i.e. both holes reside in the lowest Kramers doublet. Regarding the overlap of the Kramers ground state and the jj-limit ground state, we find that $\langle J_{jj} = 0|A_+A_-(\Delta = 0)\rangle = 1$. Therefore, the one-particle picture with two holes yields an appropriate description for the ground state in the large SOC limit. Figure 3.15 (d) shows the expectation values of the Kramers states. The Kramers $B_\pm$ and $C_\pm$ are nearly empty as the splitting to $A_\pm$ is proportional to λ. The population increase in $\langle A_\pm\rangle$ is nearly the same as in $\langle J_{jj} = 0\rangle$.

The different populations of the cubic harmonic orbitals in the LS-regime are no longer present in the jj-regime. The orbitals are nearly equally populated, see Fig. 3.15 (c). Since λ is in the PM regime strong enough to suppress superexchange any impact of the layered geometry is likewise suppressed. As the Kramers doublets ground state $|A_+A_-\rangle$ is a perfect description for the large SOC limit, it is obvious that the cubic harmonics are equally populated according to Eq. (2.25).

The black symbols in Fig. 3.15 denote a fixed Hund's coupling $J_\mathrm{H} = 0.2U = 2.5t$. The red symbols, however, show the calculations performed with $J_\mathrm{H} = U/3 \approx 4.167t$. A higher Hund's coupling should lead to an enhanced and extended LS-regime as J_H longer dominates λ. This can be verified in Fig. 3.15 (a) as $\langle J_{LS} = 0\rangle$ has higher expectation values than for smaller J_H. In an analogous manner, $\langle J_{jj} = 0\rangle$ and $\langle A_\pm\rangle$ are reduced in Fig. 3.15 (b) and (d). The degeneracy of the orbitals is not lifted as SOC is still dominating.

Another connection of the LS- and jj- schemes becomes evident when starting in the LS-regime for $\lambda \approx t$ and turning off Hund's coupling. Instantly, the system is driven into the jj-regime, given by the white symbols in Fig. 3.15.

Figure 3.16 shows the spectral densities for $\lambda = 1.67t,\ 5t$ and $10t$. For $\lambda = 1.67t$ the bands show a rather small gap which increases for $\lambda = 5t$. Further, the three upper bands approach. For $\lambda = 10t$ the band gap enlarges even more and the number of upper bands reduces to two. The latter are quite close and resemble the Kramers band structure with a doublet ground state and a quartet excited state, cf. Fig. 2.11.

3.3 Reduced Impact of t_{2g} Hopping Anisotropy in the excitonic Regime

Regarding only the strongest hopping parameters t_{xy}, t_{yz} and t_{xz} as done in Sec. 3.1.1, the orbitals xy, xz and yz do not participate equally in the nearest neighbor hopping process. As discussed in Sec. 2.1.2, the xy-orbital is allowed to hop in x- and y-direction while yz and xz are only allowed to hop in y- and x- direction, respectively. This hopping anisotropy is characteristic for t_{2g} orbitals and is, for example, responsible for the stripy pattern found at $\lambda < 0.4t$, cf. Sec. 3.1.1. We investigate here the impact of the hopping

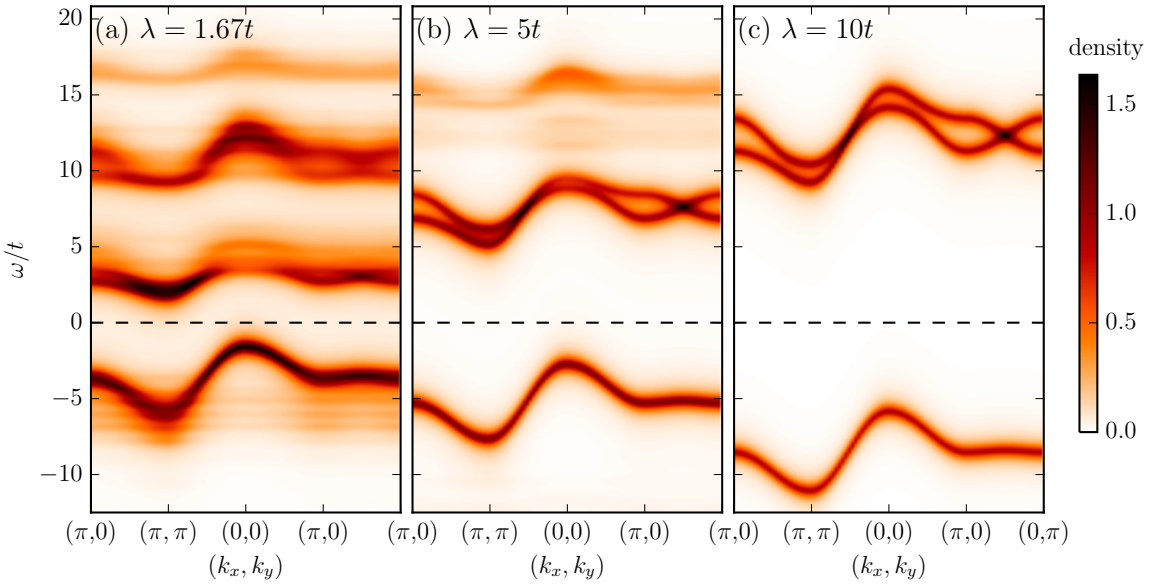

Figure 3.16: Spectral density $A(\boldsymbol{k}, \omega)$ for SOC (a) $\lambda = 1.67t$, (b) $\lambda = 5t$, (c) $\lambda = 10t$ along the path in the Brillouin zone given in Fig. 2.5 for fixed $U = 12.5t$, $J_\mathrm{H} = 0.2U$ and $t = t_{xy} = t_{yz} = t_{xz} = 0.12\,\mathrm{eV}$. The band gap between the lowest and the upper bands enlarges for increasing SOC. Further, the upper bands move close together. For $\lambda = 10t$ the band structure resembles the one given by the Kramers doublets in Fig. 2.11.

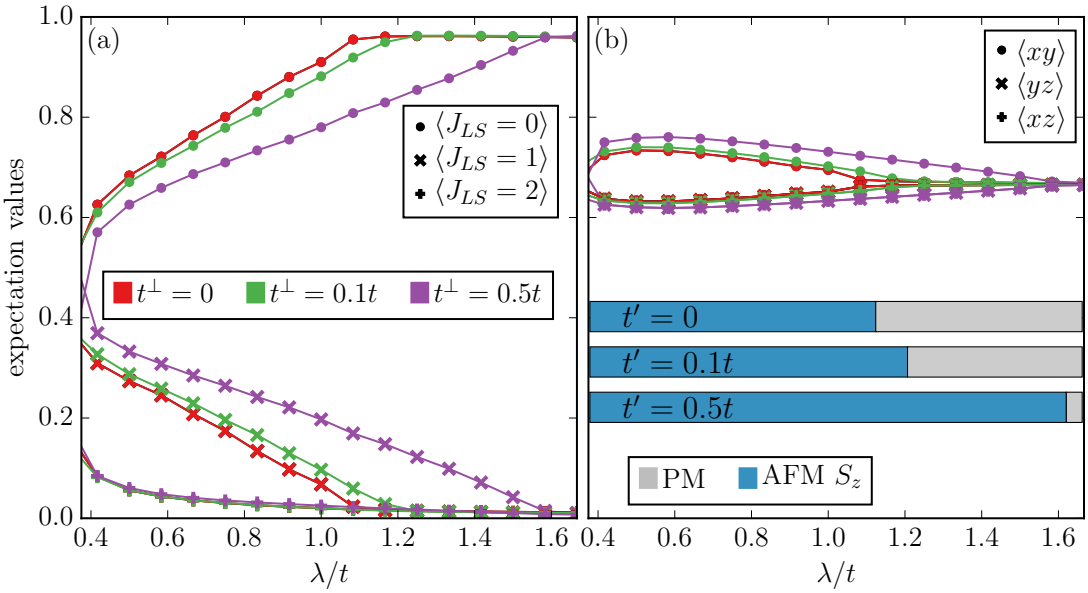

Figure 3.17: Expectation values of (a) the J_{LS} states and (b) the orbitals over SOC λ for different values of the "orthogonal" hopping $t^\perp$ in the optimal order. The model parameters are set to $t = t_{xy} = t_{xz} = t_{yz} = 0.12\,\text{eV}$, $t^\perp = t^\perp_{xz} = t^\perp_{yz}$, $U = 12.5t$ and $J_\text{H} = 2.5t$. The regimes are PM and AFM S_z as found in the previous investigations and their boundaries depend SOC. The regimes for every value of $t^\perp$ are shown in the inset of (b). It is apparent from this chart that the addition of $t^\perp$ shrinks the PM regime and extends the AFM regime. With small $t^\perp = 0.1t$, the AFM regime reaches up to a bit higher λ than for vanishing $t^\perp$. Increasing $t^\perp$ even more shifts the PM regime to $\lambda > 1.6t$.

anisotropy on the excitonic regime $\lambda > 0.4t$ by reducing it towards a more isotropic model. We introduce an "orthogonal" hopping $t^\perp$, see Eq. (2.9), which allows the yz- and xz-orbital to hop in x- and y-direction, respectively. The new hopping $t^\perp$ is equal for both orbitals i.e. $t^\perp = t^\perp_{xz} = t^\perp_{yz}$.

Figure 3.17 shows the expectation values of the J_{LS} states and the orbitals with fixed $U = 12.5t$, $J_\text{H} = 2.5t$ and $t = t_{xy} = t_{xz} = t_{yz} = 0.12\,\text{eV}$ for $0.4t < \lambda < 1.7t$ and three different hopping amplitudes $t^\perp = 0,\ 0.1t,\ 0.5t$ in the optimal orders. The curve with $t^\perp = 0$ was already discussed in Fig. 3.4 and is reproduced here for comparison. The inset in Fig. 3.17 (b) depicts the regimes which depend on λ as well as on $t^\perp$.

For $t^\perp = 0$, the model reveals two regimes depending on λ which are already known from the previous section. There is the AFM S_z order for intermediate SOC and the PM regime for large SOC. As discussed before the orbital order has not much influence on the system and the AFM S_z order is a sufficient order parameter in this model system.

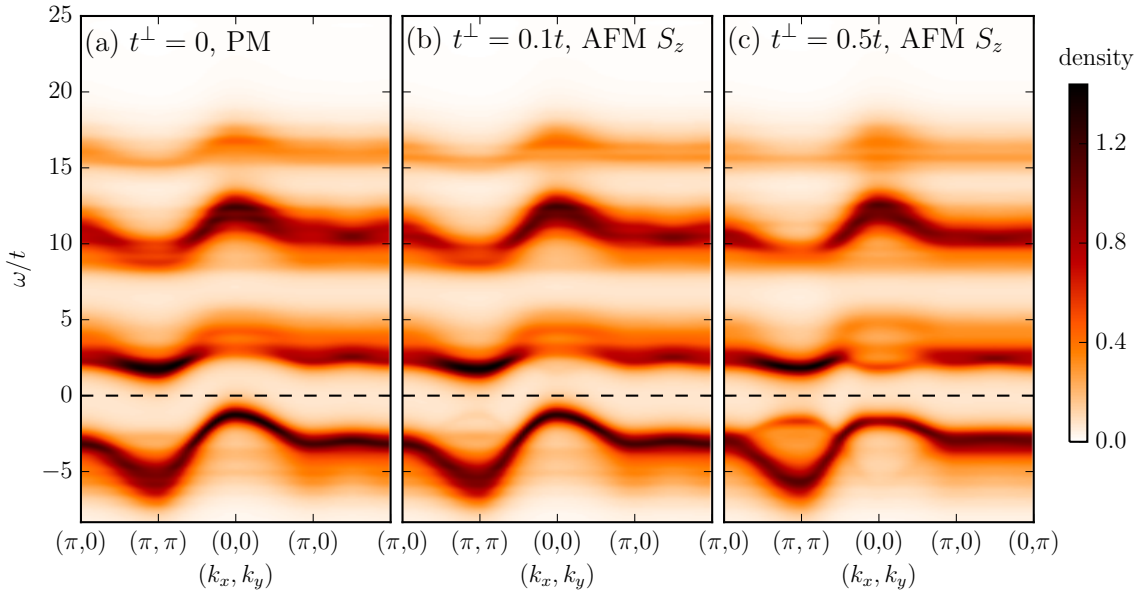

Figure 3.18: Spectral density $A(\boldsymbol{k}, \omega)$ for the "orthogonal" hopping (a) $t^\perp = 0$, (b) $t^\perp = 0.1t$, (c) $t^\perp = 0.5t$ along the path in the Brillouin zone given in Fig. 2.5 for SOC $\lambda = 1.167t$. The spectral density in the AFM regime in (c) shows the characteristic doubling of the unit cell. Apart from the doubling feature, the spectra look quite similar. The band widths have the same value and the bands show almost equal dispersion.

The PM regime starts at $\lambda \approx 1.1t$ for $t^\perp = 0$. The magnetic behavior is directly visible in the expectation values of the J_{LS} states in Fig. 3.17 (a). The expectation value $\langle J_{LS} = 1 \rangle$ is non-vanishing and $\langle J_{LS} = 0 \rangle$ is reduced in the AFM regime. As soon as it gets non-magnetic, the population of $|J_{LS} = 1\rangle$ disappears and $\langle J_{LS} = 0 \rangle \approx 1$. Regarding the cubic harmonics, the xy-orbital is slightly more populated in the magnetic regime. In the PM regime the orbitals contribute equally.

Adding $t^\perp$ alters the regimes slightly, see Fig. 3.17 (b), by extending the AFM regime up to $\lambda \approx 1.2t$. Regarding $t^\perp = 0.5t$, the magnetic regime spreads even further up to $\lambda \approx 1.6t$. This is also reflected in the expectation values as the population in $|J_{LS} = 1\rangle$ decreases much more slowly over λ than before. Vice versa, $\langle J_{LS} = 0 \rangle$ gains weight more slowly. For $t^\perp = 0.5t$, xy is only a bit more populated than for $t^\perp = 0.1t$ but remains favored for large λ.

The spectral densities for fixed $\lambda = 1.167t$ are given in Fig. 3.18. At this value the $t^\perp = 0$ model has just reached the non-magnetic regime, $t^\perp = 0.1t$ is at the end of the AFM regime and $t^\perp = 0.5t$ is still deep in the AFM regime. For the latter, the spectral density shows the characteristic doubling of the unit cell. Apart from the doubling feature, the spectra look quite similar. The band widths have the same value and the bands show almost equal dispersion.

In summary, the isotropic hopping parts $t^{\perp}$ somewhat extend the magnetic regimes. This can be understood by noting that the total kinetic energy increases for $t^{\perp} \neq 0$ and therefore supports excitonic magnetism even for a larger SOC λ. However, a small isotropic channel $t^{\perp}$ does not make much difference in the population of the orbitals. This is quite surprising as one could have supposed that the newly opened hopping channel $t^{\perp}$ would alter the occupation of the orbitals to become more equal [31]. However, the dominant effect appears to be the extension of the AFM regime, which comes together with a slight orbital polarization. The latter is not only reduced, but even slightly increased.

4 Interplay of Spin-Orbit Coupling and Tetragonal Crystal Field

The interplay of on-site interactions and SOC reveals magnetic regimes with several orbital and spin orderings as shown in Sec. 3.1. This so-called excitonic magnetism [31] can be explained by the admixture of the magnetic triplet to the non-magnetic singlet. However, many transition metal oxides have lower symmetry than cubic such as the elongation or flattening of the RuO_6 octahedra represented by the TCF, see Eq. (2.1). We investigate the TCF for flattened octahedra, $\Delta > 0$, motivated by the low-temperature phase of Ca_2RuO_4 [49, 77].

Let us briefly remember the main impact of the TCF on the atomic LS-limit which was discussed in detail in Sec. 2.1.4. Figure 2.9 shows this scenario with the energy levels given by one-site ED calculations. Starting from the scenario discussed in Sec. 3.1 with $\Delta = 0$, the level structure is given by the ground state singlet $|J_{LS} = 0\rangle$ and the higher lying triplet $|J_{LS} = 1\rangle$ and quintet $|J_{LS} = 2\rangle$. TCF splits the triplet as well as the quintet by raising the xy-orbital. The triplet splits into the singlet S_3 and the doublet $D_{1/2}$ with lower energy, see Fig. 2.9. The latter and the ground state singlet S_0 build the new ground state manifold for $\lambda = 0$. In this case, $\lambda = 0$, the ground state is threefold degenerate and given by the spin 1 of the two holes in the xz- and yz-orbitals.

Throughout this chapter, we investigate the system in the LS-regime by fixing $J_\mathrm{H} = 2.5t > \lambda$ with $U = 5J_\mathrm{H}$. Further, we take only the simplest hopping into account, $t = t_{xy} = t_{yz} = t_{xz}$, as the main focus is on the interplay of SOC and TCF. In Sec. 4.1, we investigate magnetic ordering for fixed moderate TCF $\Delta = 0.5t$ and varying SOC $0.1t < \lambda < 1.6t$, similar to the calculations done in Sec. 3.1.1. In contrast to the previous results, TCF forces the spin to order in x-direction instead of z-direction. In Sec. 4.2, the influence of TCF on the magnetic state obtained for fixed small SOC $\lambda = 0.75t$ is investigated and found to reorient spins. For rather strong $\lambda = 1.67t$, the SOC-stabilized non-magnetic regime is shown to be stable with respect to TCF up to $\Delta = 4t$. However, we observe that AFM order can be induced by TCF leading to a quantum critical point for intermediate SOC in Sec. 4.3. Section 4.4 summarizes all regimes and ordering patterns in the LS-regime for the interplay of SOC and TCF. Finally, we investigate the impact of TCF in the jj-regime in Sec. 4.5.

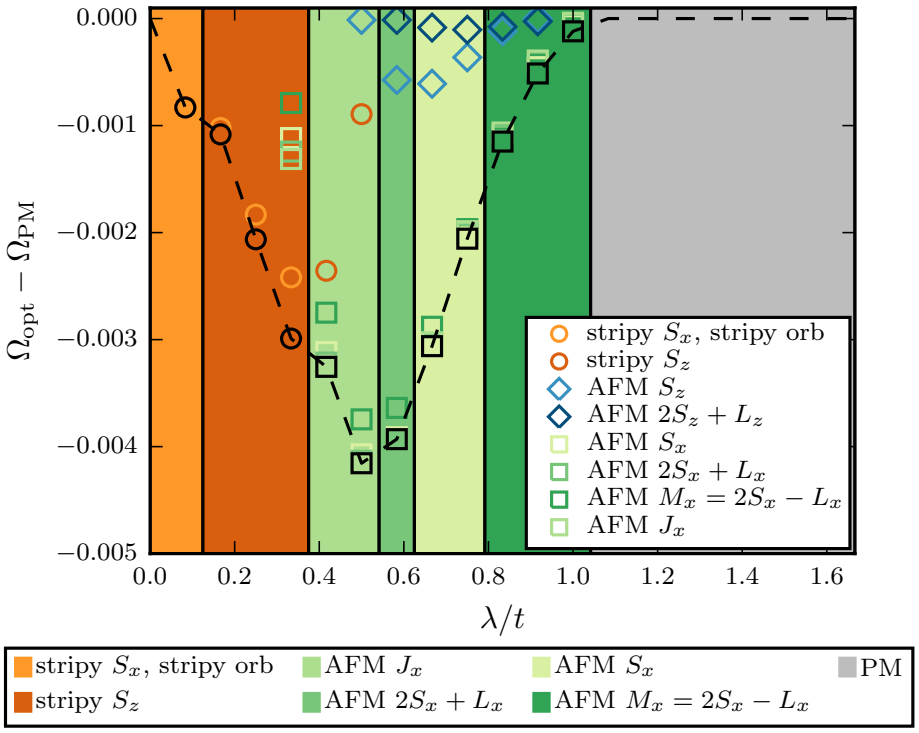

Figure 4.1: Grand potential Ω_{opt} of various ordered states relative to the results Ω_{PM} obtained without symmetry breaking depending on SOC λ for fixed TCF $\Delta = 0.5t$, $U = 12.5t$, $J_{\mathrm{H}} = 2.5t$ and $t = t_{xy} = t_{yz} = t_{xz}$. Background colors are defined by optimal orderings.

4.1 Magnetic Regimes for small TCF $\Delta = 0.5t$

In Sec. 3.1.1, we investigated the magnetic regimes depending on the strength of SOC for $\Delta = 0$, see Fig. 3.3. Now, we repeat the calculation but add TCF $\Delta = 0.5t$, which results in various regimes with stripy and checkerboard AFM order. Figure 4.1 shows the regimes as colored backgrounds as well as the grand potential of each order Ω_{opt} relative to the non-magnetic Ω_{PM} depending on SOC λ.

We start by discussing the stripy ordered regimes with $\lambda < 0.4t$. There is a short stripy S_x regime with stripy orbital order as given in Fig. 3.5 (a) for $\lambda \lesssim 0.1t$, followed by a stripy S_z regime for $0.1t \lesssim \lambda < 0.4t$. Only the stripy orders have non-zero order parameters in this range of λ. S_x and S_z lie very close together with first a tiny favor to x-ordering, and later significant advantage for S_z order. A similar situation was investigated in Sec. 3.1.1 especially in Fig. 3.3 without TCF. The stripy pattern is a consequence of the high (ninefold) degeneracy at $\lambda = \Delta = 0$, which is not lifted strongly enough by the present $\Delta = 0.5t$ and $\lambda < 0.4t$. The main effect of TCF $\Delta = 0.5t$ is to overcome the orbital asymmetry observed for $\Delta = 0$ in Sec. 3.1.1 and thus to reorient the spins.

Similar to the stripy phase in Fig. 3.4 (a), the J_{LS} states in Fig. 4.2 (a) do not provide an useful description of the ground state as the splitting between the states is too small. The similarity to Fig. 3.4 (b) is also apparent in the hole densities in Fig. 4.2 (c) where the xz-orbital is populated the most following the GKA rules. Note that orbital order is present and similar throughout the stripy phase, even though the stripy S_z does not require fictitious orbital-ordering fields.

As the J_{LS} states only describe the system in the absence of TCF, we calculate the eigenstates of the Hamiltonian including U, J_{H}, λ and Δ, c.f. Sec. 2.1.4. The ground state is given by a singlet S_0, see Fig. 2.9. As we are interested in the low-energy subspace, we focus on the ground state S_0 as well as the excited doublet $D_{1/2}$ and the excited singlet S_3. As can be seen from their expectation values, given in Fig. 4.2 (b), they do indeed add to almost 1, justifying this focus. For $\lambda < 0.4t$ the singlet S_0 and the doublet $D_{1/2}$ show reversed populations $\langle D_{1/2} \rangle > \langle S_0 \rangle$. Since SOC is responsible for the splitting between singlet and doublet but is too small here, the states are nearly degenerate and the population reversion arises.

For $\lambda \gtrsim 0.4t$ the AFM regimes with in-plane orientation start. Compared to Fig. 3.3 there is a reorientation from out-of-plane direction to in-plane direction, caused by the TCF and matching the spin order measured in Ca_2RuO_4, see Sec. 2.2. Even if the x-regimes may alter a bit in their characteristics regarding the orbital contribution, Fig. 4.1 makes clear that it has only a slight impact. The AFM ordering is mainly driven by the spin orientation as the AFM ordering out-of-plane is also present (diamond symbols) but far weaker than in-plane order. For $\lambda > t$, no magnetic order is found.

Regarding the expectation values in Fig. 4.2 (a) $\langle J_{LS} = 0 \rangle$ increases its weight up to ≈ 0.9 for $\lambda > 0.7t$. The $|J_{LS} = 1, 2\rangle$ states tend to zero for increasing SOC in the absence of Weiss fields. As observed in Fig. 3.4 (a), the $|J_{LS} = 1\rangle$ state gets populated the way

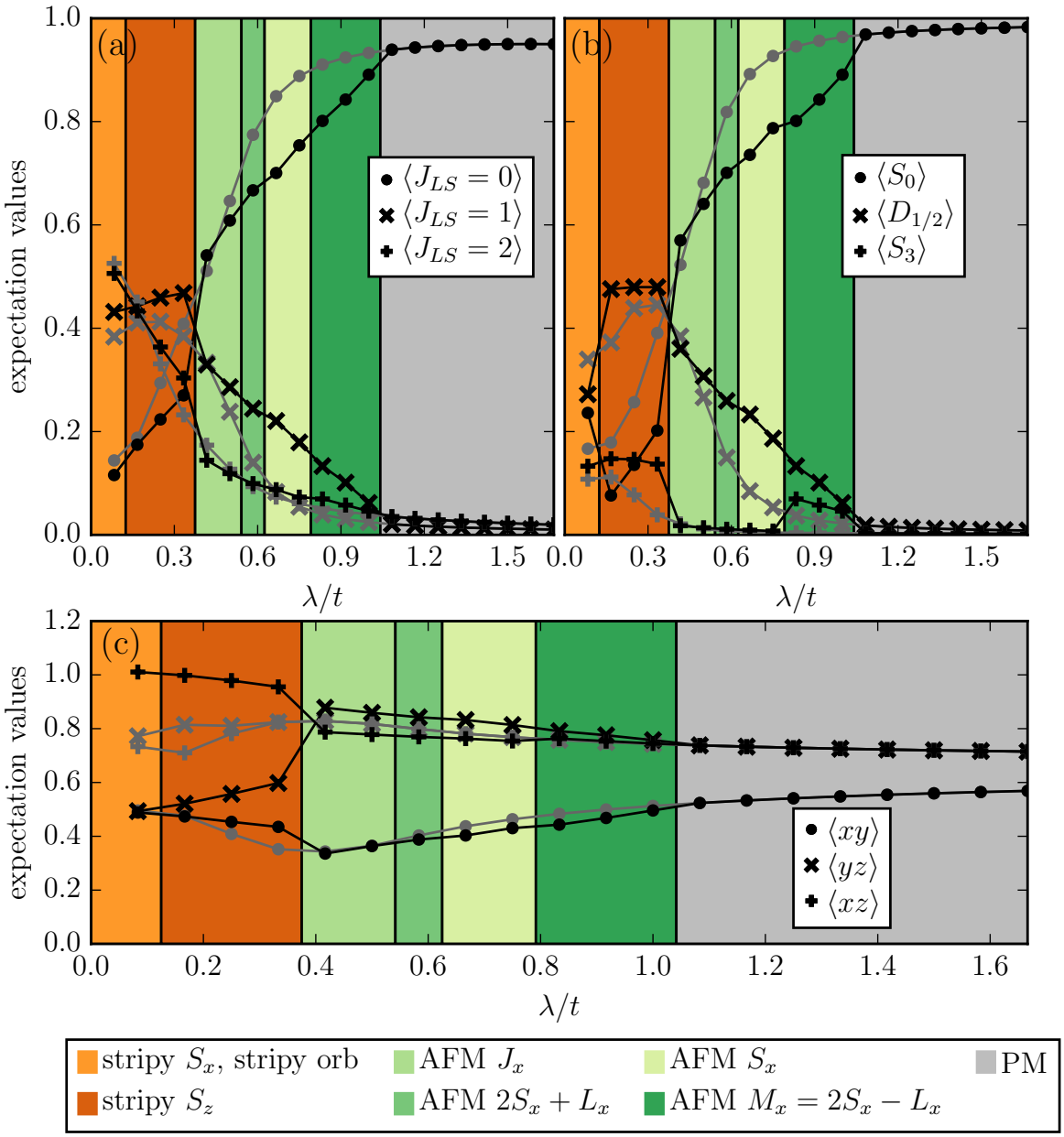

Figure 4.2: Expectation values for (a) the J_{LS} states, (b) the one-site ED states and (c) the orbitals. TCF is fixed to $\Delta = 0.5t$ with $U = 12.5t$, $J_{\mathrm{H}} = 2.5t$ and $t = t_{xy} = t_{yz} = t_{xz}$. The gray and black symbols each denote the expectation values in the absence of Weiss fields and in the optimal magnetic regime which is given by the colored background. The order changes from stripy to AFM order with in- and out-of-plane orientation depending on λ. Discussion see text.

$\langle J_{LS} = 0\rangle$ is reduced showing the admixture of the triplet to the singlet in the magnetic regime. The $|J_{LS} = 2\rangle$ state does not contribute to the magnetism. For $\lambda > t$, the PM regime starts with $\langle J_{LS} = 1, 2\rangle \approx 0$.

The one-site ED states in Fig. 4.2 (b) behave in a similar way with $\langle S_0\rangle \gg \langle D_{1/2}\rangle > \langle S_3\rangle \approx 0$. In the magnetic regime, $0.4t < \lambda < t$, the population is shifted from the singlet S_0 to the doublet $D_{1/2}$ while S_3 does not participate because of its separation from the doublet caused by TCF, see Fig. 2.9.

In contrast to the results gained in Fig. 3.4 (b), the hole density in the xy-orbital $\langle xy\rangle < \langle xz\rangle \approx \langle yz\rangle$ due to the TCF lifting it, see Fig. 4.2 (c). For increasing SOC, the difference in the hole densities diminishes as SOC reduces the orbital polarization.

4.2 Increasing TCF for small and large SOC

Next, we investigate the impact of TCF on two systems with fixed SOC. The first one, $\lambda = 0.75t$, is in the magnetic regime with TCF influencing the orientation of the spin order. The second one, $\lambda = 1.67t$, is in the PM regime and stays non-magnetic even for high TCF.

Increasing TCF for small SOC $\lambda = 0.75t$

To investigate the influence of TCF on the system in the magnetic order SOC is set to $\lambda = 0.75t$ resulting in AFM $2S_z + L_z$ order for $\Delta = 0$, as observed in Fig. 3.3. Increasing TCF, the magnetic order changes from out-of-plane to in-plane direction, see Fig. 4.3. For $\Delta < 0.3t$, the system is out-of-plane ordered but changes from AFM $2S_z + L_z$ to AFM S_z with FO xy participation. Then, for $\Delta \gtrsim 0.3t$ the order flips to in-plane ordering as observed for Ca_2RuO_4, first AFM M_x, then AFM S_x and finally AFM $2S_x + L_x$ order.

The gray symbols in Fig. 4.3 show the expectation values without Weiss field whereas the black symbols give them in the optimal order denoted by the colored background. We first focus on the J_{LS} states, Fig. 4.3 (a). In the absence of Weiss fields and for $\Delta = 0$, the ground state is perfectly described by the $|J_{LS} = 0\rangle$ state with the $|J_{LS} = 1, 2\rangle$ states having no weight. For increasing TCF, the levels split and the $|J_{LS} = 2\rangle$ state gains occupation taking part in the orbital polarization. This shows that the description in terms of J_{LS} states gets worse as the LS-picture does not include any influence of the TCF splitting. Regarding the expectation values in the optimal order, $\langle J_{LS} = 1\rangle$ is increased in the way $\langle J_{LS} = 0\rangle$ is lowered. This shows that the concept of excitonic magnetism observed in Sec. 3.1.1 even exists in the presence of TCF. What is new is that the $|J_{LS} = 2\rangle$ state becomes relevant for increasing Δ and thus contributes to orbital polarization. However, $\langle J_{LS} = 2\rangle$ stays nearly constant with and without magnetic ordering and is thus not involved in the magnetic ordering.

Moreover, Fig. 4.3 (b) shows the one-site ED eigenstates. For the non-magnetic calculation the singlet S_0 describes the situation quite well as $\langle S_0\rangle \approx 1$. Adding the magnetic

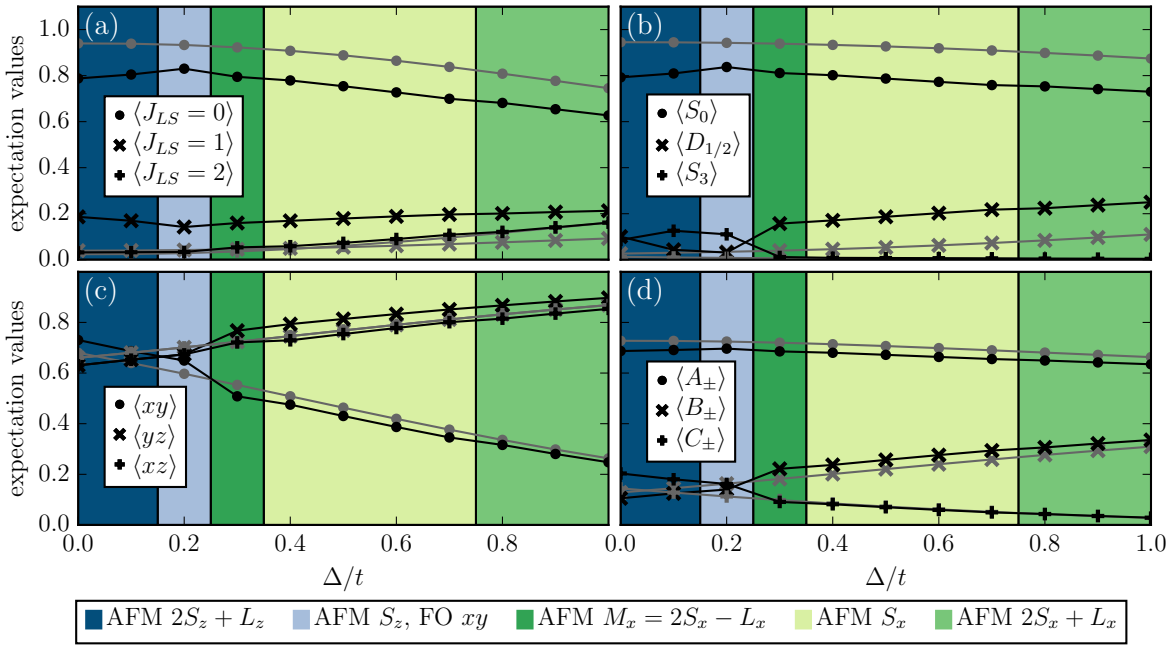

Figure 4.3: Expectation values for fixed SOC $\lambda = 0.75t$ and increasing TCF Δ with $U = 12.5t$, $J_\mathrm{H} = 2.5t$ and $t = t_{xy} = t_{yz} = t_{xz} = 0.12\,\mathrm{eV}$. The gray and black symbols each denote the expectation values in the absence of Weiss fields and in the optimal magnetic regime which is given by the colored background. The order changes from out-of-plane direction to in-plane direction for increasing Δ. For all regimes, the AFM ordering is present. Discussion see text.

Weiss field and $\Delta \gtrsim 0.3t$, the excited magnetic doublet $D_{1/2}$ starts to get populated the way $\langle S_0 \rangle$ is reduced and $\langle S_3 \rangle \approx 0$ as expected. But for quite small $\Delta < 0.3t$ the higher lying singlet S_3 starts to mix into the population. While $D_{1/2}$ and S_3 are nearly degenerate for small Δ (combined into $|J_{LS} = 1\rangle$ for $\Delta = 0$), the anisotropy of the kinetic energy slightly favors the singlet S_3. With increasing Δ, the levels split further, the population of S_3 is again reduced and the magnetism is only driven by the admixture of $D_{1/2}$ to the on-site wave function.

Regarding the cubic harmonics, Fig. 4.3 (c), the non-magnetic gray symbols nicely show how the TCF splits the orbitals. It lifts the xy-orbital resulting in a lower hole density $\langle xy \rangle$ while $\langle xz \rangle \approx \langle yz \rangle > 0.6$. In the magnetic regime, the depopulation of xy only appears for $\Delta \gtrsim 0.3t$. For small Δ, the xy-orbital is more populated than the others as already observed in Fig. 3.4 (b) and explained by the anisotropic hopping contributions.

The Kramers doublets in Fig. 4.3 (d) represent the one-particle eigenstates of SOC and TCF, see Sec. 2.1.4. For $\Delta = 0$, the doublets $B_\pm$ and $C_\pm$ are degenerate and the doublet $A_\pm$ is the ground state according to Fig. 2.11 (b). For increasing TCF, the Kramers $B_\pm$ and $C_\pm$ split and Kramers $B_\pm$ gains weight as expected by the atomic level structure and observed in the expectation values in Fig. 4.3 (d). The population reversion observed in the cubic harmonics for small small Δ is also visible in the Kramers doublets $B_\pm$ and $C_\pm$ as the Kramers doublets are directly connected to the orbitals, see Eq. (2.25).

Concerning the spectral densities in Fig. 4.4 each row has the same value of TCF $\Delta = 0.1t$, $0.4t$, $0.7t$, t while the columns show the spectra for the averaged superposition and resolved for each orbital separately. The spectra are given in the optimal orders. The characteristic arc at (π, π) resulting from the doubling of the unit cell is visible for all values of Δ. Further, the total spectra in the first column are quite similar for each Δ apart from a small shift within the uppermost bands. The density of the lowest band in the xy-orbital spectrum is reduced for increasing TCF illustrating the population decrease of the xy-orbital due to TCF. In return, the xz- and yz-orbitals loose weight in the band above the Fermi energy and gain it below. Additionally, the arc at (π, π) is shifted from the xy-orbital to the yz- and xz-orbitals showing that the latter participate now in the magnetism.

Increasing TCF for large SOC $\lambda = 1.67t$

For fixed $\lambda = 1.67t$, the system is in the LS-regime but shows no magnetic order, cf. Fig. 3.4. To investigate the transition from the limit of $\Delta = 0$ to the limit with $\lambda < \Delta$, as shown in Fig. 2.9 for the atomic limit, the TCF Δ is increased from 0 to $4t$. Although TCF is quite large, which could in principle force a spin-1 magnetism, VCA calculations with AFM S_x or AFM S_z Weiss fields revealed no magnetic order due to the large SOC. Nevertheless, the population shifts induced by TCF are investigated by calculating the expectation values of different states in the absence of magnetic Weiss fields, see Fig. 4.5. The expectation values are similar to those obtained in the absence of the Weiss field

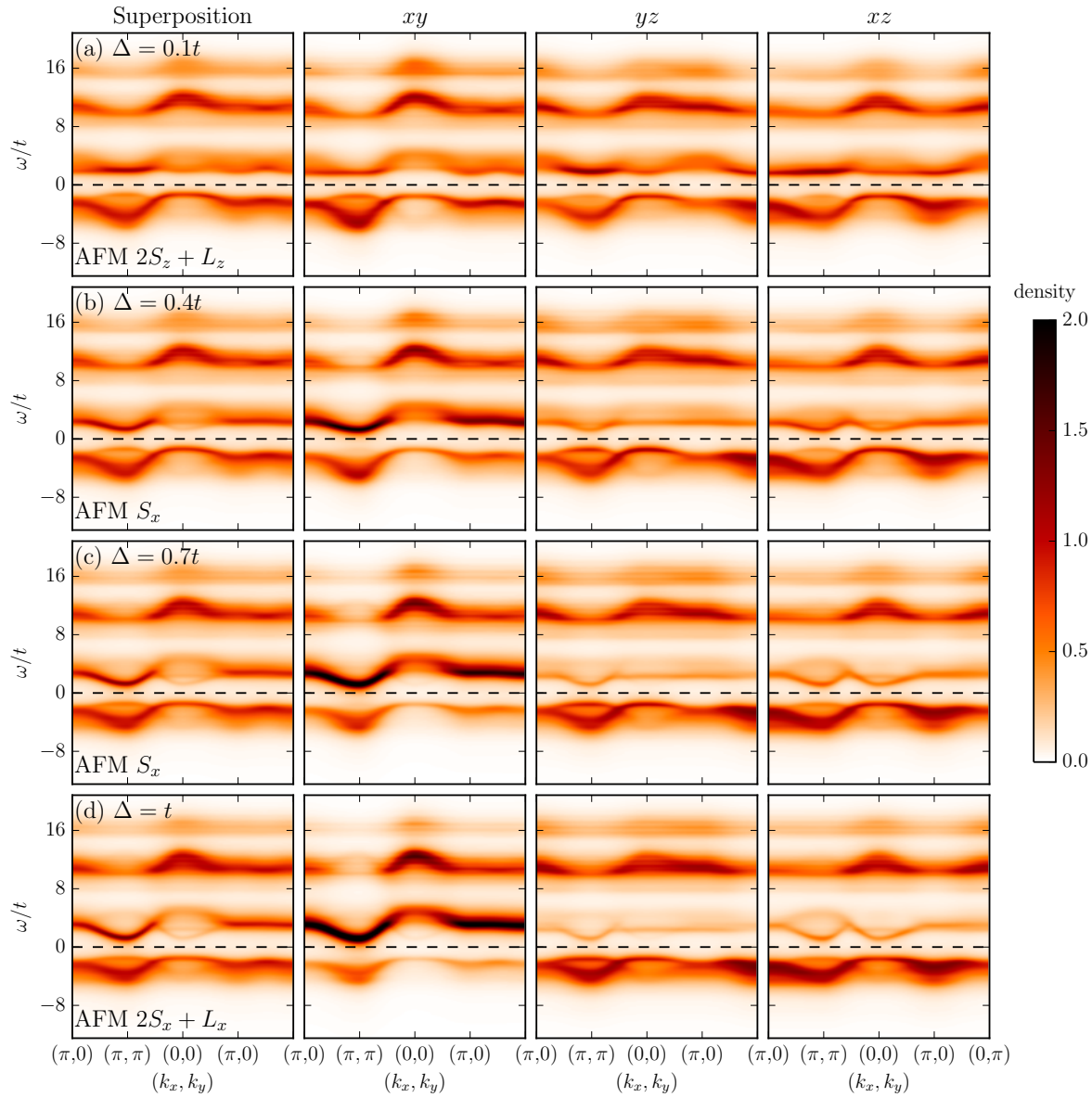

Figure 4.4: Spectral densities $A(\boldsymbol{k}, \omega)$ for fixed SOC $\lambda = 0.75t$ and four values of TCF (a) $\Delta = 0.1t$, (b) $\Delta = 0.4t$, (a) $\Delta = 0.7t$ and (d) $\Delta = t$ with $U = 12.5t$, $J_\mathrm{H} = 2.5t$ and $t = t_{xy} = t_{yz} = t_{xz} = 0.12\,\mathrm{eV}$ in the optimal order. Each row has the same value of TCF while the columns show the spectra for the averaged superposition and resolved for each orbital separately.

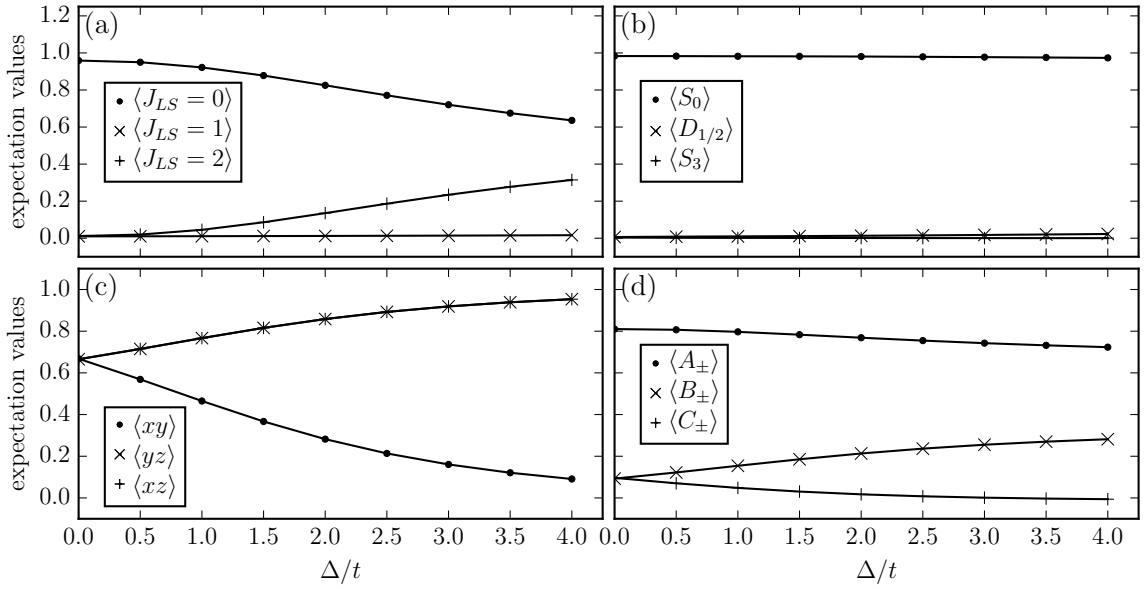

Figure 4.5: Expectation values for fixed SOC $\lambda = 1.67t$ over the TCF Δ with $U = 12.5t$, $J_{\mathrm{H}} = 2.5t$ and $t = t_{xy} = t_{yz} = t_{xz} = 0.12\,\mathrm{eV}$. The expectation values of (a) the J_{LS} states, (b) the one-site ED states, (c) the cubic harmonic orbitals and (d) the Kramers doublets are given. The system shows no magnetic order because of the large value of SOC. See text for further discussion.

for $\lambda = 0.75t$ in Fig. 4.3. However, due to the stronger TCF some features are better visible.

For $\Delta = 0$, the ground state is perfectly described by the $|J_{LS} = 0\rangle$ state with the $|J_{LS} = 1, 2\rangle$ states having no weight, see Fig. 4.5 (a). For increasing TCF, $\langle J_{LS} = 0\rangle$ strongly reduces and the $|J_{LS} = 2\rangle$ state becomes relevant showing that the description in terms of J_{LS} states breaks down as the LS-picture does not include any influence of the TCF. The singlet S_0, however, is a perfect description for the system as $\langle S_0\rangle \approx 1$ and $\langle D_{1/2}\rangle \approx \langle S_3\rangle \approx 0$, see Fig. 4.5 (b). As the levels incorporate the TCF splitting, the expectation values do not vary with increasing Δ.

Figure 4.5 (c) nicely shows how the TCF splits the orbitals. It lifts the xy-orbital which results in a lower population while $\langle xz\rangle \approx \langle yz\rangle > 0.6$. The two holes in the xz- and yz-orbitals build a spin-1 that in principle could order. However, VCA calculations with AFM S_x or AFM S_z Weiss fields revealed no magnetic order due to the large SOC. For $\Delta = 0$, the Kramers doublet $A_\pm$ in Fig. 4.5 (d) yields a good description of the ground state as $\langle A_\pm\rangle \approx 0.8$ according to the overlap $\langle J_{LS} = 0|A_+A_-\rangle \approx 0.816$ calculated in Sec. 2.1.4. The Kramers doublets $B_\pm$ and $C_\pm$ are degenerate with $\langle B_\pm\rangle \approx \langle C_\pm\rangle \approx 0.1$. For increasing TCF, the Kramers $B_\pm$ and $C_\pm$ split and Kramers $B_\pm$ gains weight as expected by the atomic level structure in Fig. 2.11 (b).

The population shift of the xy-orbital is also visible in the spectral densities in Fig. 4.6 and the density of states in Fig. 4.7. Both figures show the data for four values of $\Delta = 0$, t, $3t$, $4t$ in each row, the averaged superposition as well as the orbital resolved data in each column. The spectra of the averaged superposition in the first column are quite similar for each Δ apart from a small shift within the uppermost bands. However, the xy-orbital is severely affected by the TCF as the population in the lowest band vanishes almost completely. In return the xz- and yz-orbitals loose weight in the band above the Fermi energy and gain it below. This is also well visible in the density of states in Fig. 4.7.

4.3 Antiferromagnetic Order driven by TCF at intermediate SOC

Section 4.2 showed on the one hand, that TCF causes a reorientation of the spin direction in the magnetic regime if the magnetic regime is already present for $\Delta = 0$. On the other hand, if SOC is large, $\lambda = 1.67t$, and stabilizes a non-magnetic regime, even high TCF cannot force the magnetic order. Fixing SOC to an intermediate value $\lambda = 1.25t$ which is on the edge of the non-magnetic regime for $\Delta = 0$, TCF is able to drive the system into magnetic order, see Fig. 4.8.

For $\Delta = 0.5t$, the system is still PM. However, increasing TCF to $\Delta = 1.5t$ yields AFM $2S_x + L_x$ order with non-vanishing ordered moment $\langle 2S_x + L_x\rangle$. Even higher TCF $\Delta = 4.2t$ changes the order to AFM S_x. In between $\Delta = 0.5t$ and $\Delta = 1.5t$ the

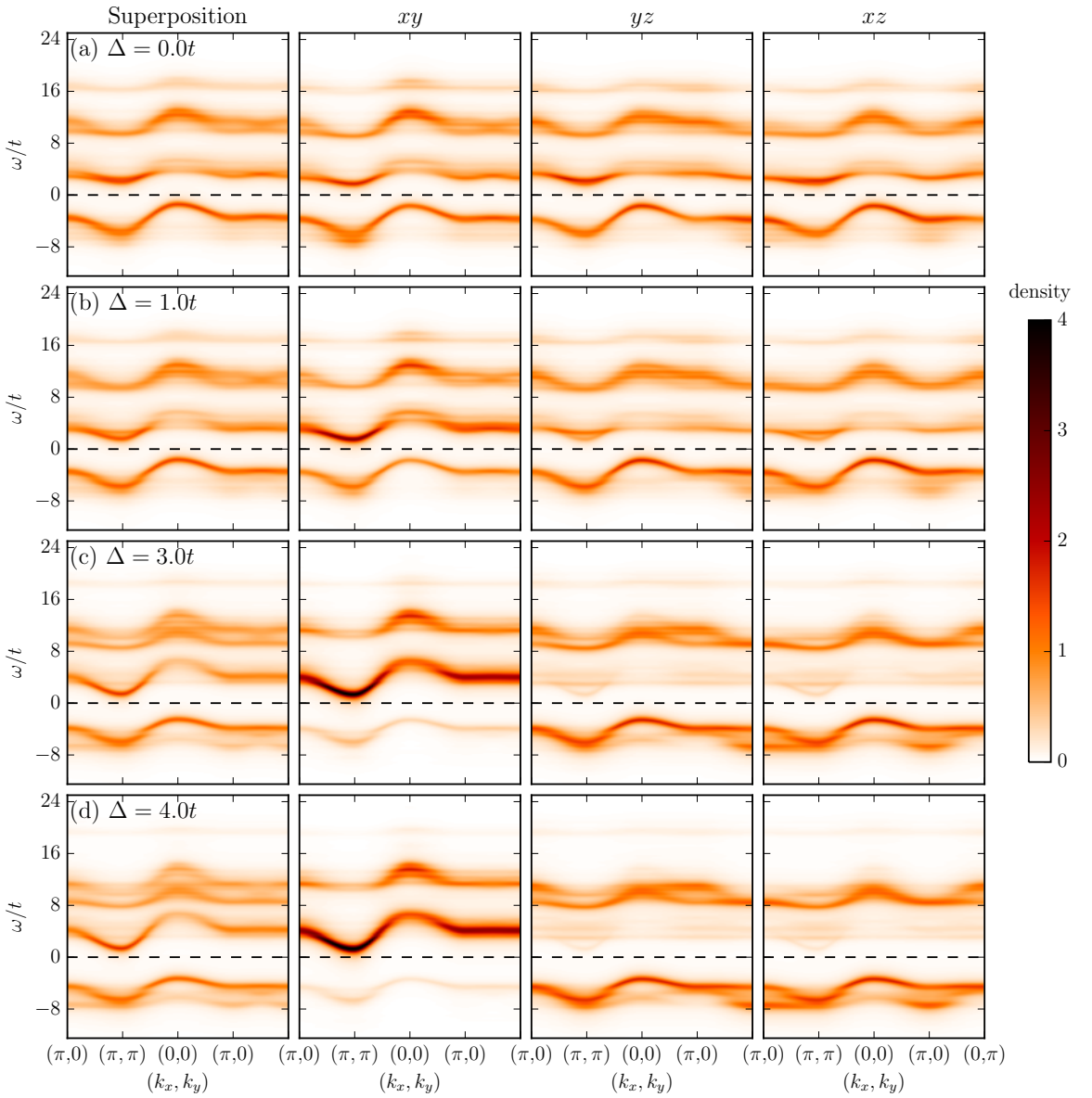

Figure 4.6: Spectral density $A(\boldsymbol{k}, \omega)$ for fixed SOC $\lambda = 1.67t$ and four values of the TCF (a) $\Delta = 0$, (b) $\Delta = t$, (c) $\Delta = 3t$ and (d) $\Delta = 4t$ with $U = 12.5t$, $J_\mathrm{H} = 2.5t$ and $t = t_{xy} = t_{yz} = t_{xz} = 0.12\,\mathrm{eV}$. Each row has the same value of TCF while the columns show the spectra for the averaged superposition and resolved for each orbital separately.

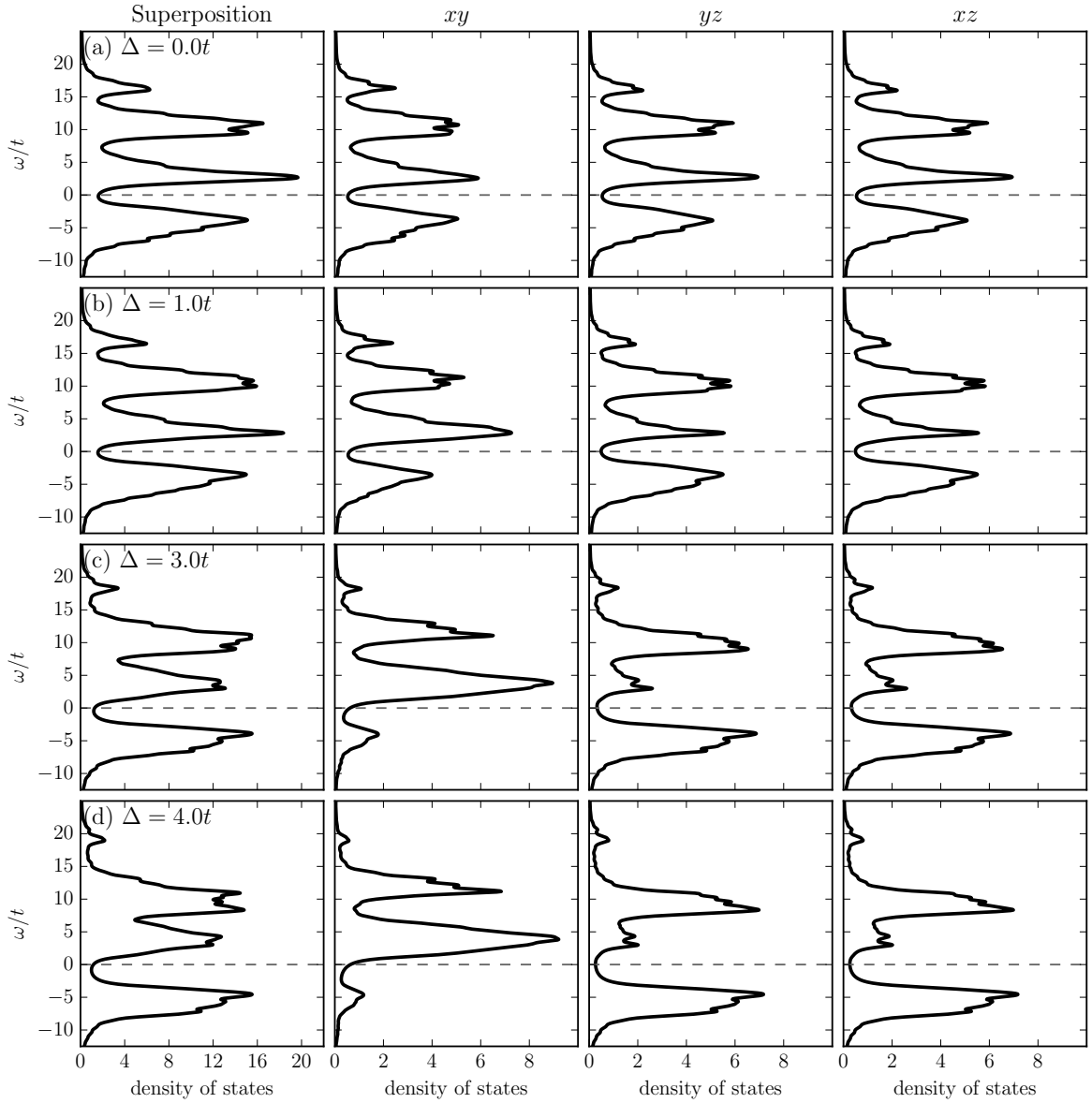

Figure 4.7: Density of states for fixed SOC $\lambda = 1.67t$ and four values of the TCF (a) $\Delta = 0$, (b) $\Delta = t$, (c) $\Delta = 3t$ and (d) $\Delta = 4t$ with $U = 12.5t$, $J_\mathrm{H} = 2.5t$ and $t = t_{xy} = t_{yz} = t_{xz} = 0.12\,\mathrm{eV}$. Each row has the same value of TCF while the columns show the densities of states for the averaged superposition and resolved for each orbital separately.

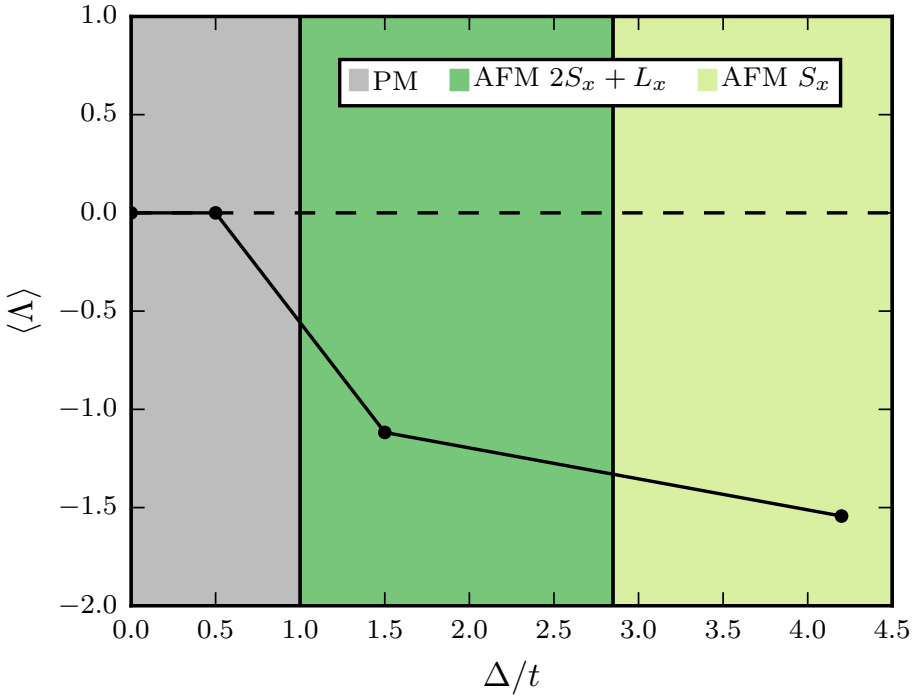

Figure 4.8: The ordered moment $\langle \Lambda \rangle$, $\Lambda = 2S_x + L_x,\ S_x$, in dependence on the TCF Δ for fixed SOC $\lambda = 1.25t$, $U = 12.5t$, $J_{\mathrm{H}} = 1.67t$, $t = t_{xy} = t_{yz} = t_{xz}$. In the absence of TCF, the system is in the PM regime. TCF drives the system into AFM order denoted by the colored background yielding a quantum critical point for $\Delta \approx t$.

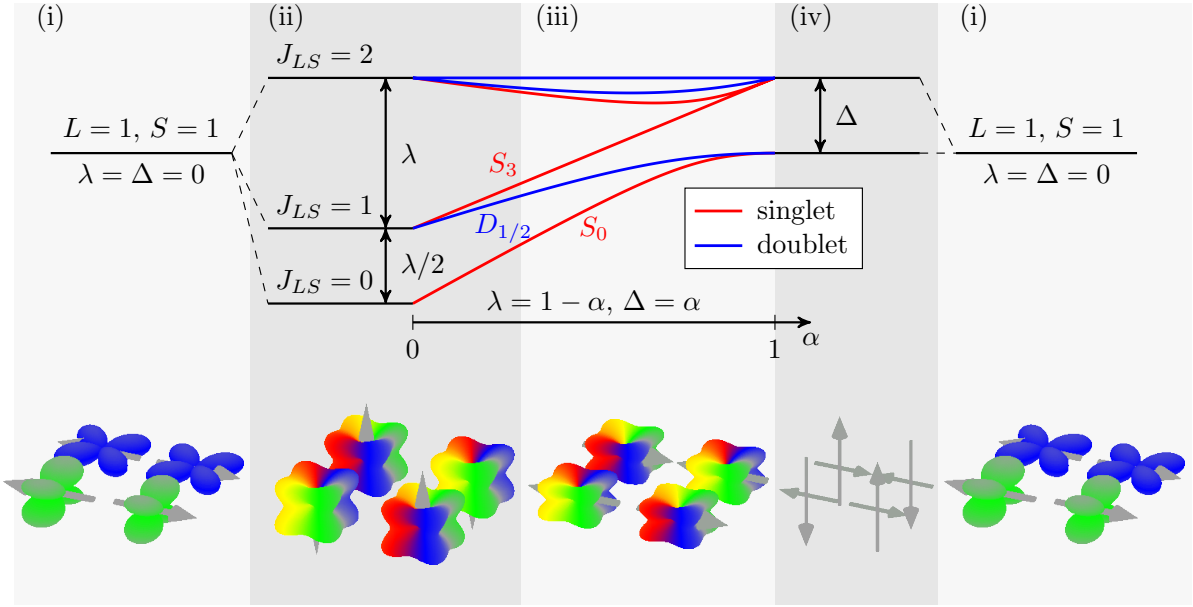

Figure 4.9: The interplay of SOC and TCF in the LS-limit reveals a rich atomic level structure and multiple magnetic and orbital orders which are given as cartoons. There are four different regimes (i)-(iv) each dominated by a certain ordering pattern. Discussion see text.

system undergoes a second order phase transition with a quantum critical point [60, 61]. As given by the atomic level structure in Fig. 2.9, the singlet S_0 and the doublet $D_{1/2}$ approach for increasing TCF and the reduced splitting enables the magnetism.

4.4 Summary: Interplay of SOC and TCF in the LS-Regime

Having investigated a wide range of λ/Δ we are able to connect the magnetic and orbital orderings with the atomic level structure in the LS-regime, see Fig. 4.9. There are four main parts depending on the relation $\alpha(\lambda, \Delta)$:

(i) If $J_\mathrm{H}/\lambda > 1$ and $J_\mathrm{H}/\Delta > 1$, the system is in the stripy S_x regime with stripy orbital pattern following the GKA rules. Corresponding plots are given in Fig. 3.3 and Fig. 4.1.

(ii) In the absence of TCF $\Delta = 0$ and for strong enough λ, the AFM S_z or AFM $S_z + L_z$ order is stabilized as investigated in Fig. 3.3. The spins are antiferromagnetically ordered and the orbitals follow a complex superposition depicted by the multicolored orbital in Fig. 4.9 (ii). This regime survives even small amounts of $\Delta/\lambda \approx 0.3$ as seen in Fig. 4.3.

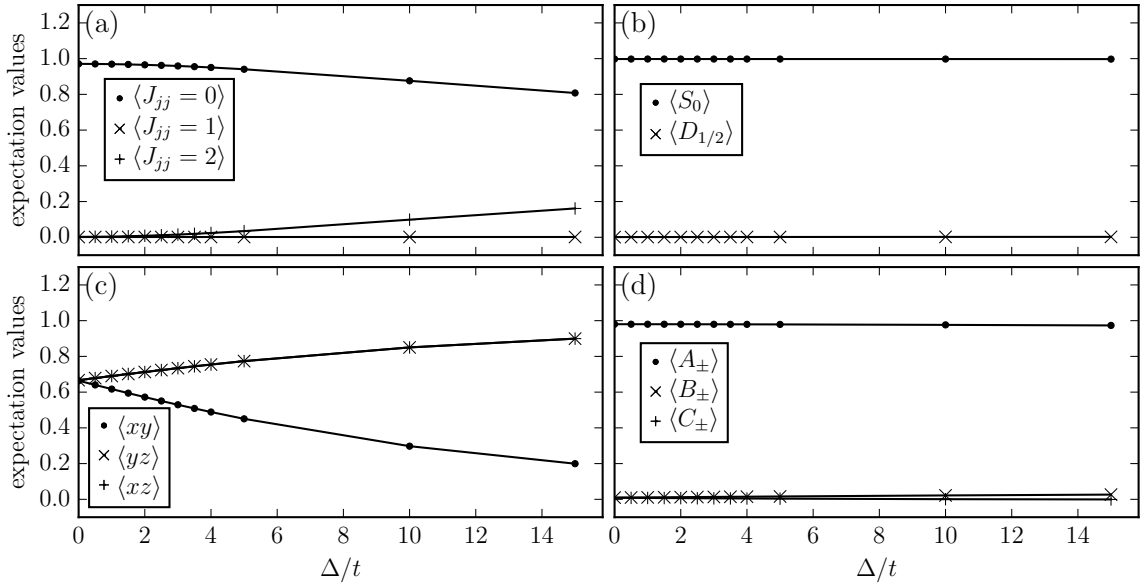

Figure 4.10: Expectation values of (a) the J_{jj} states, (b) the one-site ED states, (c) the cubic harmonic orbitals and (d) the Kramers doublets for $\lambda = 10t > J_\mathrm{H} = 2.5t$ over TCF Δ. We fix $U = 12.5t$ and $t = t_{xy} = t_{yz} = t_{xz} = 0.12\,\mathrm{eV}$.

(iii) As the value of TCF increases the ordering changes its direction to in-plane. The spins are always antiferromagnetically ordered but the orbital superposition changes depending on SOC and TCF, see Fig. 4.3 and Fig. 4.1. This regime lasts even for $\Delta > \lambda$ and turns into PM if J_H/λ gets too high, which will be discussed in Fig. 5.2 in Sec. 5.

(iv) Finally, the limit of $\lambda = 0$ and $\Delta \gg 0$ reveals an AFM $S_{x/y/z}$ regime where all spin directions coexist. A detailed discussion is given in context with Fig. 5.2 and Fig. 5.3 in Sec. 5.

4.5 jj-Limit with TCF

For the sake of completeness, the impact of the TCF on the jj-regime is investigated. Although there is no magnetic order in the jj-regime, cf. Fig. 3.15, the influence of TCF is observable in the band structure and the level population, see Fig. 4.10. The jj-regime's most remarkable feature is the large gap between the singlet $|J_{jj} = 0\rangle$ and the triplet $|J_{jj} = 1\rangle$ as shown in Fig. 2.10. When adding the TCF, the $|J_{jj} = 1, 2\rangle$ states split into subbands but do not affect the large gap.

We fix $\lambda = 10t > J_\mathrm{H} = 2.5t$ and vary Δ from 0 to $15t$ with $U = 12.5t$, $t = t_{xy} = t_{yz} = t_{xz}$ in Fig. 4.10. Figure 4.10 (a) shows that the J_{jj} states are quite robust against small values of Δ. However, the J_{jj} states fail to describe the system for large TCF and the

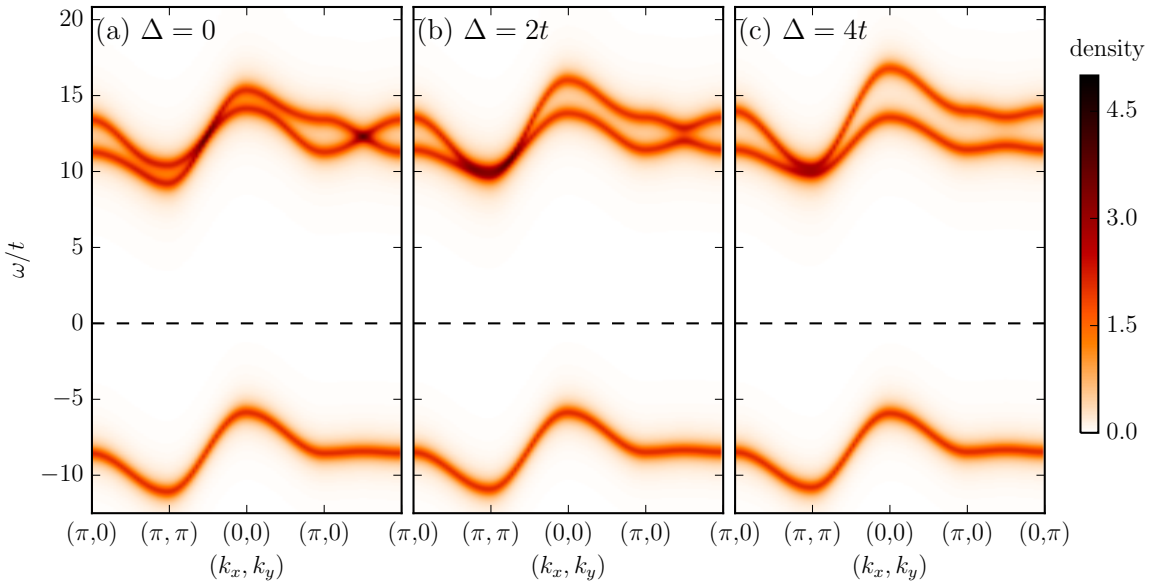

Figure 4.11: Spectral densities $A(\boldsymbol{k}, \omega)$ in the jj-regime with SOC $\lambda = 10t > J_{\mathrm{H}} = 2.5t$, $U = 12.5t$, $t = t_{xy} = t_{yz} = t_{xz} = 0.12\,\mathrm{eV}$ and TCF (a) $\Delta = 0$, (b) $\Delta = 2t$, (c) $\Delta = 4t$. The bands show the typical large splitting between the ground state and the excited states as characteristic for the jj-regime. The TCF influences the upper two bands by increasing the gap along the whole path except at (π, π).

$|J_{jj} = 2\rangle$ states start to admix. The J_{jj} states are derived from a Hamiltonian including J_{H} and λ and are not able to represent the level structure for non-negligible TCF. On the contrary, the one-site ED states in Fig. 4.10 (b) fit perfectly as they include the TCF completely. The system is fully described by the singlet S_0 and there is no contribution of the magnetic doublet $D_{1/2}$ as the gap is far too large. Figure 4.10 (c) shows once more the results which are characteristic for TCF, namely the population decrease in the xy-orbital. The Kramers doublets in Fig. 4.10 (d) provide a perfect description as they are the eigenstates of the Hamiltonian with Δ and λ. As $J_{\mathrm{H}} < \lambda$, it does not matter that these states ignore any Hund's coupling influence.

Figure 4.11 shows the spectral densities for $\Delta = 0,\ 2t,\ 4t$. The bands show the typical large splitting between the ground state and the excited states as characteristic for the jj-regime. The TCF influences the upper two bands by increasing the gap along the whole path except at (π, π).

5 Ca_2RuO_4

The low-temperature phase of Ca_2RuO_4 is characterized by a flattening of the RuO_6 octahedra [2, 17] and an AFM order with moments aligned parallel to the layers [7] as discussed in Sec. 2.2. The xy-orbital is lowered in energy and experiments [15] as well as numerical approaches [13, 14, 21, 44] indicate its nearly full occupation. The yz- and xz-orbitals are then both approximately half-filled and form a spin $S = 1$. Within this approach, SOC is only a correction rather than a dominant force [41, 78].

However, experiments in the AFM insulating state revealed a global maximum of the spin-wave dispersion found at the center of the first Brillouin zone which is in sharp contrast to a Heisenberg antiferromagnet [28] and can be explained by the excitonic picture presenting Ca_2RuO_4 as a possible candidate for excitonic magnetism [22, 67, 77]. Our results in Chap. 4 showed that the excitonic magnetism [31] arising from the admixture of the magnetic triplet to the non-magnetic singlet is realized for a certain range of TCF and SOC and coexists with orbital polarization.

In this chapter, we focus on model systems that are close to the experimentally measured parameters for Ca_2RuO_4 [22]. Small deviations from these data allow us to investigate the role of each parameter separately that is Coulomb interaction U, Hund's coupling J_H, TCF Δ and SOC λ. As the role of SOC in the magnetism is crucial, we first focus on a model with varying λ in Sec. 5.1. For simplicity, the hopping is given only by the dominant terms $t_{xy} = t_{yz} = t_{xz}$ and a next-nearest neighbor hopping for the xy-orbital. Furthermore, we investigate the influence of small deviations of U, J_H and λ from the experimentally measured values on the magnetic structure and the expectation values in Sec. 5.2. Using more hopping terms derived by DFT calculations and Wannier projections [5, 63], we are able to simulate lattice distortions and cants in the cluster.

5.1 Influence of Spin-Orbit Coupling on a simplified Model of Ca_2RuO_4

We investigate a model that is quite close to the real parameters of Ca_2RuO_4 but with a simpler hopping structure containing only $t = t_{xy} = t_{yz} = t_{xz} = 0.2\,\mathrm{eV}$ and a next-nearest neighbor hopping $t_{xy}^{NNN} = 0.5t$ for the xy-orbital, cf. Eq. (2.10). The Mott insulator is guaranteed as $U = 10t$ and $J_\mathrm{H} = 2.5t$ [69]. We fix $\Delta = 1.5t = 0.3\,\mathrm{eV}$, which is close to and even slightly larger than the experimental value of $\Delta \approx 0.25\,\mathrm{eV}$ [22]. Furthermore, SOC λ is varied from 0 to $\lambda \approx 1.6t$, which is still in the LS-regime with $J_\mathrm{H} > \lambda$, but allows us to study the emergence of magnetic order up to the non-magnetic regime.

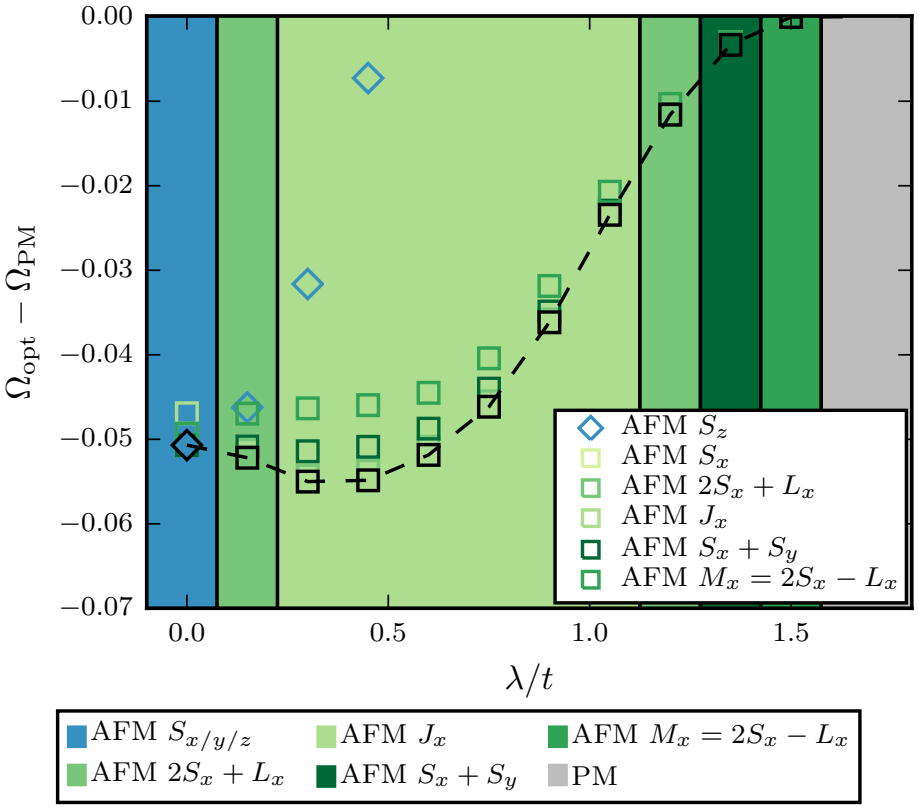

Figure 5.1: Comparison of the optimal values Ω_{opt} of the grand potential for several ordering patterns relative to the non-magnetic Ω_{PM} over SOC λ. The other parameters are fixed to $U = 10t$, $J_{\mathrm{H}} = 2.5t$, $t = t_{xy} = t_{xz} = t_{yz} = 0.2\,\mathrm{eV}$, $t_{xy}^{NNN} = 0.5t$ and $\Delta = 1.5t$. Background colors refer to the optimal ordering given by the lowest value of Ω_{opt}. Discussion see text.

As in the previous chapters, there are several competing orderings with and without orbital contribution and in- and out-of-plane orientation. Figure 5.1 shows the optimal values of the grand potential Ω_{opt} for these orderings relative to the non-magnetic Ω_{PM}. The order with the lowest value of Ω_{opt} wins and is denoted by the colored background. There are six different regimes whereof five are antiferromagnetically in-plane ordered for $\lambda \lesssim 1.5t$ and one is the PM regime for $\lambda > 1.5t$.

For $\lambda = 0$, the Ω_{opt} values are quite close to each other as there is no clear direction of the spins in the absence of SOC. We denote this regime by AFM $S_{x/y/z}$ as all directions are equal in accordance with ED calculations without SOC which find an AFM state with C- or G-type structure and different orbital configurations depending on the degree of flattening [10].

The direction preferred by SOC becomes evident for increasing λ. The AFM S_z order gets significantly worse and disappears already for $\lambda \approx 0.5t$. Still, the Ω_{opt} values of the in-plane orders stay close together and the optimal order changes from $2S_x + L_x$ to J_x which stays for a quite large range of $0.3t \lesssim \lambda \lesssim 1.05t$. As observed before, the orbital order has only a minor influence on Ω_{opt}. For stronger SOC, the optimal order changes again to $2S_x + L_x$ and $S_x + S_y$ and ends with M_x before becoming PM. This is quite interesting as it shows that the in-plane orientation is canted a bit against the previous x-direction. However, the Ω_{opt} are numerically so close together that it is impossible to speak of a real trend. We can only state that the dominant order is of AFM type with spins in-plane ordered and that the spin is the dominant contribution for symmetry breaking.

Figure 5.2 shows the expectation values of the J_{LS} states, the one-site ED states and the cubic harmonics. The gray symbols give the values without Weiss fields, the black symbols the values for the optimal order denoted by the colored background. For small $\lambda < 0.6t$, the J_{LS} states in Fig. 5.2 (a) contribute with comparable weights and cannot be used to characterize the ground state. The alternative picture of a spin $S = 1$ antiferromagnet with rather weak SOC is here appropriate. For $\lambda > 0.6t$, $\langle J_{LS} = 0\rangle$ dominates but not as clearly as it used to in the absence of TCF. In clear contrast to the case $\Delta = 0$, $\langle J_{LS} = 2\rangle$ is not close to zero and is in fact larger than $\langle J_{LS} = 1\rangle$. While the latter goes to zero with increasing λ, $\langle J_{LS} = 2\rangle$ persists into the PM regime and contributes to the orbital polarization. This is quite reasonable as the TCF destroys the J_{LS} level scheme in the atomic limit.

A better description for the populations is provided by the one-site ED states in Fig. 5.2 (b), which take Hund's coupling, SOC and TCF into account. As before, the small splitting of the three lowest states state for $\lambda \leq 0.6t$ makes a spin $S = 1$ antiferromagnet a more suitable ground state description than the singlet S_0 and the doublet $D_{1/2}$. However, for increasing λ, the singlet S_0 gains weight. In the magnetic regime the population is a bit reduced in favor of the doublet $D_{1/2}$ which shows that the latter admixes in the excitonic regime. The higher lying singlet S_3 is not affected at all and remains empty for all investigated SOC values. The J_{LS} states show a similar behavior as the magnetism is only driven by admixture of the magnetic triplet $|J_{LS} = 1\rangle$ to the

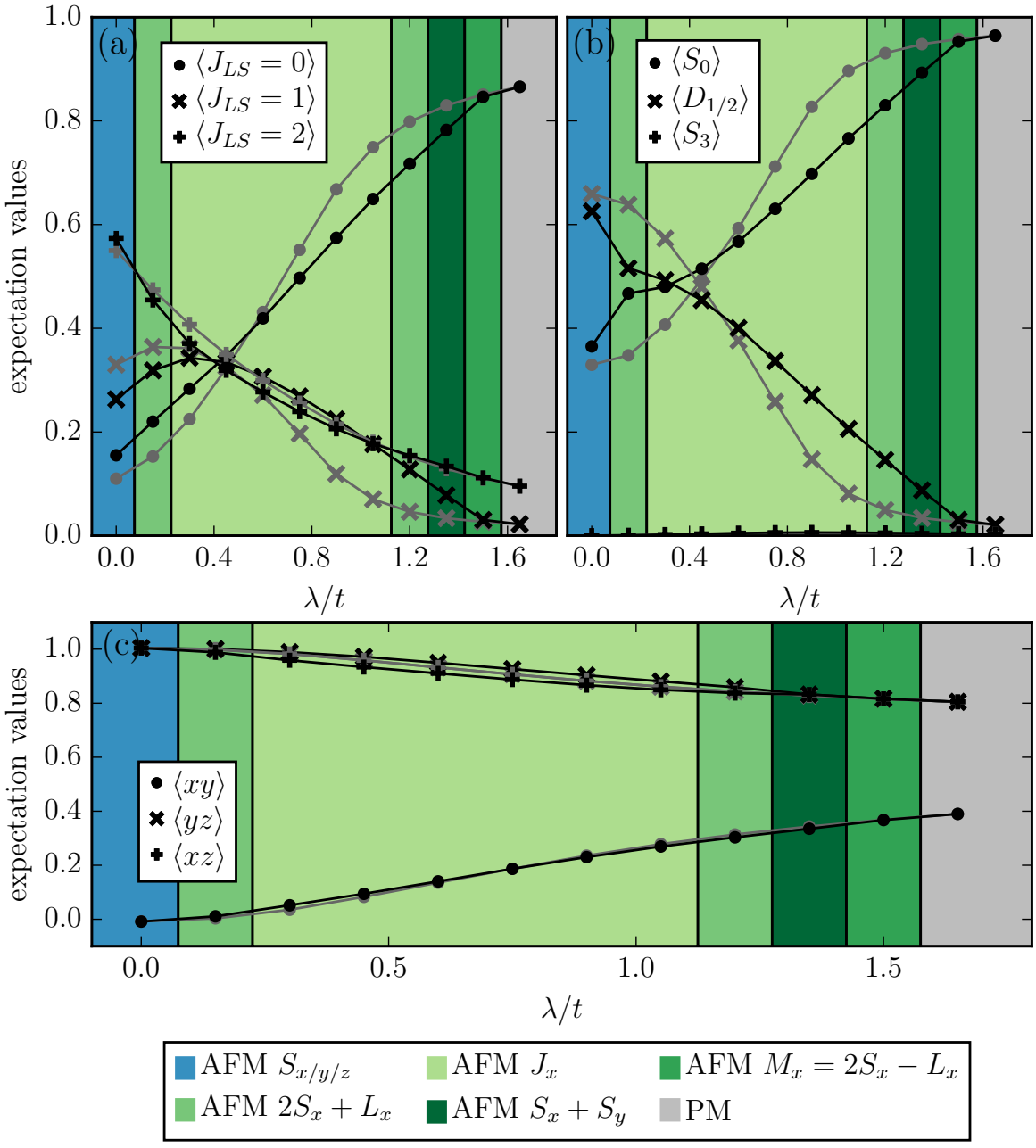

Figure 5.2: Expectation values for (a) the J_{LS} states, (b) the one-site ED states and (c) the cubic harmonic orbitals in the absence of Weiss fields (gray symbols) and in the ordered regime (black symbols). The background colors give the optimal order depending on SOC λ with fixed $U = 10t$, $J_{\mathrm{H}} = 2.5t$, $t = t_{xy} = t_{xz} = t_{yz} = 0.2\,\mathrm{eV}$, $t_{xy}^{NNN} = 0.5t$ and $\Delta = 1.5t$.

singlet $|J_{LS} = 0\rangle$. The population of the $|J_{LS} = 2\rangle$ state stays constant and it does not take part in the magnetism.

The population of the orbitals in Fig. 5.2 (c) shows that the xz- and yz-orbital are more populated than the xy-orbital, especially for small λ. This supports the existence of the spin-1 magnetism built by the two spins in xz and yz. When SOC increases, the splitting gets weaker as SOC mixes all orbitals and competes with TCF and orbital occupations become more equal.

The results obtained by the J_{LS} states and the one-site ED states support the explanation of excitonic magnetism. Even if $\langle J_{LS} = 2\rangle > 0$, the magnetism occurs by population shifts between the ground state singlet and the excited triplet or doublet. These observations indicate the coexistence of spin-1 and excitonic magnetism for intermediate SOC. However, a critical $\lambda \approx 1.6t$, which is in the order of $\Delta = 1.5t$, fully suppresses magnetism even though substantial orbital population $\langle xy\rangle \approx 0.4 < \langle xz\rangle \approx \langle yz\rangle \approx 0.8$ remains.

5.2 Parameter Variation around the most plausible Values

As we are interested in the interplay of hopping, Hund's coupling, Coulomb interaction, TCF and SOC, we investigate the impact of small parameter deviations on the magnetic order and the expectation values. In this way, we are able to determine the role of each parameter separately and to estimate how strong it influences the ground state.

To have an additional observable in hand we present the eigenvalues of the single-site density matrix, which can be calculated by VCA. The number and strength of the dominant eigenvalues gives further indications concerning the ground state. For reasons of clarity and comprehensibility, we only plot eigenvalues > 0.05.

First, we focus on a simplified model with parameters close to the experimental values [22]. Second, we use hopping amplitudes derived by DFT calculations [63] to observe their influence on the model. Next, we alter all other parameters to values determined from recent resonant inelastic x-ray scattering experiments [22] step by step. Finally, using the DFT derived hoppings and experimental data, the importance of SOC is once more investigated by reducing it to lower values and to one extremely high value.

All sets of parameters are given in Tab. 5.1. The models are labeled from 1-7 and e1-e8 for a better distinction. Table 5.1 also gives the obtained ground state order in the last column.

Models with simple Hopping (Models 1-7)

Starting with the models with simplified hopping, the expectation values and optimal regimes are shown in Fig. 5.3.

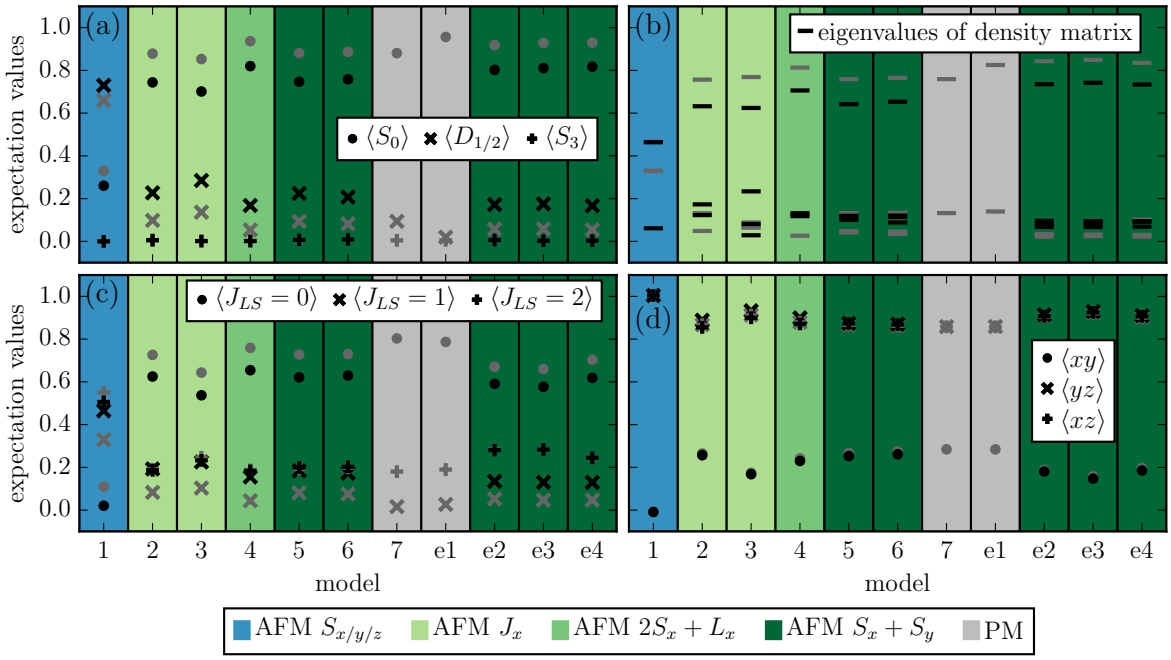

Figure 5.3: Overview of the expectation values of (a) the one-site ED states, (b) the dominant eigenvalues of the density matrix, (c) the J_{LS} states and (d) the orbitals for the investigated models whose parameters are given in Tab. 5.1. The gray and black symbols denote the values for vanishing Weiss field and in the optimal order, respectively, with the latter given by the colored background.

	$t = t_{xy}$	t_{yz}	t_{xz}	t_{xy}^{NNN}	$t_{xy,xz}$	U	J_{H}	λ	Δ	optimal order
1	0.2 eV	t	t	$0.5t$	0	$10t$	$2.5t$	0	$1.5t$	AFM $S_{x/y/z}$
2	0.2 eV	t	t	$0.5t$	0	$10t$	$2.5t$	t	$1.5t$	AFM J_x
3	0.2 eV	t	t	$0.5t$	0	$12.5t$	$2.5t$	$0.8t$	$1.5t$	AFM J_x
4	0.2 eV	t	t	$0.5t$	0	$12.5t$	$2.5t$	t	$1.5t$	AFM $2S_x + L_x$
5	0.2 eV	t	t	$0.5t$	$0.25t$	$10t$	$2.5t$	t	$1.5t$	AFM $S_x + S_y$
6	0.2 eV	t	t	$0.5t$	$0.5t$	$10t$	$2.5t$	t	$1.5t$	AFM $S_x + S_y$
7	0.2 eV	$0.5t$	$0.5t$	$0.5t$	$0.25t$	$10t$	$2.5t$	t	$1.5t$	PM
e1	0.1985 eV	$0.6831t$	$0.6831t$	$0.4952t$	$0.4680t$	$10t$	$2.5t$	t	$1.5t$	PM
e2	0.1985 eV	$0.6831t$	$0.6831t$	$0.4952t$	$0.4680t$	$10t$	$2.5t$	$0.6831t$	$1.5t$	AFM $S_x + S_y$
e3	0.1985 eV	$0.6831t$	$0.6831t$	$0.4952t$	$0.4680t$	$10t$	$1.713t$	$0.6831t$	$1.5t$	AFM $S_x + S_y$
e4	0.1985 eV	$0.6831t$	$0.6831t$	$0.4952t$	$0.4680t$	$10.0756t$	$1.7128t$	$0.6549t$	$1.2594t$	AFM $S_x + S_y$
e5	0.1985 eV	$0.6831t$	$0.6831t$	$0.4952t$	$0.4680t$	$10.0756t$	$1.7128t$	$0.32745t$	$1.2594t$	AFM $S_x + S_y$
e6	0.1985 eV	$0.6831t$	$0.6831t$	$0.4952t$	$0.4680t$	$10.0756t$	$1.7128t$	$0.163725t$	$1.2594t$	AFM $S_x + S_y$
e7	0.1985 eV	$0.6831t$	$0.6831t$	$0.4952t$	$0.4680t$	$10.0756t$	$1.7128t$	$0.06549t$	$1.2594t$	AFM $S_x + S_y$
e8	0.1985 eV	$0.6831t$	$0.6831t$	$0.4952t$	$0.4680t$	$10.0756t$	$1.7128t$	$1.3098t$	$1.2594t$	PM

Table 5.1: Parameters for models 1 to 7 and e1 to e8 including hopping t_i, Coulomb interaction U, Hund's coupling J_{H}, SOC λ and TCF Δ. Further, the obtained ground state order is given in the last column.

To begin with an unphysical but nevertheless important special case, model 1 represents the pure spin-1 scenario with SOC $\lambda = 0$. As already observed in Fig. 5.1 the orientation of the magnetic order cannot be determined as all orientations are possible giving rise to the so called AFM $S_{x/y/z}$ regime. As expected, the J_{LS} states and the one-site ED states cannot be used to characterize the ground state. Since TCF is here the dominant splitting, the xy-orbital is completely empty and the others are half-filled, i. e. $\langle yz\rangle = \langle xz\rangle = 1$. Concerning the eigenvalues of the density matrix, there are three eigenvalues with the same value of ≈ 0.33. This shows that the ground state is a spin $S = 1$. In the magnetic regime, there are two eigenvalues having ≈ 0.46 and one smaller one with ≈ 0.06 showing the breaking of local spin isotropy due to spontaneous symmetry breaking.

Model 2, which is already known from Fig. 5.2 at $\lambda = t$, is plotted for guidance and serves as a comparison for the other models. It orders AFM J_x with $\langle xy\rangle \ll \langle yz\rangle \approx \langle xz\rangle$, see Fig. 5.3 (d). The orbitals are robust against magnetic ordering. The J_{LS} states in Fig. 5.3 (c) cannot describe the ground state perfectly due to the TCF splitting. However, the excitonic magnetism is present as $|J_{LS} = 1\rangle$ mixes with $|J_{LS} = 0\rangle$. Although $\langle J_{LS} = 2\rangle \neq 0$ it does not take part in the magnetism. The description in terms of one-site ED singlets and doublets is quite good as the population is divided between them, see Fig. 5.3 (a). The higher lying singlet S_3 is not populated at all. The eigenvalues of the density matrix in Fig. 5.3 (b) show that there is one dominant eigenvalue and two other rather small contributions. In the ordered regime, the weight of the upper one is reduced and the two lowers are lifted a bit showing a population shift caused by the magnetic order.

As all models show quite similar results regarding their expectation values, we will only focus on the differences of the models 3-7.

For model 3 and 4, the Coulomb interaction U is increased whereas J_H stays constant giving $U/J_\mathrm{H} = 5$. Additionally, two values of λ, namely $\lambda = 0.8t$ and $\lambda = t$, are investigated which gives $U/\lambda = 15.625$ and 12.5 compared to $U/\lambda = 10$ in model 2. Model 3 shows AFM J_x order (like model 2) and model 4 has AFM $2S_x + L_x$ order. We conclude that the interplay of λ and U changes the type of order only a bit since both orderings are in-plane and quite similar as $J_x = S_x + L_x$. The relation U/λ has only a slight influence on the expectation values, especially the one-site ED states and the J_{LS} states are a bit shifted. In model 3 the large value of U/λ decreases the populations of the $|J_{LS} = 0\rangle$ state and the singlet S_0 compared to model 2. In model 4, $U/\lambda = 12.5$ is a bit higher than in model 2 with $U/\lambda = 10$ but the populations of the singlet S_0 are nevertheless slightly higher.

For the next two models 5 and 6, an additional hopping parameter $t_{xy,xz}$ is added to the parameters of model 2. It opens a hopping channel between neighboring xy- and xz-orbitals along the x-direction, see Eq. (2.10), and can be ascribed to a slight orthorhombic distortion in the AFM states motivated by DFT calculations [63]. We start with a small value of $t_{xy,xz} = 0.25t$ in model 5 and increase it to $t_{xy,xz} = 0.5t$ in model 6. Apart from a small change in the magnetic order to AFM $S_x + S_y$, this hopping

has no influence on the expectation values compared to model 2.

Finally, model 7 reduces the hoppings t_{yz} and t_{xz} to only $0.5t$ which is more realistic regarding the DFT calculations [63] resulting in a PM state. We suppose that the effective hopping strength is too weak compared to SOC to allow excitonic magnetism.

Models with DFT derived Hoppings (Model e1-e3)

Hopping terms derived from DFT and Wannier projections [5, 63] for Ca_2RuO_4 give more realistic hopping amplitudes than the idealized hopping we used in previous sections. They include cants and distortions in real space and provide specific values for each hopping. The Wannier hoppings are unique for each of the four Ru-atoms (Ru1 to Ru4) of the unit cell, cf. Fig. 2.14. We neglect hopping amplitudes $< 0.092\,\mathrm{eV}$.

The hopping t_{xy} between the xy-orbitals is the dominant hopping in the Ru1-Ru3 layer and serves as an energy scale. The hoppings t_{yz} and t_{xz} between the yz- and xz-orbitals are equal but only $\approx 2/3t_{xy}$. In the Ru2-Ru4 layer, the hopping $t_{xy,xz}$ between the xy- and the xz-orbital is $\approx 0.5t_{xy}$. Further, the next-nearest neighbor hopping t_{xy}^{NNN} is present for all Ru atoms. The DFT calculations finally lead to the hopping parameters

$$t_{xy} = t = 0.1985\,\mathrm{eV}, \quad t_{yz} = t_{xz} = 0.6831t, \quad t_{xy}^{NNN} = 0.4952t, \quad t_{xy,xz} = 0.4680t. \tag{5.1}$$

The one-particle spectral densities of the hoppings in Eq. (5.1) are given in Fig. 5.4. Here, we investigate the tight-binding limit with $U = J_\mathrm{H} = \lambda = \Delta = 0$ to see the rich dispersion structure caused by the complex hoppings. The dispersion of the yz-orbital in Fig. 5.4 stays one-dimensional whereas the xz hopping gets two-dimensional due to the hopping $t_{xy,xz}$.

We impose these hopping parameters on model 7 to get model e1. The system is still in the PM regime. Compared to model 7, e1 has a slightly increased effective hopping but it is not strong enough to compete against the singlet-triplet splitting. Regarding the J_{LS} states and the orbitals in Fig. 5.3 (c) and (d) there is nearly no distinction from model 7 visible. Surprisingly, the one-site ED states in Fig. 5.3 (a) and the eigenvalues of the density matrix are sensible to the hoppings. The population of the singlet S_0 increases while the other states are nearly empty.

To drive the system into the magnetic regime we reduce SOC to $\lambda = 0.6831t$ which is equivalent to the value of t_{xz} and t_{yz} and indeed find AFM $S_x + S_y$ order for model e2. In Fig. 5.3 (c) $\langle J_{LS} = 0\rangle \approx 2/3$ and is slightly reduced in the AFM regime. The $|J_{LS} = 1\rangle$ state is extremely low populated but essential for the magnetism as its population rises in the magnetic state. As observed in the models before, $\langle J_{LS} = 2\rangle > \langle J_{LS} = 1\rangle$ but the quintet population is constant with and without magnetic ordering and thus contributes only to orbital polarization and not to the magnetism. Regarding the one-site ED states the magnetism is enabled by the admixture of the doublet $D_{1/2}$ to the singlet S_0. There is one dominant density matrix eigenvalue and two lower ones, corresponding to these three involved states. Orbital occupations are robust with respect to magnetic order and the value of SOC, and orbital polarization is rather strong.

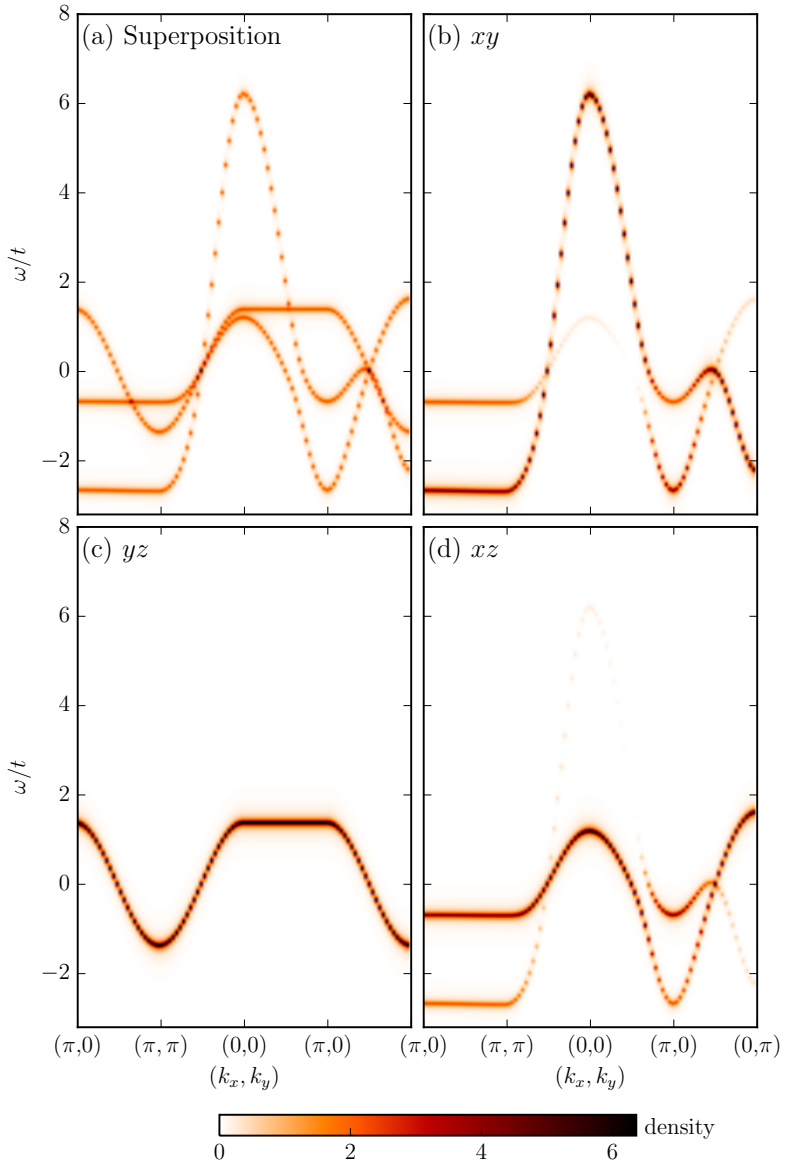

Figure 5.4: Spectral density $A(\boldsymbol{k}, \omega)$ for the hoppings given in Eq. (5.1) along the path of the Brillouin zone given in Fig. 2.5. (a) The averaged superposition and each orbital (b) xy, (c) yz and (d) xz are shown separately. The xy- and xz-orbitals show a two-dimensional dispersion as the hopping is allowed in two directions while yz is still one-dimensional.

For the next parameter set e3, we reduce J_{H} from $2.5t$ to $1.713t$ but keep $U = 10t$ fixed. This increases the relation from $U/J_{\mathrm{H}} = 4$ to $U/J_{\mathrm{H}} \approx 5.84$ which is a more realistic value for Ca_2RuO_4 [22, 69]. Compared to model e2, the expectation values are almost identical which shows that the adjustment of U/J_{H} is not highly important for the physics.

Models with DFT derived Hoppings and experimental Data (Model e4)

Gretarsson et al. recently observed a series of Ru intra-ionic transitions in Ca_2RuO_4 using Ru L_3-edge resonant inelastic x-ray scattering [22]. By measuring $J_{LS} = 0 \to 2$ spin-orbit excitations and Hund's rule driven $S = 1 \to 0$ spin state transitions, they were able to directly derive the values of SOC, TCF and Hund's rule interaction to $\lambda = 0.13\,\mathrm{eV}$, $\Delta = 0.25\,\mathrm{eV}$ and $J_{\mathrm{H}} = 0.34\,\mathrm{eV}$, respectively. Note that oxygen covalency reduces SOC from its free-ion value $\lambda \approx 0.16\,\mathrm{eV}$ to $\lambda \approx 0.13\,\mathrm{eV}$. As $U \approx 2\,\mathrm{eV}$ [22], we set our parameters with $t = t_{xy} = 0.1985\,\mathrm{eV}$ from Eq. (5.1) to

$$\begin{aligned} U &= 10.0756t \approx 2\,\mathrm{eV}, \quad J_{\mathrm{H}} = 1.7128t \approx 0.34\,\mathrm{eV}, \\ \lambda &= 0.6549t \approx 0.13\,\mathrm{eV}, \quad \Delta = 1.2594t \approx 0.25\,\mathrm{eV}. \end{aligned} \tag{5.2}$$

Within these parameters, the singlet-triplet splitting λ is smaller than the superexchange energy scale $4t^2/U \approx 80\,\mathrm{meV}$. With the TCF Δ, the emerging singlet-doublet splitting is further reduced in the atomic limit which could in principle enable excitonic magnetism.

Probing several Weiss fields, i.e. AFM S_z, S_x, $2S_x + L_x$, $S_x + S_y$, J_x and M_x, we find that the AFM $S_x + S_y$ is favored as in experiment [22]. The expectation values with and without Weiss field for the J_{LS} states, the one-site ED states, the density matrix eigenvalues and the cubic harmonics are given in Fig. 5.3, see model e4. The J_{LS} states as well as the one-site ED states show that the magnetism is driven by the admixture of the magnetic triplet $|J_{LS} = 1\rangle$ or the doublet $D_{1/2}$ to the singlet $|J_{LS} = 0\rangle$ and S_0, respectively. The higher quintet $|J_{LS} = 2\rangle$ and the singlet S_3 are not involved at all. Regarding the cubic harmonics, the xy-orbital is much less occupied than the two others as the TCF is large compared to SOC. In general, the model e4 is quite close to model e2 and e3 and the small corrections concerning the parameters have no substantial influence on the expectation values.

Figure 5.5 shows the spectral densities of model e4 (a) without Weiss fields and (b) in the optimal regime AFM $S_x + S_y$ along the path in the Brillouin zone given in Fig. 2.5. The lower band is clearly separated by a large band gap to the higher lying bands which confirms the Mott insulating state. The upper bands are rather blurred. In the magnetic regime the doubling of the unit cell is clearly visible by an arc around the (π, π) point. Also in the upper bands, there are some arc-like features around (π, π) and a splitting of the bands at $(\pi,0)$. Figure 5.5 (c) shows the spectral density of the model system with the parameters from Eq. (5.1) and Eq. (5.2) except that $\lambda = 0$ and thus represents

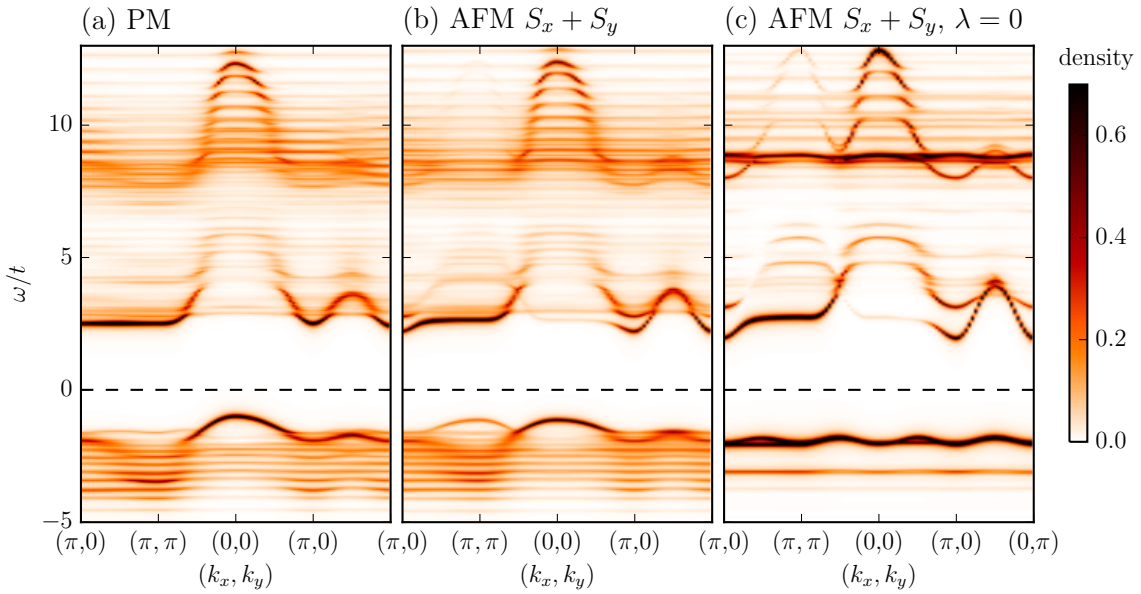

Figure 5.5: Spectral density $A(\boldsymbol{k}, \omega)$ of model e4 with the parameters of Eq. (5.1) and Eq. (5.2) (a) in the absence of Weiss fields and (b) in the optimal regime AFM $S_x + S_y$ and (c) with the same parameters except $\lambda = 0$ along the path in the Brillouin zone given in Fig. 2.5.

the pure spin-1 scenario. The system orders AFM $S_x + S_y$ like the model e4, showing that the presence of TCF is sufficient for the emergence of magnetism in line with the interpretation of angle-resolved photoemission-spectroscopy data [42, 69].

Figure 5.6 provides the density of states for (a) all orbitals and (b)-(d) each orbital separately. The density of states is given in the absence of the Weiss field as well as in the magnetic regime to better identify shifts in the bands. Even if there are small shifts the overall structure is unchanged.

Models with DFT derived Hoppings and experimental Data for different Values of SOC (Model e5-e8)

As observed in model 1-e3, the expectation values are mostly sensible to the values of SOC. Further, it showed that there is excitonic magnetism combined with a strong orbital polarization. In this section, we explore the range of SOC in which the excitonic magnetism still exists by setting the experimental value of SOC as a temporary scale $\lambda_0 = 0.6549t$. For $\lambda = \lambda_0$ (= model e4) the excitonic magnetism is present. Additionally, we have a deeper look into the models with $\lambda = 2\lambda_0$, $\lambda = 0.5\lambda_0$, $\lambda = 0.25\lambda_0$ and $\lambda = 0.1\lambda_0$, see Tab. 5.1 models e5-e8 for the parameters. The case $\lambda = 0$, see above, is the pure $S = 1$ limit with conventional spin rather than excitonic magnetism.

The expectation values of the models e5-e8 are presented in Fig. 5.7. The small offset

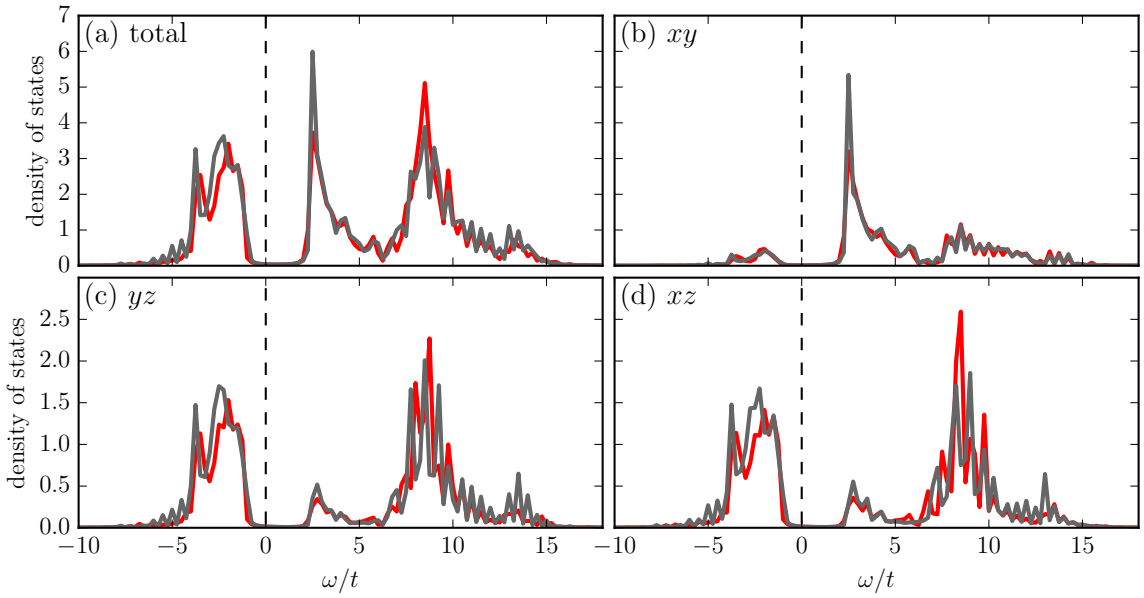

Figure 5.6: Density of states for the model e4 with the parameters of Eq. (5.1) and Eq. (5.2) in the absence of Weiss fields (gray lines) and in the optimal regime AFM $S_x + S_y$ (red lines). The density of states is given for (a) all orbitals and (b)-(d) each orbital separately. There are small shifts from the non-magnetic to the magnetic regime but the overall structure is unchanged.

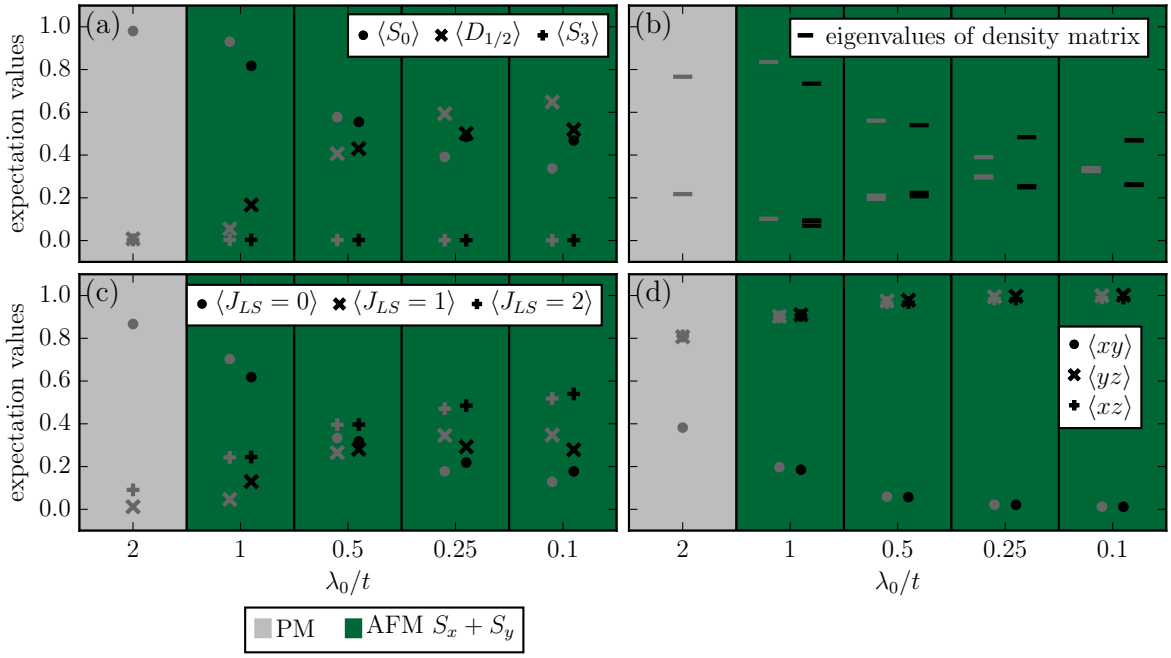

Figure 5.7: Several expectation values for the model systems based on the parameters in Eq. (5.1) and Eq. (5.2) with variation of SOC λ. (a) The one-site ED states, (b) the eigenvalues of the density matrix, (c) the J_{LS} states and (d) the cubic harmonic orbitals are given in the absence of Weiss fields (gray symbols) and in the optimal magnetic regime (black symbols) which is denoted by the colored background. We set $\lambda_0 = 0.6549t$ as a temporary scale. Except from $\lambda = 2\lambda_0$, which is non-magnetic, all systems order in AFM $S_x + S_y$.

between the magnetic and the non-magnetic values is introduced for a better readability. The background colors denote the optimal order. First, it is striking that all sets of parameters order in AFM $S_x + S_y$ except for $2\lambda_0$. In the latter case we find no magnetic ordering since SOC enlarges the energy gap between the non-magnetic singlet and the magnetic triplet and inhibits excitonic magnetism although orbital polarization is rather strong with $\langle xy\rangle \approx 0.4 < \langle xz\rangle \approx \langle yz\rangle \approx 0.6$.

Regarding the SOC values in the magnetic regime, the one-site ED states in Fig. 5.7 (a) give the well known singlet-doublet mixing for $\lambda = \lambda_0$. But already for $\lambda = 0.5\lambda_0$ the description starts to fail. The occupations of the singlet S_0 and the doublet $D_{1/2}$ are close to each other and the magnetic population is shifted only a bit compared to the non-magnetic. Decreasing λ even further reverses the population of the singlet S_0 and the doublet $D_{1/2}$ which shows that they cannot be used to characterize the ground state.

A similar behavior is visible in the J_{LS} states in Fig. 5.7 (c). For $\lambda = \lambda_0$ the population of the singlet $|J_{LS} = 0\rangle$ is dominant but only two thirds. The triplet $|J_{LS} = 1\rangle$ is very little populated but gains the weight that $|J_{LS} = 0\rangle$ looses in the magnetic state.

The quintet population $\langle J_{LS} = 2 \rangle \approx 0.2$ but is robust to the magnetic regime. These observations support the presence of excitonic magnetism. However, halving SOC immediately brings the LS-picture to a breakdown. All states are nearly equally populated and the population reverses for even smaller SOC. Due to the degeneracy for $\lambda = 0$ in the atomic limit, the states cannot be resolved any more. Hence, the concept of excitonic magnetism and the LS-scheme are only applicable for $\lambda \approx t_{xz}$.

The eigenvalues of the density matrix in Fig. 5.7 (b) behave accordingly to the other observations. For large SOC, there is one dominant eigenvalue representing the well occupied singlet state. For decreasing SOC several states start to mix into the ground state thus there are more dominant eigenvalues appearing. However, the differences between the non-magnetic values and the magnetic ones show, that there is a weight shift within the density matrix. For the non-magnetic values, the eigenvalues are closer together and split further apart in the magnetic regime.

Here, the occupation of the orbitals given in Fig. 5.7 (d) becomes important. The TCF is so strong compared to SOC that $\langle xy \rangle \approx 0$ already for $0.5\lambda_0$. This leads to the stable half-filling of the xz- and yz-orbitals where the two spins form a spin 1. The latter is able to order magnetically.

Our results concerning the one-site ED states and the J_{LS} states show that the excitonic magnetism applies when $\lambda \approx t_{xz}$. If SOC leaves this range, the expectation values no longer support the singlet-triplet excitonic model: For smaller $\lambda \lesssim 0.5t_{xz}$, we find spin-1 magnetism without excitonic character. Larger λ stabilizes a non-magnetic state. As far as Ca_2RuO_4 is concerned, our calculations on model e4 show that it falls into the excitonic regime despite its strong orbital polarization with nearly filled xy-orbital. This is supported by magnetic excitations obtained using ED [16] as they are found to closely match neutron-scattering data [28, 41], in particular showing the maximum at momentum (0,0). Therefore, Ca_2RuO_4 is well described by the coexistence of excitonic and spin-1 magnetism.

6 Summary and Outlook

The purpose of this thesis was to investigate the emergence of magnetism caused by the interplay of superexchange, SOC and TCF of t_{2g}^4 systems in general and particularly of Ca_2RuO_4 in the low-temperature phase. SOC causes the spin and orbital angular momentum to couple to a total momentum J with a non-magnetic singlet ground state $J = 0$ and a magnetic triplet $J = 1$ and quintet $J = 2$ in the atomic limit. However, if superexchange, involving the $J = 1$ and $J = 2$ states, is strong enough to compete with the singlet-triplet splitting, the on-site wave function becomes a superposition of the magnetic triplet and the non-magnetic singlet and acquires a magnetic moment that can order. This so called excitonic magnetism is likely to be realized in Ca_2RuO_4.

As the role of SOC in the magnetism is highly debated, we investigated the interplay of SOC and on-site interactions with and without TCF and its impact on the magnetic orderings. Using VCA, we studied the magnetism by applying fictitious Weiss fields with complex spin and orbital orderings. By comparing the grand potentials, we identified the optimal ordering depending on SOC and TCF. The populations of the atomic states and the hole densities allowed us to characterize the ground state of the lattice. Since the small cluster shows no order in the absence of Weiss fields, we were able to compare the non-magnetic and the magnetic expectation values and directly observe the impact of magnetism on the ground state. Figure 6.1 summarizes our results in a phase diagram.

In the absence of TCF, SOC and superexchange are the competing interactions. SOC stabilizes the non-magnetic $|J_{LS} = 0\rangle$ state while superexchange drives the magnetism by admixing the triplet to the singlet. For fixed hopping and on-site interactions, we found several regimes with spin and orbital order depending on the strength of SOC, see data points on the λ-axis in Fig. 6.1. For small SOC, there is a stripy S_x spin order with orbital order following the GKA rules, see the orange symbols. The xz-orbital is always half-filled, while xy and yz alternate along the y-direction orthogonal to the stripy spin order in x-direction. Finite SOC prefers the spin to lie in x- instead of z-direction.

For increasing SOC, the orbital polarization of GKA type is suppressed and the hole densities in the orbitals differ slightly $\langle xy\rangle > \langle yz\rangle \approx \langle xz\rangle$ due to the layered geometry, see the dark blue symbols. For intermediate SOC, the ordered regime is composed of several orbital and AFM spin patterns where the spin ordering in z-direction is the crucial step as the grand potentials are almost equal for orders containing orbital contributions. The magnetic moment is present due to the admixture of the magnetic triplet $|J_{LS} = 1\rangle$ to the non-magnetic singlet $|J_{LS} = 0\rangle$ supporting the theory of excitonic magnetism. The quintet $|J_{LS} = 2\rangle$ is not affected by the magnetism and always nearly unpopulated.

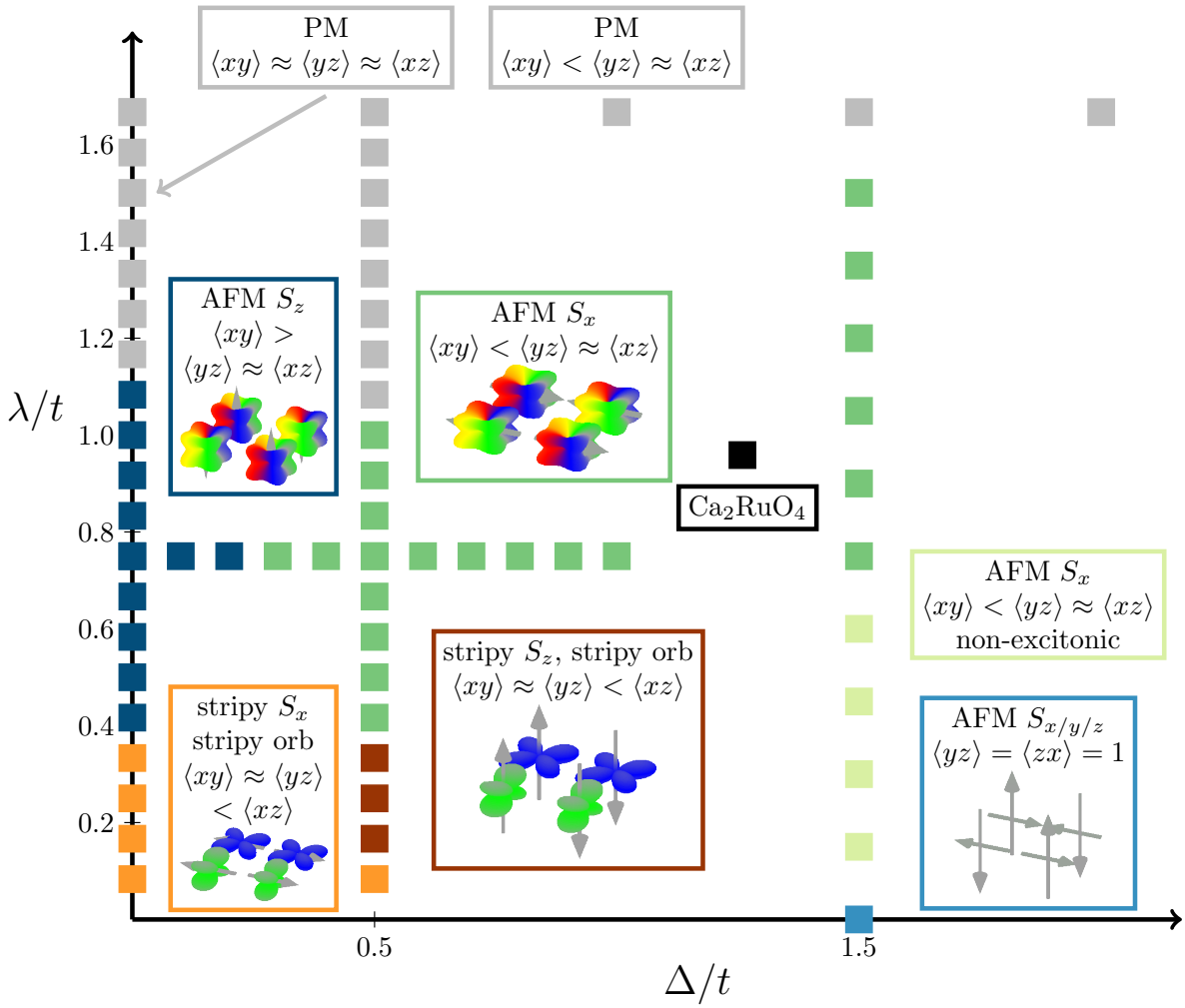

Figure 6.1: Phase diagram of TCF Δ and SOC λ derived from our results in Chap. 3, Chap. 4 and Chap. 5. The spin (small arrows) and orbital order (cartoon orbitals) as well as the hole densities are shown in each regime. For small Δ and λ the orange and red regimes have stripy spin and orbital pattern with the orbital occupation following the GKA rules. For $\Delta = 0$ and intermediate SOC, the excitonic regime (dark blue) with AFM S_z order and orbital polarization in favor of xy arises. Stronger SOC induces a PM phase with suppressed orbital polarization (gray). For $\lambda = 0$ and intermediate TCF $\Delta = 1.5t$, there is a spin-1 magnetism with AFM $S_{x/y/z}$ order and full orbital polarization (light blue). For intermediate Δ and intermediate SOC, the AFM order changes to S_x and orbital polarization favors xz and yz is according to the lifting of xy by TCF (dark green). The light green regime for $\Delta = 1.5t$ denotes AFM S_x order where the excitonic magnetism is not present. For high SOC, the system is in the PM phase (gray) with orbital polarization depending on TCF.

Increasing SOC even further drives the system into the PM phase, see the gray symbols. As SOC suppresses the orbital polarization, the impact of the layered geometry is likewise suppressed and $\langle xy\rangle \approx \langle yz\rangle \approx \langle xz\rangle$. In the strongly coupled regime, $\lambda > J_{\mathrm{H}}$, the PM phase is still present but better describable in terms of the J_{jj} states with a doubly occupied $J = 1/2$ state.

The characteristic hopping anisotropy for t_{2g} orbitals is responsible for the stripy order in the small SOC regime. Investigations of a more isotropic hopping model showed rather slight impact on the excitonic regime except by extending the magnetic regimes a bit. The extension can be explained by the increase of the total kinetic energy and therefore supports excitonic magnetism even for larger SOC. However, the difference in the orbital populations $\langle xy\rangle > \langle yz\rangle \approx \langle xz\rangle$ is in fact not reduced but slightly increased.

Taking TCF into account, the competition between SOC and TCF becomes important. As TCF lifts the xy-orbital in energy in hole notation, the absence of SOC, $\lambda = 0$, results in the full orbital polarization with $\langle xy\rangle = 0$ and $\langle yz\rangle = \langle xz\rangle = 1$. The spins in the yz- and xz-orbital form a spin $S = 1$ that orders in AFM $S_{x/y/z}$ direction, see the light blue symbol for $\Delta = 1.5t$.

Focusing first on small TCF $\Delta = 0.5t$, the stripy phase is again present for small SOC but with S_z rather than S_x spin orientation for increasing SOC, see the red symbols. Unaffected by small TCF, the orbital polarization follows the GKA rules. Increasing SOC leads to various AFM spin and orbital orders while TCF causes a reorientation of the spins from z- to x-direction, see the dark green symbols. Further, there is a strong orbital polarization with $\langle xy\rangle < \langle xz\rangle \approx \langle yz\rangle$ due to the lifting of the xy-orbital by TCF. However, the admixture of the triplet $|J_{LS} = 1\rangle$ and the doublet $D_{1/2}$ to the non-magnetic singlet $|J_{LS} = 0\rangle$ or S_0 is present showing the coexistence of excitonic magnetism and strong orbital polarization for intermediate SOC and TCF. The $|J_{LS} = 2\rangle$ states carry finite weight and contribute thus to orbital polarization but are not involved in the magnetic ordering. Larger SOC inhibits the magnetic order and causes a PM phase, see the gray symbols. The hole density $\langle xy\rangle$ increases with SOC but remains low and maintains the orbital polarization $\langle xy\rangle < \langle xz\rangle \approx \langle yz\rangle$.

The regimes change somewhat for stronger TCF $\Delta = 1.5t$. Stronger TCF suppresses the stripy regime even for small SOC due to the strong orbital polarization. AFM order with spins pointing along the x-direction is present, see the light green symbols. We denote this as the non-excitonic regime as the ground state and the magnetic ordering cannot be characterized in terms of singlets and doublets. When SOC increases, the excitonic regime reemerges and coexists with the strong orbital polarization until a critical but moderate SOC inhibits any magnetic order. However, the orbital polarization is still present in the PM regime indicating a considerable role of SOC even for stronger TCF.

For large SOC $\lambda = 1.67t$ the system is robust in its PM state and even strong TCF and the orbital polarization are not able to yield an ordered state. However, if SOC is

on the edge of the PM regime, $\lambda = 1.25t$, TCF is able to drive the system into the AFM ordered regime showing a quantum critical point.

The low-temperature phase of Ca_2RuO_4 is characterized by the flattening of the RuO_6 octahedra. This TCF causes the xy-orbital to be lowered in energy and leads to a strong orbital polarization where the xz- and the yz-orbitals are both approximately half-filled. Our calculations for Ca_2RuO_4 based on DFT derived hoppings and experimental data showed that Ca_2RuO_4 is in the excitonic AFM $S_x + S_y$ ordered regime with strong orbital polarization, see the black symbol in Fig. 6.1. The excitonic magnetism is only present for moderate SOC $\lambda \approx t_{xz}$. Smaller SOC yields spin-1 magnetism without excitonic character and stronger SOC stabilizes the PM phase.

In summary, our results show that the interplay of SOC and TCF yields a rich phase diagram concerning spin and orbital orders of which some show excitonic character. In the pure spin-1 scenario, $\lambda = 0$, it shows that TCF is sufficient for the emergence of magnetism. However, the magnetism is strongly influenced by SOC even in the orbitally polarized regime showing excitonic magnetism. Moreover, the loss of AFM order at large SOC indicates a considerable role of SOC.

We conclude that the spin-1 and the singlet-triplet excitonic magnetism coexist in the regime of comparable TCF and SOC. The magnetic order only affects the states with total angular momentum $J_{LS} = 0, 1$. The $J_{LS} = 2$ states carry finite weight and contribute thus to orbital polarization but are not involved in the magnetic ordering. This explains why magnetic excitations, including the amplitude Higgs mode, show singlet-triplet physics.

An extension of our research is possible in many ways. Having worked out that the excitonic magnetism is present for intermediate SOC and TCF in t_{2g}^4 systems, other materials like the honeycomb Li_2RuO_3 [48] and $Ag_3LiRu_2O_6$ [38] can be investigated in terms of this excitonic character since they were found to show excitations of the low-lying triplet acquiring nontrivial band topology in a magnetic field [3]. Further, VCA is also applicable to finite-temperature systems where one could observe temperature-depending phase transitions and their impact on the excitonic magnetism.

Bibliography

[1] A. Akbari and G. Khaliullin. Magnetic excitations in a spin-orbit-coupled d^4 Mott insulator on the square lattice. *Phys. Rev. B*, **90**:035137, Jul 2014.

[2] C. S. Alexander, G. Cao, V. Dobrosavljevic, S. McCall, J. E. Crow, E. Lochner, and R. P. Guertin. Destruction of the Mott insulating ground state of Ca_2RuO_4 by a structural transition. *Phys. Rev. B*, **60**:R8422–R8425, Sep 1999.

[3] P. S. Anisimov, F. Aust, G. Khaliullin, and M. Daghofer. Nontrivial Triplon Topology and Triplon Liquid in Kitaev-Heisenberg-type Excitonic Magnets. *Phys. Rev. Lett.*, **122**:177201, Apr 2019.

[4] M. Balzer and M. Potthoff. Variational cluster approach to ferromagnetism in infinite dimensions and in one-dimensional chains. *Phys. Rev. B*, **82**:174441, Nov 2010.

[5] J. Bertinshaw, N. Gurung, P. Jorba, H. Liu, M. Schmid, D. T. Mantadakis, M. Daghofer, M. Krautloher, A. Jain, G. H. Ryu, O. Fabelo, P. Hansmann, G. Khaliullin, C. Pfleiderer, B. Keimer, and B. J. Kim. Unique Crystal Structure of Ca_2RuO_4 in the Current Stabilized Semimetallic State. *Phys. Rev. Lett.*, **123**:137204, Sep 2019.

[6] J. Bertinshaw, Y. Kim, G. Khaliullin, and B. Kim. Square Lattice Iridates. *Annual Review of Condensed Matter Physics*, **10**:315–336, 2019.

[7] M. Braden, G. André, S. Nakatsuji, and Y. Maeno. Crystal and magnetic structure of Ca_2RuO_4: Magnetoelastic coupling and the metal-insulator transition. *Phys. Rev. B*, **58**:847–861, Jul 1998.

[8] J. Chaloupka, G. Jackeli, and G. Khaliullin. Kitaev-Heisenberg Model on a Honeycomb Lattice: Possible Exotic Phases in Iridium Oxides A_2IrO_3. *Phys. Rev. Lett.*, **105**:027204, Jul 2010.

[9] M. K. Crawford, M. A. Subramanian, R. L. Harlow, J. A. Fernandez-Baca, Z. R. Wang, and D. C. Johnston. Structural and magnetic studies of Sr_2IrO_4. *Phys. Rev. B*, **49**:9198–9201, Apr 1994.

[10] M. Cuoco, F. Forte, and C. Noce. Interplay of Coulomb interactions and c-axis octahedra distortions in single-layer ruthenates. *Phys. Rev. B*, **74**:195124, Nov 2006.

[11] M. Cuoco, F. Forte, and C. Noce. Probing spin-orbital-lattice correlations in $4d^4$ systems. *Phys. Rev. B*, **73**:094428, Mar 2006.

[12] C. Dahnken, M. Aichhorn, W. Hanke, E. Arrigoni, and M. Potthoff. Variational cluster approach to spontaneous symmetry breaking: The itinerant antiferromagnet in two dimensions. *Phys. Rev. B*, **70**:245110, Dec 2004.

[13] Z. Fang and K. Terakura. Magnetic phase diagram of $Ca_{2-x}Sr_xRuO_4$ governed by structural distortions. *Phys. Rev. B*, **64**:020509, Jun 2001.

[14] Z. Fang, N. Nagaosa, and K. Terakura. Orbital-dependent phase control in $Ca_{2-x}Sr_xRuO_4$ ($0 \lesssim x \lesssim 0.5$). *Phys. Rev. B*, **69**:045116, Jan 2004.

[15] C. G. Fatuzzo, M. Dantz, S. Fatale, P. Olalde-Velasco, N. E. Shaik, B. Dalla Piazza, S. Toth, J. Pelliciari, R. Fittipaldi, A. Vecchione, N. Kikugawa, J. S. Brooks, H. M. Rønnow, M. Grioni, C. Rüegg, T. Schmitt, and J. Chang. Spin-orbit-induced orbital excitations in Sr_2RuO_4 and Ca_2RuO_4: A resonant inelastic x-ray scattering study. *Phys. Rev. B*, **91**:155104, Apr 2015.

[16] T. Feldmaier, P. Strobel, M. Schmid, P. Hansmann, and M. Daghofer. Excitonic Magnetism at the intersection of Spin-orbit coupling and crystal-field splitting. arXiv:1910.13977, Oct 2019.

[17] O. Friedt, M. Braden, G. André, P. Adelmann, S. Nakatsuji, and Y. Maeno. Structural and magnetic aspects of the metal-insulator transition in $Ca_{2-x}Sr_xRuO_4$. *Phys. Rev. B*, **63**:174432, Apr 2001.

[18] S. Fuchs, T. Dey, G. Aslan-Cansever, A. Maljuk, S. Wurmehl, B. Büchner, and V. Kataev. Unraveling the Nature of Magnetism of the $5d^4$ Double Perovskite Ba_2YIrO_6. *Phys. Rev. Lett.*, **120**:237204, Jun 2018.

[19] A. Georges, L. d. Medici, and J. Mravlje. Strong Correlations from Hund's Coupling. *Annual Review of Condensed Matter Physics*, **4**:137–178, 2013.

[20] T. Giamarchi, C. Rüegg, and O. Tchernyshyov. Bose-Einstein condensation in magnetic insulators. *Nature Physics*, **4**:198–204, 2008.

[21] E. Gorelov, M. Karolak, T. O. Wehling, F. Lechermann, A. I. Lichtenstein, and E. Pavarini. Nature of the Mott Transition in Ca_2RuO_4. *Phys. Rev. Lett.*, **104**:226401, Jun 2010.

[22] H. Gretarsson, H. Suzuki, H. Kim, K. Ueda, M. Krautloher, B. J. Kim, H. Yavaş, G. Khaliullin, and B. Keimer. Observation of spin-orbit excitations and Hund's multiplets in Ca_2RuO_4. *Phys. Rev. B*, **100**:045123, Jul 2019.

[23] C. Gros and R. Valentí. Cluster expansion for the self-energy: A simple many-body method for interpreting the photoemission spectra of correlated Fermi systems. *Phys. Rev. B*, **48**:418–425, Jul 1993.

[24] T. Hotta and E. Dagotto. Prediction of Orbital Ordering in Single-Layered Ruthenates. *Phys. Rev. Lett.*, **88**:017201, Dec 2001.

[25] J. Hubbard. Electron Correlations in Narrow Energy Bands. *Proceedings of the Royal Society of London A: Mathematical, Physical and Engineering Sciences*, **276**:238–257, 1963.

[26] M. Imada, A. Fujimori, and Y. Tokura. Metal-insulator transitions. *Rev. Mod. Phys.*, **70**:1039–1263, Oct 1998.

[27] G. Jackeli and G. Khaliullin. Mott Insulators in the Strong Spin-Orbit Coupling Limit: From Heisenberg to a Quantum Compass and Kitaev Models. *Phys. Rev. Lett.*, **102**:017205, Jan 2009.

[28] A. Jain, M. Krautloher, J. Porras, G. H. Ryu, D. P. Chen, D. L. Abernathy, J. T. Park, A. Ivanov, J. Chaloupka, G. Khaliullin, B. Keimer, and B. J. Kim. Higgs mode and its decay in a two-dimensional antiferromagnet. *Nature Physics*, **13**:633, Mar 2017.

[29] N. Kaushal, J. Herbrych, A. Nocera, G. Alvarez, A. Moreo, F. A. Reboredo, and E. Dagotto. Density matrix renormalization group study of a three-orbital Hubbard model with spin-orbit coupling in one dimension. *Phys. Rev. B*, **96**:155111, Oct 2017.

[30] G. Khaliullin. Orbital Order and Fluctuations in Mott Insulators. *Progress of Theoretical Physics Supplement*, **160**:155–202, Jun 2005.

[31] G. Khaliullin. Excitonic Magnetism in Van Vleck–type d^4 Mott Insulators. *Phys. Rev. Lett.*, **111**:197201, Nov 2013.

[32] D. I. Khomskii. *Transition Metal Compounds*. Cambridge University Press, 2014.

[33] B. J. Kim, H. Jin, S. J. Moon, J.-Y. Kim, B.-G. Park, C. S. Leem, J. Yu, T. W. Noh, C. Kim, S.-J. Oh, J.-H. Park, V. Durairaj, G. Cao, and E. Rotenberg. Novel $J_{\text{eff}} = 1/2$ Mott State Induced by Relativistic Spin-Orbit Coupling in Sr_2IrO_4. *Phys. Rev. Lett.*, **101**:076402, Aug 2008.

[34] B. J. Kim, H. Ohsumi, T. Komesu, S. Sakai, T. Morita, H. Takagi, and T. Arima. Phase-Sensitive Observation of a Spin-Orbital Mott State in Sr_2IrO_4. *Science*, **323**:1329–1332, 2009.

[35] J. Kim, M. Daghofer, A. H. Said, T. Gog, J. van den Brink, G. Khaliullin, and B. J. Kim. Excitonic quasiparticles in a spin-orbit Mott insulator. *Nature Communications*, **5**:4453, 2014.

[36] Y. K. Kim, O. Krupin, J. D. Denlinger, A. Bostwick, E. Rotenberg, Q. Zhao, J. F. Mitchell, J. W. Allen, and B. J. Kim. Fermi arcs in a doped pseudospin-1/2 Heisenberg antiferromagnet. *Science*, **345**:187–190, 2014.

[37] Y. K. Kim, N. H. Sung, J. D. Denlinger, and B. J. Kim. Observation of a d-wave gap in electron-doped Sr_2IrO_4. *Nature Physics*, **12**:37, Oct 2015.

[38] S. A. J. Kimber, C. D. Ling, D. J. P. Morris, A. Chemseddine, P. F. Henry, and D. N. Argyriou. Interlayer tuning of electronic and magnetic properties in honeycomb ordered $Ag_3LiRu_2O_6$. *J. Mater. Chem.*, **20**:8021–8025, 2010.

[39] A. Kitaev. Anyons in an exactly solved model and beyond. *Annals of Physics*, **321**:2 – 111, 2006. January Special Issue.

[40] Y. Kulik and O. P. Sushkov. Width of the longitudinal magnon in the vicinity of the O(3) quantum critical point. *Phys. Rev. B*, **84**:134418, Oct 2011.

[41] S. Kunkemöller, D. Khomskii, P. Steffens, A. Piovano, A. A. Nugroho, and M. Braden. Highly Anisotropic Magnon Dispersion in Ca_2RuO_4: Evidence for Strong Spin Orbit Coupling. *Phys. Rev. Lett.*, **115**:247201, Dec 2015.

[42] A. Kłosiński, D. V. Efremov, J. van den Brink, and K. Wohlfeld. Photoemission Spectrum of Ca_2RuO_4: Spin Polaron Physics in an S=1 Antiferromagnet with Anisotropies, 2019.

[43] C. Lanczos. An iteration method for the solution of the eigenvalue problem of linear differential and integral operators. *J. Res. Natl. Bur. Stand. B*, **45**:255–282, 1950.

[44] A. Liebsch and H. Ishida. Subband filling and Mott transition in $Ca_{2-x}Sr_xRuO_4$. *Phys. Rev. Lett.*, **98**:216403, May 2007.

[45] J. M. Luttinger and J. C. Ward. Ground-State Energy of a Many-Fermion System. II. *Phys. Rev.*, **118**:1417–1427, Jun 1960.

[46] M. Matsumoto, B. Normand, T. M. Rice, and M. Sigrist. Field- and pressure-induced magnetic quantum phase transitions in $TlCuCl_3$. *Phys. Rev. B*, **69**:054423, Feb 2004.

[47] O. N. Meetei, W. S. Cole, M. Randeria, and N. Trivedi. Novel magnetic state in d^4 Mott insulators. *Phys. Rev. B*, **91**:054412, Feb 2015.

[48] Y. Miura, Y. Yasui, M. Sato, N. Igawa, and K. Kakurai. New-Type Phase Transition of Li_2RuO_3 with Honeycomb Structure. *Journal of the Physical Society of Japan*, **76**:033705, 2007.

[49] T. Mizokawa, L. H. Tjeng, G. A. Sawatzky, G. Ghiringhelli, O. Tjernberg, N. B. Brookes, H. Fukazawa, S. Nakatsuji, and Y. Maeno. Spin-Orbit Coupling in the Mott Insulator Ca_2RuO_4. *Phys. Rev. Lett.*, **87**:077202, Jul 2001.

[50] W. Nolting. *Viel-Teilchen-Theorie*. Springer, Berlin; Heidelberg [u.a.], 6th edition, 2005.

[51] A. M. Oleś. Antiferromagnetism and correlation of electrons in transition metals. *Phys. Rev. B*, **28**:327–339, Jul 1983.

[52] K. Pajskr, P. Novák, V. Pokorný, J. Kolorenč, R. Arita, and J. Kuneš. On the possibility of excitonic magnetism in Ir double perovskites. *Phys. Rev. B*, **93**:035129, Jan 2016.

[53] D. Pesin and L. Balents. Mott physics and band topology in materials with strong spin-orbit interaction. *Nature Physics*, **6**:376, Mar 2010.

[54] M. Potthoff, M. Aichhorn, and C. Dahnken. Variational Cluster Approach to Correlated Electron Systems in Low Dimensions. *Phys. Rev. Lett.*, **91**:206402, Nov 2003.

[55] M. Potthoff. *Dynamical Variational Principles for Strongly Correlated Electron Systems*, pages 135–147. Springer Berlin Heidelberg, Berlin, Heidelberg, 2006.

[56] Potthoff, M. Self-energy-functional approach: Analytical results and the Mott-Hubbard transition. *Eur. Phys. J. B*, **36**:335–348, 2003.

[57] Potthoff, M. Self-energy-functional approach to systems of correlated electrons. *Eur. Phys. J. B*, **32**:429–436, 2003.

[58] J. G. Rau, E. K.-H. Lee, and H.-Y. Kee. Spin-Orbit Physics Giving Rise to Novel Phases in Correlated Systems: Iridates and Related Materials. *Annual Review of Condensed Matter Physics*, **7**:195–221, 2016.

[59] C. Rüegg, B. Normand, M. Matsumoto, A. Furrer, D. F. McMorrow, K. W. Krämer, H. U. Güdel, S. N. Gvasaliya, H. Mutka, and M. Boehm. Quantum Magnets under Pressure: Controlling Elementary Excitations in $TlCuCl_3$. *Phys. Rev. Lett.*, **100**:205701, May 2008.

[60] S. Sachdev. Quantum magnetism and criticality. *Nature Physics*, **4**:173–185, 2008.

[61] S. Sachdev and B. Keimer. Quantum criticality. *Physics Today*, **64**:29, 2011.

[62] T. Sato, T. Shirakawa, and S. Yunoki. Spin-orbital entangled excitonic insulator with quadrupole order. *Phys. Rev. B*, **99**:075117, Feb 2019.

[63] M. Schmid. Personal communication. See also [5].

[64] D. Sénéchal, D. Perez, and M. Pioro-Ladrière. Spectral Weight of the Hubbard Model through Cluster Perturbation Theory. *Phys. Rev. Lett.*, **84**:522–525, Jan 2000.

[65] D. Sénéchal. An introduction to quantum cluster methods. arXiv:0806.2690, Jun 2008.

[66] D. Sénéchal, D. Perez, and D. Plouffe. Cluster perturbation theory for Hubbard models. *Phys. Rev. B*, **66**:075129, Aug 2002.

[67] S.-M. Souliou, J. Chaloupka, G. Khaliullin, G. Ryu, A. Jain, B. J. Kim, M. Le Tacon, and B. Keimer. Raman Scattering from Higgs Mode Oscillations in the Two-Dimensional Antiferromagnet Ca_2RuO_4. *Phys. Rev. Lett.*, **119**:067201, Aug 2017.

[68] S. Sugano, Y. Tanabe, and H. Kamimura. *Multiplets of Transition-Metal Ions in Crystals*. Acad. Pr., New York [u.a.], 1970.

[69] D. Sutter, C. G. Fatuzzo, S. Moser, M. Kim, R. Fittipaldi, A. Vecchione, V. Granata, Y. Sassa, F. Cossalter, G. Gatti, M. Grioni, H. M. Rønnow, N. C. Plumb, C. E. Matt, M. Shi, M. Hoesch, T. K. Kim, T.-R. Chang, H.-T. Jeng, C. Jozwiak, A. Bostwick, E. Rotenberg, A. Georges, T. Neupert, and J. Chang. Hallmarks of Hunds coupling in the Mott insulator Ca_2RuO_4. *Nature Communications*, **8**:15176, 2017.

[70] H. Takagi, T. Takayama, G. Jackeli, G. Khaliullin, and S. E. Nagler. Kitaev quantum spin liquid - concept and materialization. arXiv:1903.08081, Mar 2019.

[71] R. Triebl, G. J. Kraberger, J. Mravlje, and M. Aichhorn. Spin-orbit coupling and correlations in three-orbital systems. *Phys. Rev. B*, **98**:205128, Nov 2018.

[72] H. Watanabe, T. Shirakawa, and S. Yunoki. Microscopic Study of a Spin-Orbit-Induced Mott Insulator in Ir Oxides. *Phys. Rev. Lett.*, **105**:216410, Nov 2010.

[73] S. M. Winter, Y. Li, H. O. Jeschke, and R. Valentí. Challenges in design of Kitaev materials: Magnetic interactions from competing energy scales. *Phys. Rev. B*, **93**:214431, Jun 2016.

[74] S. M. Winter, A. A. Tsirlin, M. Daghofer, J. van den Brink, Y. Singh, P. Gegenwart, and R. Valentí. Models and materials for generalized Kitaev magnetism. *Journal of Physics: Condensed Matter*, **29**:493002, Nov 2017.

[75] W. Witczak-Krempa, G. Chen, Y. B. Kim, and L. Balents. Correlated Quantum Phenomena in the Strong Spin-Orbit Regime. *Annual Review of Condensed Matter Physics*, **5**:57–82, 2014.

[76] B. Yuan, J. P. Clancy, A. M. Cook, C. M. Thompson, J. Greedan, G. Cao, B. C. Jeon, T. W. Noh, M. H. Upton, D. Casa, T. Gog, A. Paramekanti, and Y.-J. Kim. Determination of Hund's coupling in 5*d* oxides using resonant inelastic x-ray scattering. *Phys. Rev. B*, **95**:235114, Jun 2017.

[77] I. Zegkinoglou, J. Strempfer, C. S. Nelson, J. P. Hill, J. Chakhalian, C. Bernhard, J. C. Lang, G. Srajer, H. Fukazawa, S. Nakatsuji, Y. Maeno, and B. Keimer. Orbital Ordering Transition in Ca_2RuO_4 Observed with Resonant X-Ray Diffraction. *Phys. Rev. Lett.*, **95**:136401, Sep 2005.

[78] G. Zhang and E. Pavarini. Mott transition, spin-orbit effects, and magnetism in Ca_2RuO_4. *Phys. Rev. B*, **95**:075145, Feb 2017.

Zusammenfassung in deutscher Sprache

Das Verständnis der Interaktion von Spin-Bahn-Kopplung (SBK) und elektronischen Korrelationen birgt großes Potential hinsichtlich der Erforschung topologisch nichttrivialer Mott-Isolatoren [53] und Spinflüssigkeiten [8]. Die bekannten $3d$-Metalle, wie Eisen, Nickel und Kupfer, besitzen jedoch eher schwache SBK. Geeignetere Kandidaten finden sich unter den $5d$ und $4d$ Übergangsmetalloxiden, da sie eine stärkere SBK aufweisen. Besonders die Elektronenkonfigurationen der $4d^4$, $4d^5$, $5d^4$ und $5d^5$ Übergangsmetalloxide mit Ru^{4+}, Ir^{5+} und Ir^{4+} weisen unerwartete Grundzustände und interessante magnetische Phänomene auf [58, 75].

Die Wirkung der SBK ist in Systemen mit t_{2g}^5-Konfiguration besonders klar, wo es ein Loch in den t_{2g}-Niveaus gibt, dessen Bahndrehimpuls $L = 1$ und Spin $S = 1$ von der SBK zu einem Gesamtdrehimpuls J gekoppelt werden. Die Energiestruktur besteht aus einem Dublett $J = 1/2$ und einem Quartett $J = 3/2$ [30], welche mit insgesamt fünf Elektronen jeweils halb beziehungsweise ganz gefüllt sind. Das Zusammenspiel von SBK und lokalen Coulomb-Wechselwirkungen führt dann zu einem Mott-Isolator mit einem Loch im $J = 1/2$-Zustand, welches magnetisch ordnen kann. Sr_2IrO_4, ein einschichtiges Material mit quadratischer Gitterstruktur, ist ein Paradebeispiel eines solchen SBK getriebenen Mott-Isolators [6]. Die effektive Ein-Band-Beschreibung des Lochs im $J = 1/2$-Zustands ist robust genug, Dotierung zu überstehen, wobei Fermibögen [36] und Hinweise auf Supraleitung [37] beobachtet worden sind. Für Systeme mit Honigwabenstruktur, wie α-$RuCl_3$ und vergleichbare Iridate [70, 74], ist die von der SBK erzeugte magnetische Anisotropie ähnlich zum Kitaev-Modell für Spinflüssigkeiten [39].

In einem System mit vier Elektronen ist die physikalische Situation jedoch eine andere. Für sehr starke SBK könnte J-J-Kopplung vorliegen, bei welcher beide Löcher im $J = 1/2$-Zustand sitzen und einen Singulettgrundzustand $J = 0$ bilden [22]. Die Realisierung eines solchen Grundzustands wird in nicht-magnetischen Doppelperovskit-Iridaten [18, 52] vermutet, da die SBK dort groß genug sein könnte um die J-J-Kopplung zu stabilisieren.

Bei gemäßigten SBK-Stärken ist durch starke lokale Elektronenwechselwirkungen in Form von Coulombwechselwirkung und Hundscher Kopplung jeweils nur ein Orbital pro Platz voll besetzt. Die zwei Löcher in den anderen beiden halbgefüllten Orbitalen bilden daraufhin den Gesamtbahndrehimpuls $L = 1$ und den Gesamtspin $S = 1$, welcher von der SBK zu einem Gesamtdrehimpuls $J = 0, 1, 2$ gekoppelt wird. Theoretische Betrachtungen [31, 47] lassen einen nichtmagnetischen Grundzustand $J = 0$ vermuten,

der maßgeblich von der SBK unterstützt wird. Jedoch ist die Anregungslücke zum magnetischen Triplett $J = 1$ nicht allzu groß, da sie mit der SBK skaliert, wie in der Levelstruktur auf der linken Seite von Abb. 6.2 skizziert. In diesem Fall kann durch Superaustausch, welcher die höher liegenden magnetischen Triplettzustände $J = 1$ und die Quintettzustände $J = 2$ miteinbezieht, exzitonischer Magnetismus auftreten [31, 47]. Ist der Superaustausch stark genug, um mit der von der SBK erzeugten Singulett-Triplett-Aufspaltung zu konkurrieren, werden der lokalen Wellenfunktion Anteile des $J = 1$-Zustandes zum $J = 0$-Zustand beigemischt. Hierbei erlangt die Wellenfunktion ein magnetisches Moment, welches ordnen kann. Ein solcher exzitonischer Magnetismus wurde bereits in Berechnungen eindimensionaler Drei-Band-Modelle mittels Dichtematrixrenormierungsgruppe [29], sowie in Dynamischen Molekularfeldtheorie-Rechnungen für unendliche Dimensionen gefunden [62].

Eine mögliche Realisierung dieses Prozesses wird in Ca_2RuO_4 erwartet. Dieses t_{2g}^4-Ruthenat mit quadratischer Gitterstruktur zeigt für tiefe Temperaturen eine antiferromagnetische, isolierende Phase auf [7, 41]. Messungen der Spinwellendispersion zeigten ein Maximum derselben im Zentrum der ersten Brillouinzone [28], was in starkem Kontrast zur Beschreibung von Ca_2RuO_4 im Sinne eines Heisenberg-Antiferromagneten steht und daher als Zeichen exzitonischen Magnetismus gedeutet wurde [22, 67, 77].

Eine alternative Erklärung des Magnetismus in Ca_2RuO_4 stützt sich auf das Vorhandensein eines Spin-1-Magnetismus durch starke orbitale Polarisierung, da die Tieftemperaturphase von Ca_2RuO_4 mit einer Stauchung der RuO_6-Oktaeder entlang der c-Achse einhergeht [2, 17, 49, 77]. Das resultierende tetragonale Kristallfeld senkt das xy-Orbital ab, auf dessen nahezu volle Besetzung Experimente [15] und numerische Berechnungen [13, 14, 21, 44] hindeuten. *Ab initio*-Rechnungen [78], die ihrerseits von winkelaufgelösten Photoemissionsspektroskopie-Experimenten gestützt werden [69], postulieren eine Halbfüllung der yz- und xz-Orbitale, die wiederum einen Spin $S = 1$ bilden. Die SBK wird hierbei nur als Störung angesehen und nicht als verantwortlich für den Magnetismus [41].

Modell und Methode

Mithilfe eines Dreiband-Hubbard-Modells, welches die kinetische Energie der Elektronen, lokale Wechselwirkungen, die SBK und das tetragonale Kristallfeld berücksichtigt, betrachten wir die Interaktion von vier Elektronen auf einem zweidimensionalen Quadratgitter. Die Dispersionsrelation der kinetischen Energie wird maßgeblich von der räumlichen Orientierung der t_{2g}-Orbitale bestimmt. Den stärksten Anteil hat das Hüpfen zu benachbarten Plätzen zwischen gleichen Orbitalen [27]. Dabei kann nur eines der drei Orbitale, das xy-Orbital, in beiden Kristallrichtungen am Austausch der Elektronen teilhaben. Elektronen in den beiden anderen Orbitalen xz und yz können nur in die x- beziehungsweise y-Richtung hüpfen. Des Weiteren zeigen auf Dichtefunktionaltheorie basierende Rechnungen zu Ca_2RuO_4 [63], dass es zudem einen nicht vernachlässigbaren Austausch zwischen den xy-Orbitalen übernächster Nachbarn und ein Hüpfen

zwischen dem xz- und dem xy-Orbital benachbarter Plätze in x-Richtung gibt. Lokale Elektronenwechselwirkungen sind durch die Coulombwechselwirkung U und die Hundsche Kopplung J_H gegeben, welche die Interaktion von Elektronen eines Ions innerhalb und zwischen den Orbitalen am selben Gitterplatz beschreiben. In zweiter Ordnung Störungstheorie ergeben sich durch die Hundsche Kopplung und den Superaustausch die Goodenough-Kanamori-Anderson-Regeln (GKA), welche die Ausrichtung benachbarter Spins beschreiben.

Aus dem Wechselspiel von Coulombwechselwirkung, Hundscher Kopplung, SBK und tetragonalem Kristallfeld ergeben sich auf atomarer Ebene verschiedene Energiezustände je nach relativer Stärke der Terme. Im Fall von starker Hundscher Kopplung und schwacher SBK, $\lambda < J_\mathrm{H}$, bilden sich die bereits zuvor genannten J_{LS}-Zustände mit $J_{LS} = 0, 1, 2$ aus. Der Grundzustand $J_{LS} = 0$ ist hierbei nichtmagnetisch und die Energiedifferenz zum nächsthöheren, magnetischen Triplett $J_{LS} = 1$ beträgt gerade $\lambda/2$, siehe Abb. 6.2. Der Quintettzustand $J_{LS} = 2$ ist wiederum um λ höher in der Energie.

Bei starker SBK, $\lambda > J_\mathrm{H}$, kann der Grundzustand als doppelt besetzter $J = 1/2$-Zustand angesehen werden, was ebenfalls zu einem Singulettgrundzustand $J_{jj} = 0$ führt. Der Abstand zum magnetischen Triplett $J_{jj} = 1$ skaliert mit λ und ist deshalb so groß, dass eine Anregung in diesen Zustand durch Superaustausch nicht mehr plausibel ist. Folglich treten in diesem Regime keine magnetischen Ordnungen auf.

Zieht man im Fall $\lambda < J_\mathrm{H}$ das tetragonale Kristallfeld mit in Betracht, so spaltet das Triplett $J_{LS} = 1$ auf in ein Dublett $D_{1/2}$ und ein Singulett S_3. Im Falle eines gestauchten RuO_6-Oktaeders ist das tetragonale Kristallfeld stets positiv, $\Delta > 0$, und das Dublett $D_{1/2}$ liegt tiefer als das Singulett S_3. Für zunehmendes Kristallfeld nähert sich das Dublett $D_{1/2}$ an das Singulett S_0 an und bildet mit ihm im Limes verschwindender SBK den dreifach entarteten Grundzustand. Das Singulett S_3 spaltet sich ab und bildet bei $\lambda = 0$ mit den $J_{LS} = 2$-Zuständen den sechsfach entarteten angeregten Zustand.

Da die Berechnungen mit Dichtematrixrenormierungsgruppe vor allem für eindimensionale Systeme geeignet sind und materialspezifische Dynamische Molekularfeldtheorie-Rechnungen die für die antiferromagnetische Ordnung nötige tiefe Temperatur nicht erreichen [5], wird in dieser Arbeit die variationelle Cluster-Näherung [54] genutzt. Mit dieser Methode können langreichweitige Wechselwirkungen sowie Symmetriebrechung simuliert werden. Des Weiteren ist es möglich, zweidimensionale Gitter sowie den Grundzustand bei Temperatur $T = 0$ zu betrachten, was sich von den bisher durchgeführten Rechnungen unterscheidet. Die erfolgreiche Anwendbarkeit der variationellen Cluster-Näherung hat sich bereits beim Vergleich mit winkelaufgelöster Photoemissionsspektroskopie in Sr_2IrO_4 gezeigt [72].

Für die variationelle Cluster-Näherung wird die Lösung des Hamilton-Operators auf einem kleinen Cluster benötigt, welche durch exakte Diagonalisierung gefunden wird. Die Selbstenergie des Clusters wird dann in die Einteilchen-Green-Funktion im thermodynamischen Limes eingesetzt um das großkanonische Potential zu erhalten. Basierend auf der Selbstenergiefunktionaltheorie [56] kann das großkanonische Potential nun optimiert werden, indem Einteilchenparameter auf dem Referenzsystem variiert werden.

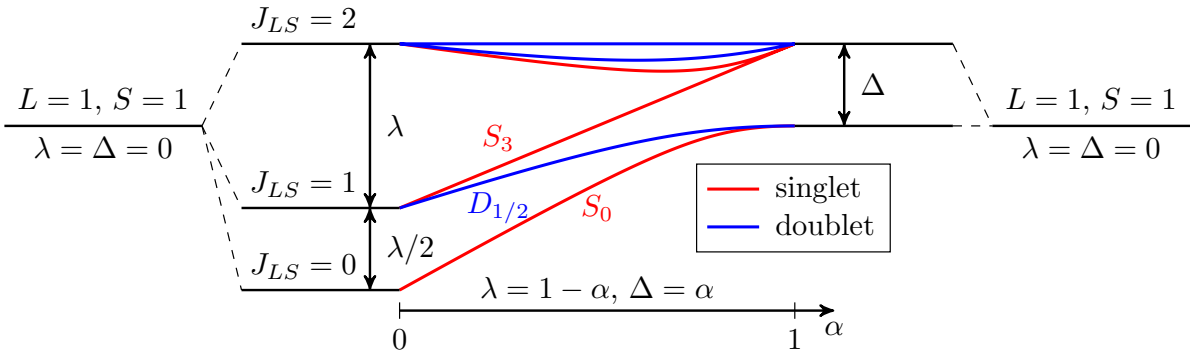

Abbildung 6.2: Die Wechselwirkung von SBK λ und tetragonalem Kristallfeld Δ im Fall $\lambda, \Delta < J_{\mathrm{H}}$ führt zu einer Aufspaltung der Energieniveaus. Im Falle $\Delta = 0$ ergibt sich ein nichtmagnetischer Grundzustand $J_{LS} = 0$, sowie ein magnetisches Triplett $J_{LS} = 1$ und ein Dublett $J_{LS} = 2$, deren Energieaufspaltungen jeweils von λ abhängen. Für zunehmendes Kristallfeld spalten die Energiezustände auf. Aus dem Triplett $J_{LS} = 1$ bilden sich ein Dublett $D_{1/2}$ und ein höher liegendes Singulett S_3 für gestauchte RuO_6-Oktaeder mit $\Delta > 0$. Im Limes verschwindender SBK ist der Grundzustand dreifach entartet.

Zum Beispiel können die kinetische Energie und das chemische Potential solche Variationsparameter sein. Insbesondere lassen sich fiktive symmetriebrechende Weiss-Felder anwenden, welche nur auf den kleinen Cluster, nicht jedoch auf das ganze Gitter wirken. Optimiert ein solches symmetriebrechendes Feld die Selbstenergie eines vollsymmetrischen Hamilton-Operators, kann auf spontane Symmetriebrechung geschlossen werden.

Exzitonischer Magnetismus

In einem vereinfachten Modell ohne tetragonales Kristallfeld, welches nur das Nächste-Nachbar-Hüpfen, lokale Wechselwirkungen und die SBK berücksichtigt, wird der Einfluss der SBK auf den Magnetismus untersucht. Durch Anwenden verschiedener Weiss-Felder mit antiferromagnetischer Spinordnung in Schachbrett- und Streifenmuster sowie diversen Orbitalordnungen kann das großkanonische Potential optimiert werden. Die auftretenden Bereiche und Phasen sind in Abb. 6.3 auf der λ/t-Achse graphisch dargestellt und werden im Folgenden diskutiert.

Für kleine Werte der SBK, $\lambda < 0.4t$, zeigt sich ein antiferromagnetisches Streifenmuster für die Spins in S_x-Richtung (orangefarbener Bereich). Die xy- und yz-Orbitale sind in einem um 90° gedrehten Streifenmuster abwechselnd mit einem Loch besetzt, während das xz-Orbital stets mit einem Loch besetzt ist. Ein solches Spin-Orbital-Muster entspricht den GKA-Regeln und wird vom Superaustausch zwischen benachbarten Plätzen bestimmt.

Für gemäßigte Werte der SBK, $0.4t \lesssim \lambda \lesssim 0.6t$, tritt ein antiferromagnetisches Schachbrettmuster mit Spin in S_z-Richtung auf (dunkelblauer Bereich). Der Einfluss der Orbitale auf den Magnetismus ist hierbei sehr gering, was sich in den Werten für das großkanonische Potential zeigt. Die Werte verschiedener Orbitalordnungen liegen sehr nah beieinander, woraus geschlossen werden kann, dass die Spinordnung das maßgebliche Element der Symmetriebrechung ist. Betrachtet man die Erwartungswerte der J_{LS}-Zustände, so erkennt man, dass der Magnetismus durch Beimischung des $J_{LS} = 1$-Zustandes zum $J_{LS} = 0$-Zustand entsteht, was für exzitonischen Magnetismus charakteristisch ist. Die Lochdichten der Orbitale zeigen eine leichte Mehrbesetzung des xy-Orbitals auf, was seinen Ursprung in der Orbitalabhängigkeit des Hüpfens hat.

Für stärkere SBK, $\lambda > 1.1t$, wird der Magnetismus unterdrückt und das System befindet sich im paramagnetischen Zustand (grauer Bereich). Der Grundzustand wird beinahe vollständig durch den $J_{LS} = 0$-Zustand charakterisiert und die Orbitale sind gleich stark besetzt.

Eine detailliertere Parameterstudie bezüglich der lokalen Wechselwirkung, dem Hüpfen und der SBK auf einem Cluster mit zwei Plätzen bestätigt diese Beobachtungen. Zu starke SBK, sowie zu starke lokale Wechselwirkungen unterdrücken den Magnetismus.

Des Weiteren wird der Einfluss des anisotropen Hüpfens auf die magnetische Phase untersucht, indem die zuvor verbotenen Hüpfrichtungen für das xz- und yz-Orbital mit kleiner Stärke erlaubt werden. Es zeigt sich, dass die exzitonischen Bereiche auch noch für größere SBK existieren als im komplett anisotropen Fall. Dies ist jedoch eher der

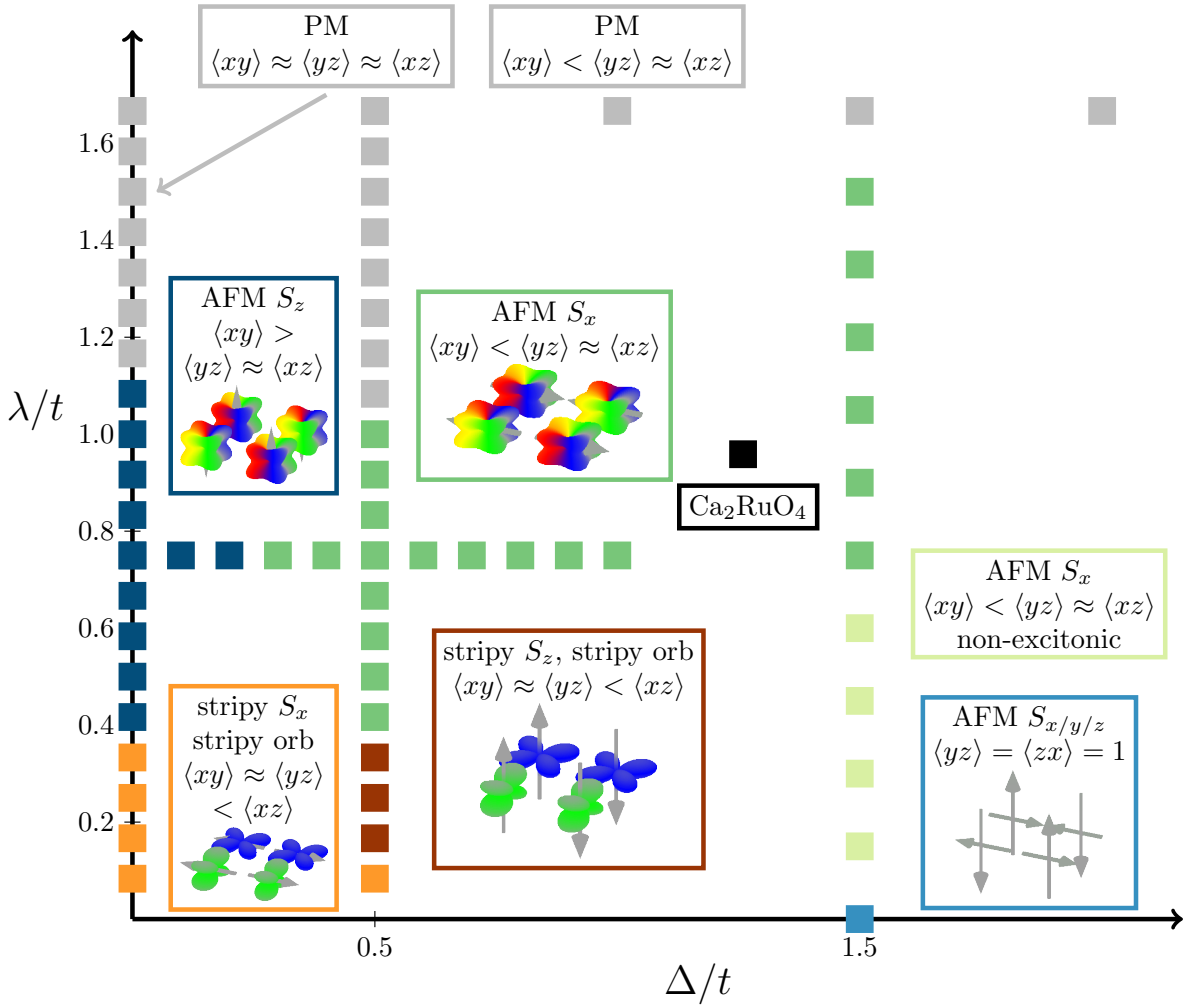

Abbildung 6.3: Phasendiagramm abhängig von SBK λ und tetragonalem Kristallfeld Δ, abgeleitet aus den Ergebnissen dieser Arbeit. Für jede Phase, gekennzeichnet durch eine Farbe, sind die Spin- und Orbitalordnung durch ein Piktogramm, sowie die Lochdichten $\langle\alpha\rangle$, $\alpha = xy$, yz zx angegeben. Die kinetische Energie t dient als Energieeinheit. Die Abkürzungen AFM beziehungsweise PM stehen für die antiferromagnetische beziehungsweise paramagnetische Phase. Beschreibung siehe Text.

erhöhten kinetischen Energie als einem Symmetrieeffekt zuzusprechen. Auch führt die erhöhte Isotropie nicht etwa zu einem Angleichen der Orbitalfüllungen, sondern verstärkt die Lochdichte im xy-Orbital leicht.

Wechselspiel von SBK und tetragonalem Kristallfeld

Die Ergebnisse für die Interaktion von SBK und tetragonalem Kristallfeld sind in Abb. 6.3 in einem Phasendiagramm dargestellt. Unter Berücksichtigung eines schwachen Kristallfeldes, $\Delta = 0.5t$, ergibt sich für schwache SBK, $\lambda \lesssim 0.1t$, zunächst die bekannte Streifenordnung mit S_x und den abwechselnd besetzten Orbitalen. Stärkere SBK, $0.1t < \lambda < 0.4t$, führt zu einer Reorientierung der Spins in S_z-Richtung, wobei die Orbitalordnung erhalten bleibt (roter Bereich).

Für mittlere Werte der SBK, $0.4t < \lambda \lesssim 1.1t$, tritt erneut der antiferromagnetische, exzitonische Bereich auf (dunkelgrüner Bereich). Jedoch bewirkt die Anwesenheit des Kristallfeldes eine Reorientierung der Spins in S_x-Richtung. Durch das vom Kristallfeld bewirkte Absenken des xy-Orbitals ändert sich auch die Orbitalbesetzung. Die Lochdichte des xy-Orbitals unterliegt deutlich der der anderen beiden Orbitale, die ihrerseits nahezu gleich besetzt sind. Die Erwartungswerte der J_{LS}-Zustände zeigen weiterhin die Beteiligung des $J_{LS} = 1$-Zustandes am Magnetismus. Der $J_{LS} = 2$-Zustand ist zu einem geringen Teil besetzt, aber konstant mit und ohne Weiss-Feld, sodass er nur zur orbitalen Polarisation beiträgt. Bei der Beschreibung des Grundzustandes durch die Zustände S_0, $D_{1/2}$ und S_3 zeigt sich, dass das Singulett S_0 und das Dublett $D_{1/2}$ am Magnetismus beteiligt sind. Das höher liegende Singulett S_3 ist verschwindend gering besetzt.

Für stärkere SBK, $\lambda > 1.1t$, tritt auch hier die paramagnetische Phase ein. Die orbitale Polarisierung mit geringer Lochbesetzung im xy-Orbital wird reduziert, bleibt aber erhalten.

Für deutlich stärkere Kristallfelder, $\Delta = 1.5t$, verschwindet die Steifenphase für schwache SBK gänzlich. Im Fall verschwindender SBK, $\lambda = 0$, befindet sich das System in vollständiger orbitaler Polarisation mit je halbgefülltem xz- und yz-Orbital. Die Spinordnung ist antiferromagnetischer Natur, wobei die Orientierung des Spins nicht festgelegt ist (hellblauer Bereich).

Für gemäßigte SBK, $0 < \lambda < 1.6t$, tritt erneut der antiferromagnetische Bereich mit S_x-Ordnung auf. Jedoch zeigt sich hier für $\lambda < 0.8t$ kein exzitonischer Magnetismus. Das xy-Orbital ist beinahe leer, was die Erklärung durch Spin-1-Magnetismus stützt. Im Bereich geringer SBK ist es somit möglich, schachbrettartigen Antiferromagnetismus durch orbitale Polarisation hervor zu rufen.

Für zunehmendes SBK, $0.8t \lesssim \lambda < 1.6t$, kehrt jedoch der exzitonische Magnetismus zurück und geht mit einer starken, vom tetragonalen Kristallfeld stabilisierten, Orbitalpolarisation einher. Der Einfluss der SBK kann nicht vernachlässigt werden, da sich auch hier für starke SBK, $\lambda > 1.6t$, die paramagnetische Phase zeigt. Selbst für sehr starke tetragonale Kristallfelder bis $\Delta = 4t$ kann bei sehr starker SBK, $\lambda = 1.67t$, keine magnetische Ordnung erzwungen werden. Erst für geringere SBK, $\lambda = 1.25t$, ist es mög-

lich durch zunehmendes Kristallfeld einen Übergang von der paramagnetischen Phase in die geordnete Phase herbei zu führen. Hierbei zeigt sich ein quantenkritischer Punkt bei $\Delta \approx t$.

Ca_2RuO_4

Anhand von Dichtefunktionaltheorie-Rechnungen [63] können materialspezifische Hüpfterme für Ca_2RuO_4 abgeleitet werden. Es zeigt sich, dass das Nächste-Nachbar-Hüpfen des xy-Orbitals dominiert. Das Nächste-Nachbar-Hüpfen der xz- und yz-Orbitale in bestimmte Richtungen ist dagegen nur ungefähr zwei Drittel so groß. Zusätzlich relevant sind das Hüpfen zwischen xy-Orbitalen übernächster Nachbarn und das Hüpfen zwischen dem xz- und dem xy-Orbital benachbarter Plätze, welche beide ungefähr die halbe Stärke des xy-Nächste-Nachbar-Hüpfens aufzeigen.

Unsere Modellrechnungen für Ca_2RuO_4 kombinieren diese Hüpfparameter mit kürzlich aus Experimenten abgeleiteten Werten für die SBK, die lokale Elektronenwechselwirkungen und das Kristallfeld [22]. Es zeigt sich, dass Ca_2RuO_4 in den Bereich exzitonischen Magnetismus fällt, obwohl die Polarisierung der Orbitale sehr stark ist (schwarzer Datenpunkt). Die Spins ordnen antiferromagnetisch mit $S_x + S_y$, was experimentellen Beobachtungen in Ca_2RuO_4 entspricht [7]. Zudem erweist sich das System als recht anfällig für Änderungen der SBK, da nur für Stärken in der Größenordnung der kinetischen Energie der exzitonische Charakter vorliegt. Für kleinere SBK ergibt sich ein reiner Spin-1-Magnetismus, während stärkere SBK einen paramagnetischen Zustand bewirkt.

Zusammenfassung und Ausblick

Zusammengefasst zeigen unsere Ergebnisse ein vielfältiges Phasendiagramm mit Spin- und Orbitalordnungen sowie exzitonischen und nicht-exzitonischen Bereichen, die maßgeblich von der Wechselwirkung zwischen SBK und tetragonalem Kristallfeld beeinflusst werden. Berechnungen für das reine Spin-1-Szenario, $\lambda = 0$, zeigen, dass das tetragonale Kristallfeld ausreicht, um schachbrettartige magnetische Ordnungen vorzufinden. Jedoch ist der Magnetismus selbst für größere Kristallfelder stark von der SBK beeinflusst. Auch im stark orbitalpolarisierten Bereich gibt es Bereiche mit exzitonischem Charakter. Zusätzlich zeigt das Verschwinden der magnetischen Ordnung für große SBK, dass der Einfluss der SBK nicht unterschätzt werden darf.

Für gemäßigte Stärken der SBK und des tetragonalen Kristallfeldes können der Spin-1-Magnetismus und der exzitonische Magnetismus gleichzeitig existieren. Die magnetische Ordnung beeinflusst nur die Zuständen $J_{LS} = 0, 1$ beziehungsweise das Singulett S_0 und das Dublett $D_{1/2}$. Der $J_{LS} = 2$-Zustand ist zwar leicht besetzt und trägt damit zur orbitalen Polarisation bei, leistet aber keinen Beitrag zum Magnetismus. Dies erklärt, warum magnetische Anregungen einschließlich der Higgs-Mode durch den exzitonischen Singulett-Triplett-Magnetismus erklärt werden können.

Eine Fortführung und Anwendung der Ergebnisse dieser Arbeit ist in vielerlei Hinsicht möglich. Nachdem sich gezeigt hat, dass exzitonischer Magnetismus für gemäßigte Stärken der SBK und des Kristallfeldes existiert, kann die Suche nach diesem in anderen Materialien fortgeführt werden. Hierzu eignen sich insbesondere Ruthenate mit Honigwabenstruktur, zum Beispiel Li_2RuO_3 [48] und $Ag_3LiRu_2O_6$ [38]. Des Weiteren kann die variationelle Cluster-Näherung auch auf Systeme endlicher Temperatur erweitert werden, was ermöglicht, temperaturabhängige Phasenübergänge und ihren Einfluss auf den exzitonischen Magnetismus zu untersuchen.

TERESA FELDMAIER

Schulausbildung

1999 – 2003 **Grundschule**.
Haldenschule Kernen

2003 – 2011 **Allgemeinbildendes Gymnasium**.
Friedrich-Schiller-Gymnasium Fellbach

Studium

2011–2014 **Bachelorstudiengang Physik**.
Universität Stuttgart

2014 – 2016 **Masterstudiengang Physik**.
Universität Stuttgart

2015 – 2016 **Masterarbeit**, *Variational-cluster approximation for strongly correlated materials*, Betreuung: Prof. Dr. Maria Daghofer.
Institut für funktionelle Materie und Quantentechnologien, Universität Stuttgart

2016–2019 **Promotion**, Betreuung: Prof. Dr. Maria Daghofer.
Institut für funktionelle Materie und Quantentechnologien, Universität Stuttgart

Wissenschaftliche Tätigkeiten

2013–2015 **Mitarbeiterin: Probiert die Uni aus**.
Gleichstellungsreferat, Universität Stuttgart

2013–2016 **Organisation: Vortragsreihe Physik die Wissen schafft**.
Fachbereich Physik, Universität Stuttgart

2013–2016 **Studentische Hilfskraft in der Lehre**.
Fachbereich Physik, Universität Stuttgart

2016–2019 **Organisation: Probiert die Uni aus und TryScience Workshop Physik**.
Gleichstellungsreferat, Universität Stuttgart

2016–2019 **Organisation: Mentoring Physik**.
Fachbereich Physik, Universität Stuttgart

2016–2019 **Wissenschaftliche Mitarbeiterin mit Lehrtätigkeit**.
Institut für funktionelle Materie und Quantentechnologien, Universität Stuttgart

Wissenschaftliche Poster

März 2016 **Variational-cluster approximation for iridiates**, Frühjahrstagung der Deutschen Physikalischen Gesellschaft, Regensburg.

Sept. 2016 **Variational-cluster approximation for iridiates**, Bad Honnef Physics School Frontiers of Quantum Matter, Physikzentrum Bad Honnef.

März 2017 **Variational Cluster Approximation for Spin Liquids**, Frühjahrstagung der Deutschen Physikalischen Gesellschaft, Dresden.

Sept. 2017 **Variational Cluster Approximation for Iridates**, Korrelationstage Dresden, Internationaler Workshop, Max Planck Institute for the Physics of Complex Systems, Dresden.

März 2018 **Variational-cluster approximation for d4 systems**, Frühjahrstagung der Deutschen Physikalischen Gesellschaft, Berlin.

Juni 2018 **Excitonic magnetism in d4 systems**, WE-Heraeus-Seminar on Trends in Quantum Magnetism, Wilhelm und Else Heraeus-Stiftung, Bad Honnef.

Danksagung

Diese Arbeit wäre ohne die Unterstützung vieler Menschen nicht möglich gewesen. Ganz besonders danken möchte ich

- Frau Prof. Dr. Maria Daghofer. Herzlichen Dank für die Ermöglichung und Betreuung der Promotion, für Ihre Unterstützung und Ihre Erklärungen. In meiner Situation hätte ich mir keine bessere und verständnisvollere Betreuung wünschen können.
- Herrn Jun.-Prof. Dr. Stefan Kaiser für die Übernahme des Mitberichts.
- Herrn Prof. Dr. Ronny Nawrodt für die Übernahme des Prüfungsvorsitzes. Vielen Dank auch für deine Unterstützung bei TryScience! Ohne dich und das Schülerlabor wären die Workshops nicht so erfolgreich gewesen!
- beim Land Baden-Württemberg für die Unterstützung in Form des bwHPC.
- meinen Kollegen am FMQ, insbesondere Pascal, Michael, Jan und Friedemann fürs Korrekturlesen der Arbeit. Danke, dass ihr immer Zeit hattet, meine Fragen und seltsamen Ergebnisse zu diskutieren.
- meinen lieben Freunden. Danke Philipp, Meli, Flo und Sascha für die schöne Promotionszeit und eure offenen Ohren für Probleme bei Datenauswertung, Literaturrecherche und sonstigem Unikram. Ich verspreche euch, weiterhin zu den Mittagessen zu kommen! Vielen Dank Gela, Marina und Maren für unsere schöne Studienzeit und eure Freundschaft darüber hinaus. Ganz lieben Dank an die zwei Tobis, sowie Feli und Philipp mit Isabelle und Nikolas. Ihr habt mich immer wieder geerdet, wenn ich zu weit in meine Forschung abgedriftet bin.
- meiner Familie für ihre grenzenlose Unterstützung und Liebe in jeder Situation. Danke, dass ich immer auf euch zählen kann!
- Matthias. Was wäre ich ohne dich?

Ehrenwörtliche Erklärung

Ich erkläre, dass ich diese Dissertation, abgesehen von den ausdrücklich bezeichneten Hilfsmitteln, selbständig verfasst habe.

Stuttgart, den 06. November 2019 *Teresa Feldmaier*